Óbuda University

Ph.D. Thesis

Study of complex nanostructures by infrared spectroscopy

Zsolt Szekrényes

Doctoral School on Materials Sciences and Technologies

Supervisor: Prof. Katalin Kamarás

Wigner Research Centre for Physics
Hungarian Academy of Sciences

Budapest, 2015

Acknowledgement

Contents

List of symbols

Symbol	Physical Quantity
$\mathbf{E}$	electric field
$\mathbf{B}$	magnetic induction
$\mathbf{P}$	polarization
$\mathbf{F}$	Force
c	velocity of light in vacuum
ϵ_0, μ_0	vacuum constants
$\mathbf{q}$	wave vector
$\hat{\mathbf{q}}$	complex wave vector
$\tilde{\mathbf{q}}$	unit vector
ω	frequency of light
σ	conductivity
ϵ	dielectric constant
n	refractive index
κ	extinction coefficient
η	complex refractive index
α	absorption coefficient
p	dipole moment
e^*	effective ionic charge
$\mathbf{v}$	velocity of the moving charges
k	force constant
$\mathbf{r}$	displacement
Γ	damping constant
μ	reduced mass
ν	phase velocity of the wave
d	sample thickness
MI	matrix isolation
ATR	attenuated total reflection

1. General introduction

This PhD work is focused around infrared spectroscopy of organic (self-assemled supramolecular networks) and inorganic (functionalized silicon carbide quantum dots) complex nano- and microstructures. The novelty of the present work is due to the joint application of standard infrared spectroscopic methods (i.e. absorption spectroscopy) with more special methods (i.e matrix isolation infrared spectroscopy and attenuated total internal reflection infrared spectroscopy) [1–7]. Both self-assembled systems and silicon carbide (SiC) surface functional groups are structures assembled on surfaces. In the first case the three-dimensional analogue molecular crystals were studied using the results obtained by surface characterization techniques (scanning tunneling microscopy). In the second case the surface itself was investigated by special infrared techniques.

To study the structure and dynamics of the supramolecular networks, temperature dependent absorption spectroscopy and matrix isolation were applied. The studied systems were formed from different uracil and piridyne based molecular constituents, which form self-assembled networks through hydrogen bonds. The recognition between the different molecular modules is mediated via multiple hydrogen bonding donor and acceptor sites. Hydrogen bonds can be sensitively detected by infrared spectroscopy by measuring their effect in the affected N-H and C=O vibrational regions of the spectra. To reveal the exact dimeric or multimeric character of the hydrogen bonded structures, different infrared spectroscopic methods are needed. The temperature dependent measurements give a full picture about the melting of hydrogen bonds while matrix isolation infrared spectroscopy offers the possibility to study the molecular modules in their monomeric state when no interaction between them is possible. The obtained experimental results were probed by comparison with temperature dependent ab initio molecular dynamics calculations (in collaboration with the University of Liverpool and Eötvös Loránd University, Budapest). The results of

these calculations yield excellent agreement with the hydrogen bond melting temperature observed by experiment [1–3].

The study of inorganic based hybrid nanostructures requires special, surface sensitive methods of infrared spectroscopy. These methods permit the identification of atomic monolayers and surface functional molecular groups. One of the methods used and implemented during my PhD work in our laboratory is attenuated total internal reflection (ATR) infrared spectroscopy. ATR proved its sensitivity in detecting the surface related Si-H vibrations on hydrogenated silicon crystal where conventional methods of infrared spectroscopy yield no results. The main activity in surface sensitive infrared spectroscopy during my PhD work was the study of the surface structure of SiC quantum dots. SiC quantum dots show very interesting and promising luminescent properties which are related to quantum confinement effects. At the same time they show a complex surface structure, which together with the revealed bioinert and biocompatibility properties, make them very promising materials for different biological applications. ATR revealed the presence of carboxyl and carboxilate groups on the surface of quantum dots, opening the possibility for further biological functionalization [4–6].

Chapter 2.1 describes some basic properties related to the light-matter interaction. Laws of reflection and refraction are introduced as a starting point for the description of surface sensitive infrared spectroscopy. The chapter continues with the treatment of optical properties of solids. As the experimental results obtained during my work are mainly related to the infrared spectroscopy of molecular groups, section 2.1.4 presents a short introduction to molecular vibrations. In the second part of the chapter (section 2.2) the concept of hydrogen bonding is treated starting with some general definitions and ending up with a brief theoretical background.

Chapter 3 is divided in two main parts: in the first part I introduce the studied molecular library followed by the description of the experimental techniques. At the end of this section I present what kind of information is available about hydrogen bonds through infrared spectroscopy. In the second section I describe basic principles of surface sensitive infrared spectroscopy followed by a short presentation of the photoluminescence spectroscopy, both methods being very powerful in the characterization of SiC quantum dots.

Chapter 4 starts with a short literature survey about different hydrogen bonded networks. Next I present my results measured on the constituents of the molecular library (sections 4.3 and 4.4). Homomolecular association (intermolecular hydrogen bonds between the same type of molecules) and heteromolecular ordering (intermolecular hydrogen bonds between different type of molecules) were studied during my PhD work. The joint application of different techniques demonstrates that the information which can be obtained from the vibrational spectra is vast and very useful in the chemical engineering of different supramolecular systems .

In chapter 5 first I introduce, based on literature data, optical and vibrational properties of bulk and nanostructured SiC. Then I present my results on basic photoluminescent behavior and surface structure of SiC quantum dots (section 5.3). Chemical transformation of carboxylic groups on the surface of SiC quantum dots to acid anhydride groups is possible at elevated temperatures, opening new possibilities for surface modifications (section 5.4).

In chapter 6 I present a short summary and formulate a very concise outlook of the thesis, while chapter 7 presents the thesis points and my publication list.

2. Fundamentals

The investigation of solid state systems using electromagnetic radiation provides a multitude of information about the electronic and lattice excitations and their dynamics. Electromagnetic radiation affects the particles that make up the medium, and the medium affects the electromagnetic radiation. This chapter starts with a short overview about how the electromagnetic field affects the solid state systems, and material parameters which characterize the medium are also introduced (2.1.1). Laws of reflection and refraction at an interface between two media are introduced in section 2.1.2. This part is important for the description of the attenuated total internal reflection infrared spectroscopy in chapter 3. Sections 2.1.3 and 2.1.4 are related to molecular vibrations and some basic considerations of normal modes and infrared active dipole modes. The second part of the chapter is an introduction to hydrogen bonding describing some basic definitions and theoretical insights (sections 2.2.1 and 2.2.2).

2.1 Light-matter interaction [8–14]

2.1.1 Basic considerations

In order to describe the propagation of electromagnetic waves in a medium wave equations are needed that describe the behavior of the electric field $\mathbf{E}$ for a given dipole moment density or polarization $\mathbf{P}$, or the medium response $\mathbf{P}$ for a given $\mathbf{E}$. From Maxwell's equations it is straightforward to derive the wave equation by using the two curl equations. The wave equation for the electric field is:

$$-\nabla(\nabla \cdot \mathbf{E}) + \nabla^2 \mathbf{E} = \frac{1}{c^2}\frac{\partial^2 \mathbf{E}}{\partial t^2} + \frac{1}{\epsilon_0 c^2}\frac{\partial^2 \mathbf{P}}{\partial t^2}, \tag{2.1}$$

where

$$c = \frac{1}{\sqrt{\mu_0 \epsilon_0}}, \tag{2.2}$$

is the velocity of light in vacuum and ϵ_0 and μ_0 are the vacuum constants.

The harmonic plane wave solution of the wave equation for monochromatic light at frequency, ω, is:

$$\mathbf{E}(\mathbf{r}, t) = \mathbf{E_0} \exp \mathrm{i} \left(\mathbf{q} \cdot \mathbf{r} - \omega t \right). \tag{2.3}$$

In homogeneous, isotropic, and nonmagnetic solids the plane wave equation results in a complex wave vector $\hat{q}$,

$$\hat{q} = \frac{\omega}{c} \left[\frac{\epsilon}{\epsilon_0} + \mathrm{i} \frac{\sigma}{\epsilon_0 \omega} \right]^{1/2}, \tag{2.4}$$

where ϵ is the dielectric constant and σ is the conductivity and both are material parameters. A complex refractive index, η, can be defined by

$$\hat{\mathbf{q}} = \frac{\omega}{c} \eta \tilde{\mathbf{q}} \tag{2.5}$$

where $\tilde{\mathbf{q}}$ is a unit vector and

$$\eta = n + \mathrm{i} \kappa, \tag{2.6}$$

with n and κ being the refractive index and extinction coefficient, respectively. The plane wave field in equation 2.3 can be rewritten for absorbing media using equations 2.5 and 2.6.

$$\mathbf{E}(\mathbf{r}, t) = \mathbf{E_0} \exp \left(-\frac{\omega}{c} \kappa \tilde{\mathbf{q}} \cdot \mathbf{r} \right) \exp \left[\mathrm{i} \left(\frac{\omega}{c} n \tilde{\mathbf{q}} \cdot \mathbf{r} - \omega t \right) \right]. \tag{2.7}$$

The solution of the wave equation in a medium is an oscillating wave that decays during propagation; the first exponential in equation 2.7 stands for absorption, the decay of the propagating wave is characterized by the extinction coefficient, κ. The attenuation of the wave can also be described by Beer's law:

$$I = I_0 \exp \left(-\alpha z \right) \tag{2.8}$$

where I_0 is the intensity of the source, α is the absorption coefficient describing the attenuation of the intensity, I, with distance, z.

$$\alpha = \frac{2\omega\kappa}{c} = \frac{\sigma}{\epsilon_0 c n} \tag{2.9}$$

From equation 2.9 results that the attenuation is governed by the imaginary part of the complex refractive index. The second exponential in equation 2.7 is oscillatory and represents the phase velocity of the wave, $\nu = c/n$.

2.1.2 Interfaces [9–11, 13, 15]

Applying boundary conditions at an interface between two media with different refractive indices leads to the laws of reflection and refraction. Light striking an interface is partially reflected and partially refracted. The angle of refraction and the angle of incidence are interrelated by Snell's law:

$$n_1 \sin\theta_1 = n_2 \sin\theta_2, \tag{2.10}$$

In equation 2.10 n_1 is the refractive index of the incident material, θ_1 is the angle of incidence, n_2 is the refractive index of the second material, and θ_2 is the angle of refraction into the second medium (figure 2.1 (a)). Snell's law holds in general: electromagnetic waves, sound waves, water waves. If the refractive index n_1 of the medium from which the light is incident onto the interface is higher than the refractive index n_2 of the second medium, the reflection is called internal. In the opposite case, when n_1 is lower than n_2, the reflection is called external.

The field amplitude ratios of reflected and refracted rays (r and t) to the incident ray (i) are described by the Fresnel equations. For parallel ($\parallel$) polarization ($\mathbf{E}$ parallel to the plane of incidence) and perpendicular ($\perp$) polarization ($\mathbf{E}$ perpendicular to the plane of incidence) (figure 2.1 (b)):

$$r_\parallel = \frac{E_{r\parallel}}{E_{i\parallel}} = \frac{\eta_1 \cos\theta_2 - \eta_2 \cos\theta_1}{\eta_1 \cos\theta_2 + \eta_2 \cos\theta_1} = -\frac{\tan(\theta_1 - \theta_2)}{\tan(\theta_1 + \theta_2)} \tag{2.11}$$

$$r_\perp = \frac{E_{r\perp}}{E_{i\perp}} = \frac{\eta_1 \cos\theta_1 - \eta_2 \cos\theta_2}{\eta_1 \cos\theta_1 + \eta_2 \cos\theta_2} = -\frac{\sin(\theta_1 - \theta_2)}{\sin(\theta_1 + \theta_2)} \tag{2.12}$$
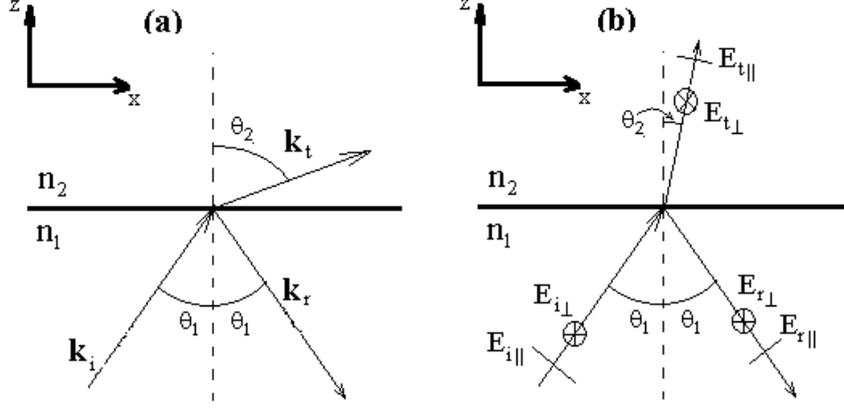
Fig. 2.1: (a) Light reflection and refraction across a boundary illustrated for internal reflection ($n_1 > n_2$). (b) Illustration of the electric field as a function of polarization for the discussion of Fresnel equations (general case of external reflection, $n_1 < n_2$).

$$t_\parallel = \frac{E_{t\parallel}}{E_{i\parallel}} = \frac{2\eta_1 \cos\theta_1}{\eta_2 \cos\theta_1 + \eta_1 \cos\theta_2} = \frac{2\sin\theta_2 \cos\theta_1}{\sin(\theta_1 + \theta_2)\cos(\theta_1 - \theta_2)} \qquad (2.13)$$

$$t_\perp = \frac{E_{t\perp}}{E_{i\perp}} = \frac{2\eta_1 \cos\theta_1}{\eta_1 \cos\theta_1 + \eta_2 \cos\theta_2} = \frac{2\sin\theta_2 \cos\theta_1}{\sin(\theta_1 + \theta_2)} \qquad (2.14)$$

Fresnel equations are the result of Maxwell's equations where θ_1 and θ_2 are connected through Snell's law. Different polarizations of light reflect and refract differently (eq. 2.11 - 2.14). The Fresnel amplitude coefficients give the amplitudes and phases of the reflected and refracted electric field as a function of incident angle, polarization, amplitude of the incident electric field, and the complex refractive indices of the two media. At normal incidence, the reflectance, R, and transmittance, T, across a boundary (as in figure 2.1) are

$$R = \left|\frac{E_r}{E_i}\right|^2 = \left|\frac{\eta_2 - \eta_1}{\eta_2 + \eta_1}\right|^2 \qquad (2.15)$$

$$T = \left|\frac{E_t}{E_i}\right|^2 = \frac{4\eta_1^2}{|\eta_2 + \eta_1|^2} \qquad (2.16)$$

2.1.3 Optical properties of solids [8, 13, 14, 16–18]

We assume that the solid has no net macroscopic charge. However, it is composed of positively and negatively charged entities. Applying an electric field $\mathbf{E}$ these entities move in opposite directions producing a dipole moment $p = e^* r$. The quantity e^* is the effective ionic charge and r is the displacement of the charge due to $\mathbf{E}$. Assuming that the charges are elastically bound with a force constant k the restoring force is described by Hooke's law ($\mathbf{F} = -k\mathbf{r}$). By equating these forces, we have

$$e^*\mathbf{E} = -k\mathbf{r}. \tag{2.17}$$

Using Newton's second law, the differential equation of motion for a charged mass is:

$$\mu\frac{d^2\mathbf{r}}{dt^2} + \mu\Gamma\frac{d\mathbf{r}}{dt} + k\mathbf{r} = e^*\mathbf{E} \tag{2.18}$$

where μ is the reduced mass and Γ is a damping constant. For the diatomic molecule with masses m_1 and m_2, presented in figure 2.2, $\mu = \frac{m_1 m_2}{m_1 + m_2}$. We assume that the applied electric field has the form $\mathbf{E} = \mathbf{E_0} exp\left(-i\omega t\right)$. For low intensities of the electromagnetic wave, the
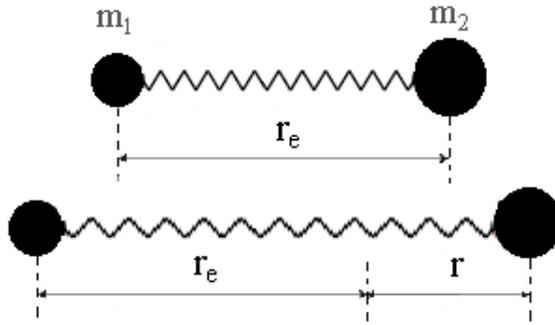
Fig. 2.2: Model for a diatomic molecule with r_e being the equilibrium distance between the atoms, and r being the relative displacement from the equilibrium position (adapted from ref. [8]).

charge motion will have the same time dependence; $\mathbf{r} = \mathbf{r_0} exp\left(-i\omega t\right)$. Solving the equation of motion for fields of frequency ω and introducing the eigenfrequency of the oscillator $\omega_0 = \left(\frac{k}{\mu}\right)^{1/2}$ a relation for the complex refractive index and complex dielectric constant will be obtained:

$$\eta^2 = \frac{\hat{\epsilon}}{\epsilon_0} = 1 + \frac{N(e^*)^2}{\mu\epsilon_0}\frac{1}{\omega_0^2 - \omega^2 - i\Gamma\omega}. \tag{2.19}$$

The resonant frequency ω_0 and the damping constant Γ are strictly related to the medium, and N is the number of charges. From equation 2.19 it follows that the dipole oscillators in a material absorb most efficiently at a frequency of ω_0. The value of ω_0 is influenced by the force constant k (for molecules the force constant k is related to the bond strength) and the value of the reduced mass μ (it means that isotopic substitution of an atom will also affect ω_0).

A typical dispersion curve for n and κ as a function of frequency is presented in figure 2.3. The value of κ goes through a maximum at the resonance frequency ω_0. From equation 2.9 ($\alpha \sim \kappa$) it follows that the absorption coefficient α also goes through a maximum at ω_0. From this relation also follows that in a dielectric medium there are regions which show no absorption if the frequency ω is not near the resonance frequency ω_0. The plot of n versus ω shows that n is gradually increasing with ω, reaching a maximum, then rapidly decreasing to a minimum as it passes through ω_0.
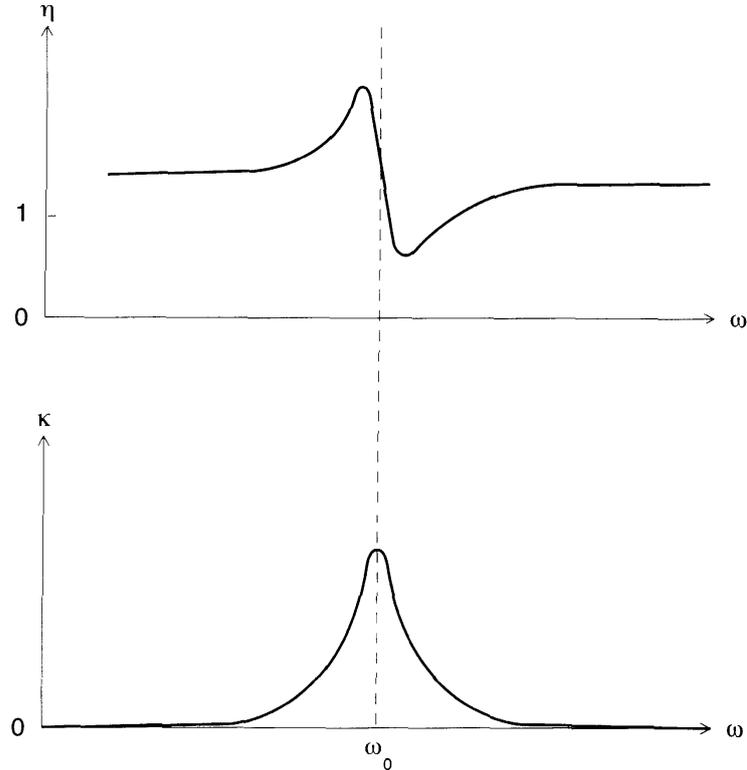
Fig. 2.3: Typical dispersion curves for the real part η and the imaginary part κ of the refractive index as a function of frequency [17].

In practice the material parameters (ϵ, η, α) are not measured directly. Assuming a light beam with known intensity (I_0) incident on the sample, it is possible to measure either the

reflected light (I_R) or the transmitted light (I_T). The intensity of the reflected light is determined by the reflectance R (defined in equation 2.15) through the relation: $I_R = RI_0$. The light which enters the sample may be transmitted through the sample or some part may be absorbed (I_A) by the sample. The intensity I_0 must equal the sum of the intensities of the transmitted, absorbed, and reflected light:

$$I_0 = I_R + I_A + I_T, \tag{2.20}$$

Equation 2.20 can be rewritten:

$$1 = \frac{I_R}{I_0} + \frac{I_A}{I_0} + \frac{I_T}{I_0} = R + \frac{I_A}{I_0} + \frac{I_T}{I_0}, \tag{2.21}$$

where I_A/I_0 represents the absorptivity, and I_T/I_0 represents the transmissivity. The transmittance T is given by the ratio of the transmitted light (I_T) to the light that enters at the front face of the sample ($i_0 = I_0 - I_R$). The transmittance of a pure sample of thickness d is given by Beer's law:

$$T = \frac{I_T}{i_0} = e^{-\alpha d}. \tag{2.22}$$

The absorbance of the sample is given by:

$$A = -\ln T = \alpha d - \ln(1 - R). \tag{2.23}$$

If the reflectance R is considered zero, the absorbance will become:

$$A = -\ln T = \alpha d. \tag{2.24}$$

2.1.4 Molecular vibrations [14, 16, 18]

The frequencies of molecular vibrations in solids are typically in the 20 to 3500 cm^{-1} range. When describing optical interactions with molecular vibrations the basic assumptions are that each atom is located at an equilibrium position in the solid and it can oscillate about this equilibrium position with an amplitude which is small compared to the internuclear distance. Also it is assumed that the response of the outer shell electrons of the atoms

to an electric field is much faster than the response of the core together with its inner electron shells (adiabatic approximation). From these assumptions it follows that the force in Newton's equation depends linearly on the displacements and the system behaves as if all the particles are joined by harmonic springs (figure 2.4). Thus, vibrations can be treated classically and the solution of the equation of motion for atoms in a solid, for small oscillations, can be described in terms of **normal modes**. A normal mode is a correlated motion of the atoms that has a characteristic wave vector (q) and frequency (ω). The resonant frequency of a normal mode depends on the crystal symmetry, atomic separation, interatomic and intermolecular forces. Molecules with N atoms have $3N$ degrees of freedom. Three degrees of freedom are translational motion in mutually perpendicular directions and three are rotational motion. The remaining degrees of freedom are vibrational modes ($3N - 6$ for nonlinear molecules and $3N - 5$ for linear molecules). The path of a normal mode of vibration is described in terms of the normal coordinate Q_i. Every normal mode has a certain type of symmetry associated with it. Normal modes depicted in the normal coordinate system corresponds to bond stretches, bends, and torsions. The normal mode frequencies ω_0 are characteristic of a specific functional group and can be used for material identification.
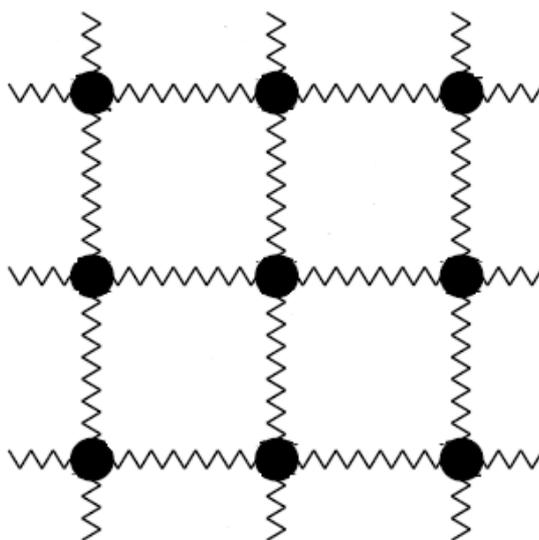
Fig. 2.4: Classical model for molecular vibrations: springs (representing the chemical bonds) and spheres (representing the atoms and ions in a solid) (adapted from ref. [8]).

For a material to show infrared absorption its dipole moment should change during the vibration ($\partial p/\partial Q_i \neq 0$). The larger this change, the more intense the absorption band will be. For the molecules studied during my work (presented in chapter 4), two molecular groups are important: the carbonyl group (C=O) and the amine group (N-H). Because of the difference in electronegativity between the constituents, both groups are permanently polarized. The C=O stretching shows an intense absorption band in the region $1670 - 1740$ cm^{-1}. The amine stretching is observed between $3150 - 3450$ cm^{-1}. In the particular situation of this thesis the exact position of the absorption bands is a function of other intermolecular interactions like hydrogen bonding, van der Waals or stacking forces.

2.2 Introduction to hydrogen bonding

2.2.1 Definitions

"A hydrogen bond exists between a functional group X-H and an atom or a group of atoms Y in the same or a different molecule when (a) there is evidence of bond formation (association or chelation), (b) there is evidence that this new bond linking X-H and Y specifically involves the hydrogen atom already bonded to X." [19]

The above is the definition of the hydrogen bond given by Pimentel and McClellan in 1960. Since then the hydrogen bond field has increased its impact to the research community by the multitude of colors shown in fundamental processes in chemistry, biology, and materials science. This statement is evident if we consider that approximately one new paper is indexed in SciFinder per hour on hydrogen bonding [20]. The tremendous increase in the hydrogen bond related research fields leads scientists from time to time to come out with new, more general definitions in order to cover the whole spectrum of the field. There is a variety of conditions under which hydrogen bonding can occur. The interaction requires two functional groups, one of them must serve as a proton donor (D) and the other as a proton acceptor (A). Usually the proton is donated by a carboxyl, hydroxyl, amine or amide group . Later it was found that protons can be donated by S-H and C-H groups also, but these hydrogen bonds are weaker (1-2 kJ/mol) [19]. At the opposite end extremely strong hydrogen bonds are present in the ion HF$^-_2$ (161.5 kJ/mol) [21]. The

International Union of Pure and Applied Chemistry (IUPAC) defined the hydrogen bond in 1997 as

"... a form of association between an electronegative atom and a hydrogen atom attached to a second, relatively electronegative atom. It is best considered as an electrostatic interaction, heightened by the small size of hydrogen, which permits proximity of the interacting dipoles or charges. Both electronegative atoms are usually (but not necessarily) from the first row of the Periodic Table, i.e., N, O or F. Hydrogen bonds may be intermolecular or intramolecular. With a few exceptions, usually involving fluorine, the associated energies are less than 20-25 kJ/mol (5-6 kcal/mol)..." [20, 22]

Since the IUPAC definition for hydrogen bonds was considered not embracing enough, in 2005 IUPAC set up a core group of 14 crystallographers, spectroscopists, and theoreticians to examine this definition and recommend changes. The final task of their work was a podium discussion on the new definition of the hydrogen bond during the XIX. International Conference on "Horizons in Hydrogen Bond Research" (Göttingen, Germany, September 11 - 17, 2011). Even if the mutual agreement between the core group and the present research community was not full, the new definition was accepted and states:

"A typical hydrogen bond may be depicted as X-H $\cdots$ Y-Z, where the three dots denote the bond. X-H represents the hydrogen-bond donor. The acceptor may be an atom or an anion Y, or a fragment or a molecule Y-Z, where Y is bonded to Z. In specific cases X and Y can be the same with both X-H and Y-H bonds being equal. In any event, the acceptor is an electron-rich region such as, but not limited to, a lone pair in Y or a π-bonded pair in Y-Z." [20, 23]

2.2.2   Theoretical background [24]

The concept of the hydrogen bond evolves from consideration of Pauling's atomic electronegativities (the tendency for an atom to attract a pair of electrons that it shares with another atom). A consequence of the greater electronegativity of X relative to H in an X-H bond is that the hydrogen proton is descreened (it is stripped of some of its electron density). This results in a dipole at the terminus of the X-H bond which interacts with the dipole of the lone pairs on the acceptor atom. Consequently hydrogen bond donor strengths are qualitatively proportional to these differences in electronegativities:

$F-H > O-H > N-H > C-H$. The hydrogen bond has also a directional property, being strongest when $X-H \cdots Y = 180°$. Beyond the electrostatic part other components of the hydrogen bond energy were identified as delocalization, repulsion, and dispersion. The electron distribution of the molecules is disturbed by the close approaches due to the hydrogen bonding. This gives rise to polarization and the quantum mechanical interactions, exchange repulsion, charge transfer, and dispersion. The polarization is the effect of the distortion of the electron distributions of X-H by Y and Y by X-H. This is a stabilizing interaction. The exchange repulsion is the short-range repulsion of the electron distributions of the donor and acceptor groups and accounts for the overlap of charges in occupied orbitals of both donor and acceptor. With the application of the Pauli principle, it is repulsive and is the major destabilizing term. Charge transfer is the result of the transfer of electrons between occupied orbitals on the donor to vacant orbitals on the acceptor and vice versa. The electrostatic, polarization, and charge transfer components are attractive at equilibrium distances while the exchange repulsion is the balancing term.

As an example for O-H $\cdots$ O bonds at O $\cdots$ O = 2.8 Å, the electrostatic component contributes about 65% of the hydrogen bond energy. As the O $\cdots$ O distance becomes closer, the quantum mechanical charge transfer contributions become more important. For longer weak bonds, the interaction becomes more electrostatic.

3. Materials and Methods

3.1 Hydrogen bonded supramolecular systems

3.1.1 Synthesis

Details regarding the synthesis of molecular modules are beyond the scope of this thesis. Molecules presented in figure 3.1 were prepared by collaborators at the University of Trieste, Italy, and at the University of Namur, Belgium, according to previously published procedures[1, 25–27].
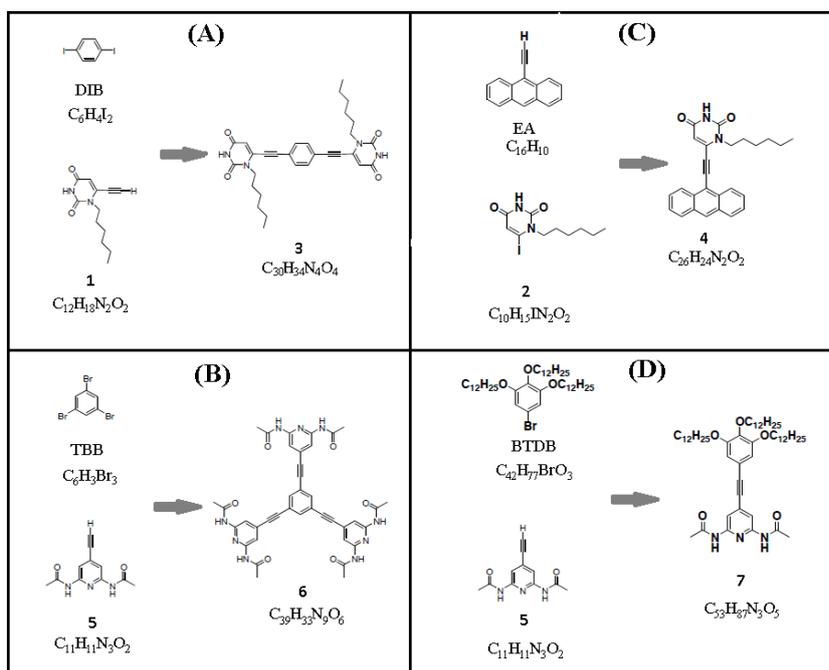
Fig. 3.1: Synthesis steps of the different molecules. Notation of the molecules: (**A**) - **DIB** - 1,4-diiodobenzene, **1** - 1-hexyl-6-ethynyl uracil, **3** - 1,4-bis[(1-hexylurac-6-yl)ethynyl]benzene; (**B**) - **TBB** - 1,3,5-tribromobenzene, **5** - 4-ethynyl-2,6-di(acetylamino)pyridine, **6** - 1,3,5-Tris-[(2,6-Di(acetylamino)pyridine-4-yl-)ethynyl]benzene; (**C**) - **EA** - 9-Ethynyl-anthracene, **2** - 1-hexyl-6-iodouracil, **4** - 1-hexyl-6-[(anthracen-9-yl)ethynyl]uracil; (**D**) - **BTDB** - 1-Bromo-3,4,5-tri(dodecyloxy)benzene, **5** - 4-ethynyl-2,6-di(acetylamino)pyridine, **7** - 2,6-Di(acetylamino)-4-{[3,4,5-tri(dodecyloxy)phenyl]ethynyl}pyridine.

3.1.2 Methods

Fourier transform infrared spectroscopy [28]

Fourier transform infrared spectroscopy (in the rest of the thesis just infrared spectroscopy) has found wide applications in the last decades. The design of an infrared spectrometer is based on that of the two-beam interferometer (designed by Michelson). The main advantage is that the whole spectrum is recorded during the measurement time (not just a region limited by resolution as in double-beam grating infrared spectrometers). The Michelson interferometer represented in figure 3.2 consists of a fixed mirror, a moving mirror and a beamsplitter. Light from a source is separated into two parts by the beamsplitter. After reflection by the two mirrors the two beams recombines at the beamsplitter. The output beam of the interferometer is recorded as a function of path difference, and is an interferogram. The infrared spectrum can be obtained by calculating the Fourier transform of the interferogram. Assuming a light source with intensity, $I_0(\omega)$, the electric fields of the two interfering beams are

$$E_1 = \sqrt{I_0(\omega)}\sin\omega t; \quad E_2 = \sqrt{I_0(\omega)}\sin\left(\omega t + \frac{2\omega x}{c}\right) \tag{3.1}$$

where x is the mirror displacement. The time-averaged intensity measured by the detector has an x dependence

$$dI(\omega, x) \propto \left(|E_1 + E_2|^2\right) d\omega. \tag{3.2}$$

As all light frequencies are simultaneously processed, the detector measures the following intensity as a function of mirror position x:

$$I(x) = \int dI = \int_0^\infty I_0(\omega)d\omega + \int_0^\infty I_0(\omega)\cos\frac{2\omega x}{c}d\omega. \tag{3.3}$$

The first term gives a constant (independent of x) while the second term represents the Fourier transform of the spectrum $I_0(\omega)$. An infrared spectrum measurement has the following steps: intensity $I(x)$ is measured as a function of the mirror position x, then by Fourier transformation the single-beam spectrum $I_0(\omega)$ is obtained. $I_0(\omega)$ is composed of the spectrum of the source and the frequency-dependent response of the detector. The resolution $\Delta\omega$ is a function of the maximum mirror movement: $\Delta\omega/c \simeq 1/x_{max}$. To measure

the transmission of the sample, the single-beam spectrum of the reference and the sample has to be recorded (I_r and I_s),

$$T = \frac{I_s}{I_r}. \tag{3.4}$$
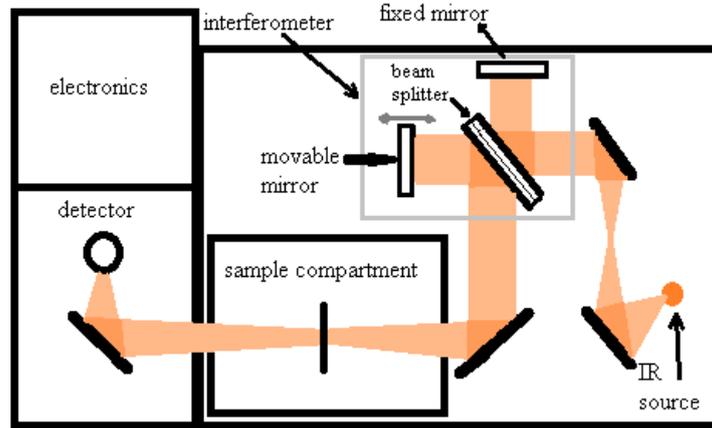
Fig. 3.2: Schematic illustration of a Bruker IFS 66v Fourier transform infrared spectrometer.

Infrared spectra in the solid state were recorded in powders ground in potassium bromide (KBr) pellets. Reference pellets were pure KBr. Mixing the sample with KBr dilutes the material so it becomes transparent to infrared light, but the grain size in the pellets ($\sim 1~\mu m$) ensures that they still can be regarded as solids, preserving the structure. The sample:KBr mass ratio was approximately 1:400 (around 1 mg sample mixed with 400 mg of KBr powder). Prior starting an experiment the KBr powder was kept in a drying oven at 350 K for five hours to assure the anhydrous state of the powder. The size of the KBr/sample pellet was 13 mm and a load of 6 to 7 tons on the press gauge produced a disc of approximately 1 to 1.5 mm thickness. Temperature dependent measurements were performed in an optical cryostat (Advanced Research Systems) under dynamic vacuum conditions (10^{-3} mbar) starting from room temperature up to a temperature value characteristic to each sample (typically up to 370 - 550 K). Two different infrared spectrometers were used, a Bruker Tensor 37 and an IFS66v for the temperature dependence with 2 cm^{-1} resolution. All spectra were taken in the 400 - 4000 cm^{-1} range with a Ge/KBr beamsplitter and mercury-cadmium-telluride (MCT) detector. The light source was a Globar (SiC rod) which is a thermal light source. For some samples far-infrared spectra in the 50-400 cm^{-1} range were also measured in polyethylene discs. Far-infrared beamsplitters are made of

Mylar thin films while the detector is deuterated tri-glycine sulfate (DTGS). The baseline was corrected by an adjusted polynomial function.

Matrix isolation infrared spectroscopy

The matrix isolation (MI) technique has been developed by Pimentel and collaborators and represents a powerful technique in investigation of hydrogen bonds [19]. A gaseous mixture of the studied material is quickly frozen in a large amount of inert gas (e.g. argon, nitrogen, neon, krypton or xenon). Under such circumstances no diffusion can occur and the inert gas forms a rigid matrix that isolates the molecular constituents of the substance (figure 3.3). Isolated molecules are devoid of collisions and rotations and the infrared band linewidths are almost one order of magnitude narrower than that observed in condensed phase.
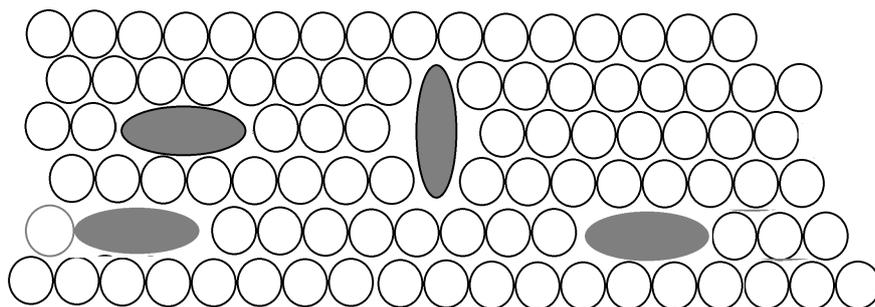
Fig. 3.3: Matrix isolation scheme. The rigid matrix of inert gas (shown as open circles) isolates molecules from each other preventing the formation of hydrogen bonds.

In my experiments I used a home made matrix isolation setup in the Laboratory of Molecular Spectroscopy, Eötvös Loránd University, Budapest. The setup is described in details elsewhere [29, 30]. Briefly, the evaporated sample was mixed with argon (Messer, 99.9997%) before deposition onto an 8-10 K CsI window. The gas flow was kept at 0.07 mmol min^{-1}, while the evaporation temperature was optimized to get the shortest possible deposition time and keep the concentration low enough to minimize the formation of dimers during deposition. MI spectra were recorded using a Bruker IFS 55 spectrometer with 1 cm^{-1} resolution and DTGS detector. Under these circumstances, the sample consists predominantly of isolated molecules, with only a small amount of aggregated species

present. Therefore, comparing MI spectra with solid-state KBr pellet spectra allows us to study the effect of aggregation.

Ab initio molecular dynamics calculations

Theoretical calculations presented in my thesis were done in collaboration with Dr. Jonas Bjork, Dr. Felix Hanke and Prof. Mats Persson from University of Liverpool and with Péter Nagy from Eötvös Loránd University, Budapest. The theoretical results are presented in combination with the experimental data in chapters 4.3.2 [2] and 4.3.3 [3].

3.1.3   Infrared spectra of hydrogen bonds

Considering now the infrared spectra of a hydrogen bonded species X-H $\cdots$ Y-Z we will find very characteristic changes in the X-H and Y-Z stretching region [19, 31]. In particular the formation of the hydrogen bond introduces a very unusual change in the frequency and intensity distribution in the IR absorption spectrum. The disturbances are so distinctive that infrared spectra provide one of the most powerful methods to reveal the presence of hydrogen bonds [19].

Vibrational modes affected by the presence of hydrogen bonds are presented in figure 3.4. The main effect related to the presence of hydrogen bonds is a spectral shift of the absorption of the *X-H* stretching vibrational mode to lower wavenumbers [19]. Another important effect related to the stretching mode is the broadening of the bands and increase in the intensity of the vibrational bands. The bending modes *X-H* show different characteristics: spectral shift in the presence of hydrogen bonds is in the direction of higher wavenumbers and the magnitude of the shift is usually smaller than that of the stretching mode [19]. In the mid-infrared region isotopic substitution of hydrogen to deuterium shows important modifications in the spectrum. The spectral shift caused by the mass number changing is proportional to the square root of the isotopic masses. In the case of hydrogen to deuterium change the isotopic shift is approximately $\frac{1}{\sqrt{2}}$.

The far-infrared region is defined as the region between 20-400 cm^{-1} and usually provides information regarding the vibrations of molecules containing heavy atoms and molecular skeleton vibrations. However, another aspect related to the far-infrared region is the possibility of direct observation of the vibration of hydrogen bonds [32]. The stretching (ν_σ)

ν_s X ←—H—→ · · · Y   X—H stretch
         R   (3500–2500 cm^{-1})

ν_b X———-H · · · · · · · Y   R—X—H bend (in-plane)
         R   (1700–1000 cm^{-1})

ν_t X———HⓞO · · · · · Y   R—X—H torsion [a] (out-of-plane)
         R   (900–300 cm^{-1})

ν_σ X———H · · · ←—Y—→   X · · · · Y stretch
         R   (250–50 cm^{-1})

ν_β X———H · · · · · · · Y   X—H · · · Y bend
         R   (<50 cm^{-1})

[a] The symbol Ⓞ indicates a vibrational movement of the hydrogen atom perpendicular to the RXY plane.
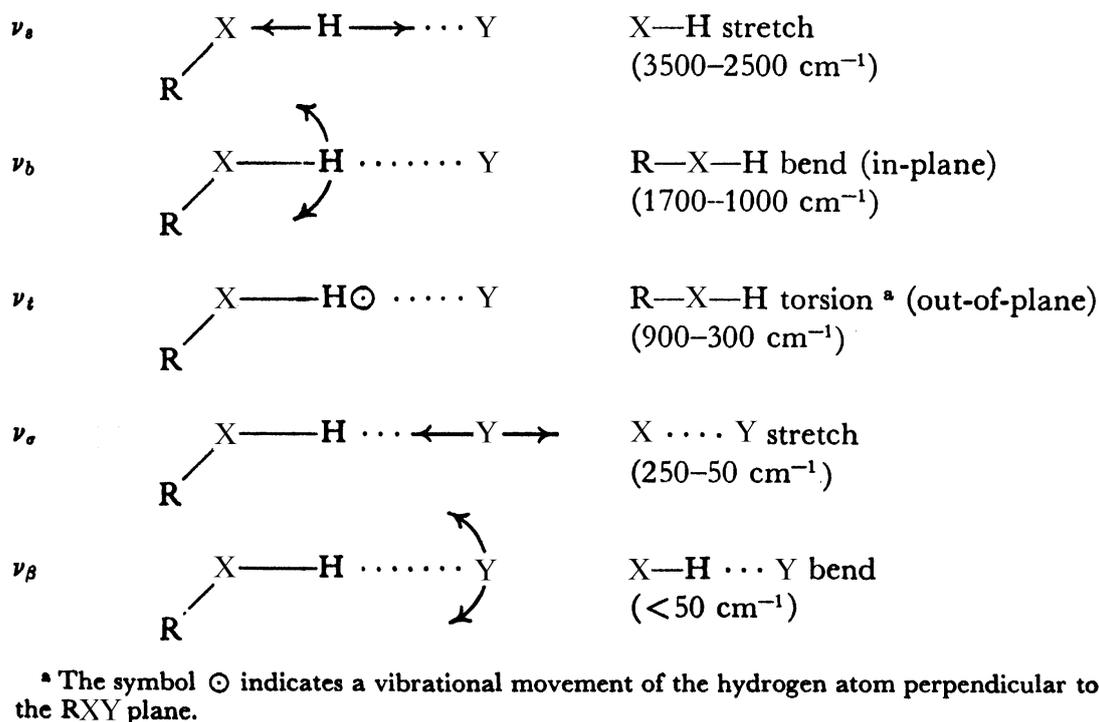
Fig. 3.4: Vibrational modes of a hydrogen bonded complex. Subscripts s, b and t are assigned to stretching, bending and torsion vibrations, respectively while subscripts σ and β represents the stretching and bending vibrational modes in the far-infrared region created by the formation of the hydrogen bonded complex. (adapted form ref. [19])

and bending (ν_β) vibration of a hydrogen bond in the far-infrared region is illustrated in figure 3.4. The values of ν_σ reported in the literature fall in the spectral range 75-250 cm^{-1} [32–34]. In contrast to the mid-infrared region, in the far-infrared part of the spectrum conventional isotopic substitution is of little value in confirming the presence of hydrogen bonds [32]. Since the entire masses of both molecules are involved in the vibration of hydrogen bonds the frequency shift is only 2-3 cm^{-1}. Such a spectral shift is within the experimental uncertainty of the location of band centers [32].

In this thesis, instead of isotopic substitution, hydrogen bonds were studied by their temperature dependence.

3.2 Silicon carbide quantum dots

3.2.1 Synthesis

SiC quantum dots were prepared by Dávid Beke and István Balogh at the Wigner Research Centre for Physics according to previously published procedures [4, 35, 36]. The term quantum dot is used because the size reduction induces a shift of the electronic excitations to higher energies in comparison to the starting bulk material. Another effect of the size confinement is a large surface to volume ratio which yields a complex surface structure conferring unique vibrational, photonic and electronic properties. Figure 3.5 shows a typical high-resolution transmission electron microscopy (HRTEM) image of SiC quantum dots. The HRTEM image reveals that SiC quantum dots are nearly spherical, and the typical lattice spacing of 0.25 nm corresponds to the (111) plane of 3C-SiC. Though the detectability of oxide or carbon contaminants is limited by the presence of the carbon film substrate, the sharp contrast of the quantum dots indicates that there is no significant contamination on the surface of SiC quantum dots.
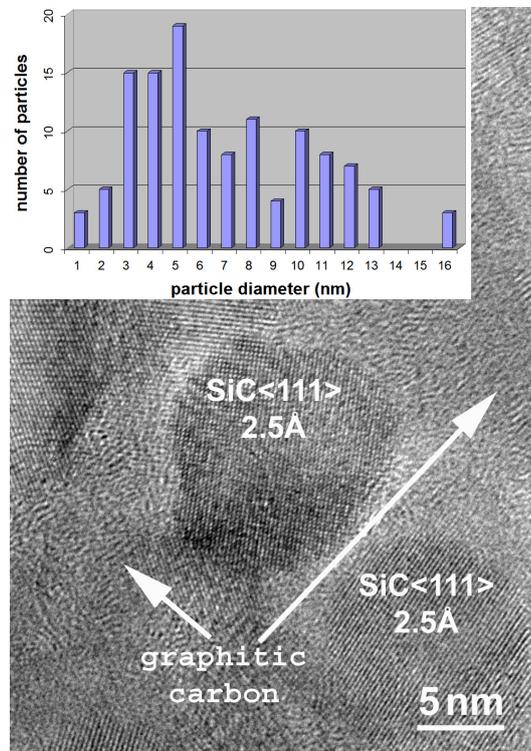
Fig. 3.5: HRTEM image and size distribution of SiC quantum dots. The average size is 4.8 nm [4], while the lattice spacing is 0.25 nm (HRTEM measurements performed by Zsolt Czigány).

3.2.2 Surface sensitive infrared spectroscopy [9–11, 15]

Due to the broad range of the potential samples a multitude of spectroscopic techniques is necessary for a proper investigation. Usually, liquids are analyzed by transmission or attenuated total reflection (ATR), gaseous samples are best investigated by transmission, powders by ATR or diffuse reflectance (DRIFT). In the past transmission spectroscopy was the dominant technique, however, the special requirements for infrared spectroscopy to detect very weak signals of thin film layers or surface termination sites lead to an increase of using surface sensitive techniques like ATR or reflection-absorption spectroscopy (RAIRS). Here I will provide a short description about the connection between ATR spectroscopy and the physical phenomena of internal reflection, and the role of the evanescent wave is also reviewed.

The main difference between normal transmission spectroscopy and surface sensitive methods (ATR, RAIRS) relies on the presence of a substrate for surface sensitive methods (silicon (Si), germanium (Ge), zinc sulfide (ZnS), zinc selenide (ZnSe), thallium bromoiodide (KRS5) or diamond for ATR and metallic surfaces like gold (Au), silver (Ag) or copper (Cu) for RAIRS).

The basic physical phenomena of ATR is related to the reflectance of an interface (introduced in chapter 2.2), which is a well-understood phenomenon [9–11, 15].

In the case of internal reflection ($n_1 > n_2$, figure 2.1 (a)) at incident angles corresponding to angles of refraction less than 90^0 the light is refracted through the interface. For the case of internal reflection (and only for this case) the incident angle can be increased beyond the maximum angle of refraction resulting in the total reflection of the incident radiation within the higher refractive index medium (optically denser medium). The angle at which the incident radiation is no longer refracted through the interface is called the critical angle. From Snell's law it follows that the critical angle is:

$$\theta_c = \arcsin\left(\frac{n_2}{n_1}\right),$$ (3.5)

In order to eliminate the refraction angle from Fresnel equations and to obtain amplitude coefficients containing only sample parameters and incident geometry Snell's law 2.10 is substituted in equations 2.11 and 2.12:

$$r_{\parallel} = -\frac{\frac{\eta_2{}^2}{\eta_1}\cos\theta_1 - \sqrt{\eta_2{}^2 - \eta_1{}^2\sin^2\theta_1}}{\frac{\eta_2{}^2}{\eta_1}\cos\theta_1 + \sqrt{\eta_2{}^2 - \eta_1{}^2\sin^2\theta_1}} \tag{3.6}$$

$$r_{\perp} = \frac{\eta_1\cos\theta_1 - \sqrt{\eta_2{}^2 - \eta_1{}^2\sin^2\theta_1}}{\eta_1\cos\theta_1 + \sqrt{\eta_2{}^2 - \eta_1{}^2\sin^2\theta_1}} \tag{3.7}$$

This new form of Fresnel equations is meaningful for the case of internal reflection, but also for complex refractive indices. For reasons of practical interest only the case of non-absorbing incident medium ($\eta_1 = n_1$ and is real) is treated. The complex refractive index of the second medium η_2 is:

$$\eta_2 = n_2 + i\kappa_2, \tag{3.8}$$

n_2 and κ_2 are the refractive index and extinction coefficient of the second medium, respectively. If the angle of incidence is greater than the critical angle, the value under the square root becomes negative and the square root becomes imaginary. Thus the Fresnel reflection coefficients 3.6 and 3.7 become complex numbers and the reflectance of the interface is total. This is an indication that there is no electromagnetic field beyond the interface. However, a very special kind of electromagnetic field, the evanescent field is established near the interface.

The evanescent field

To a first approximation the evanescent wave can be taken as a remnant of the transmitted wave. Following the electric field of the transmitted wave (according to the geometry of figure 2.1 (a)):

$$\mathbf{E_t}\left(\mathbf{r}, t\right) = \mathbf{E_t}\left(0, t\right) e^{i\eta_2\mathbf{k_t}\mathbf{r}} \tag{3.9}$$

where $\mathbf{k}_t$ is the wave vector of the transmitted wave, $\mathbf{r}$ is the position vector in which we are observing the field, and the interface is in the x-y plane. The scalar product in the exponential term can be written as:

$$\mathbf{k_t}\mathbf{r} = k_{t_x}x + k_{t_y}y + k_{t_z}z \tag{3.10}$$

The x and y terms in 3.10 represents the propagation in the x-y plane. The z term can be written as:

$$\eta_2 k_{tz} = \eta_2 k \cos \theta_2 = k\sqrt{\eta_2{}^2 - \eta_1{}^2 \sin^2 \theta_1} \tag{3.11}$$

The term $\cos \theta_2$ is meaningful in internal reflection only in the situation when the angle of incidence is smaller than the critical angle. The use of Snell's law permits the extension of equation 3.11 to the region where the angle of incidence exceeds the critical angle (region of ATR spectroscopy). The square root in equation 3.11 is positive and real when $\theta_1 < \theta_c$. In this situation the propagation along the z axis is oscillatory and the expression describes the refracted radiation. When the angle of incidence reaches the critical value, the value of the square root becomes negative and the term becomes imaginary. Equation 3.9 becomes:

$$\mathbf{E}\left(x, y, z, t\right) = \mathbf{E}\left(0, 0, 0, t\right) e^{i(k_x x + k_y y)} e^{-k_z \sqrt{\eta_1{}^2 \sin^2 \theta_1 - \eta_2{}^2}} \tag{3.12}$$

Equation 3.12 describes the evanescent wave that propagates in the x-y plane, while the magnitude of the electric and magnetic field is attenuated exponentially in the z direction away from the interface. This is called an inhomogeneous plane wave and has a peculiar property: the wave is not transverse but has a component of the field parallel to the wave vector $\mathbf{k}$ (figure 3.6).
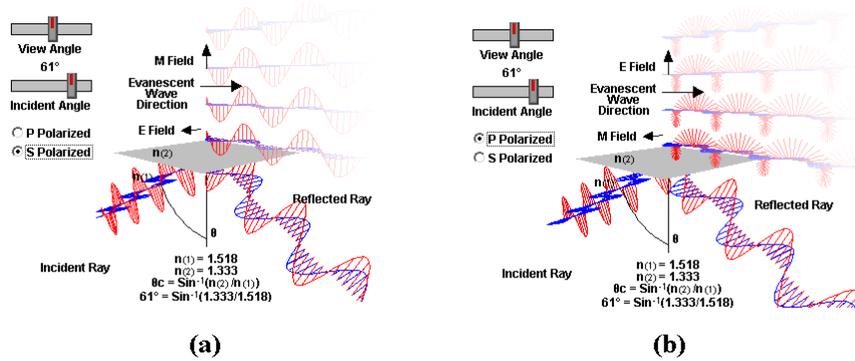
Fig. 3.6: Evanescent wave intensity at the interface surface is a function of both the incident angle and the polarization components of the light beam. The incident light ray is total internal reflected at a glass/water interface having refractive indices of 1.518 and 1.333, respectively. The electric and magnetic field components of the evanescent waves for *s*- (a) and *p* polarization (b) of the incident radiation [37].

Attenuated total internal reflection spectroscopy

An ATR spectrum is obtained by measuring the interaction of the evanescent wave with the sample. Figure 3.7 shows a schematic representation of the horizontal ATR setup used in my work. Placing an absorbing material on the surface of an ATR crystal, the evanescent wave will be absorbed by the sample and its intensity will be attenuated in those regions where the sample absorbs. An ATR spectrum is produced by the attenuated radiation as
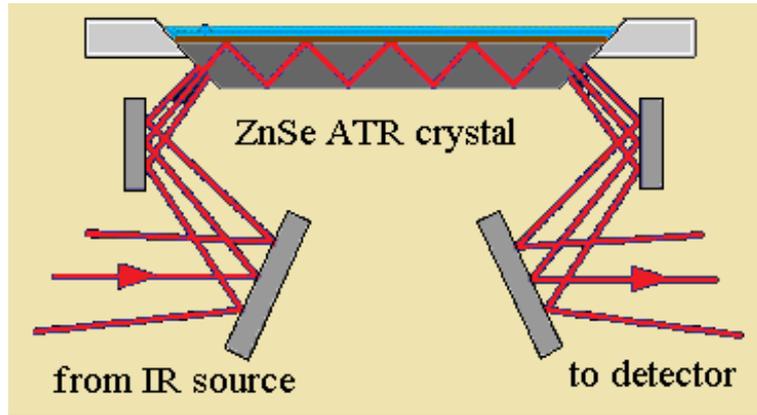
Fig. 3.7: Schematic representation of the horizontal ATR setup for liquids used during my work (adapted from ref. [38]).

a function of wavenumber and is similar to the conventional absorption spectrum. There are some differences related to band intensities at lower wavenumbers. The reason is due to the dependency of the penetration depth of the evanescent field on wavenumber. The penetration depth can be calculated from the wavelength of the incident radiation, λ, the refractive index of the internal reflection element (IRE), n_1, the refractive index of the sample, n_2, and the angle of incidence, θ_1 [18]:

$$d_p = \frac{\lambda}{2\pi n_1 \sqrt{\sin^2\theta_1 - \left(\frac{n_2}{n_1}\right)^2}}.$$
(3.13)

The penetration depth can be controlled with the refractive index of the IRE element and the angle of incidence [18]. Table 4.1 presents this dependence for two ATR crystals used during my work.

I will end this part with an experiment presenting a comparison between ATR and transmission spectroscopy. Figure 3.8 presents the spectrum of a hydrogenated silicon (Si) ATR crystal measured both in ATR and transmission mode (the geometry of the measurement

Tab. 3.1: Penetration depths (in μm) as a function of angle of incidence at 1000 cm-1 for $n_2 = 1.5$

IRE material	30^0	45^0	60^0
Ge	1.2	0.66	0.51
ZnSe	-	2.0	1.1

is presented in the figure 3.8). The size of the Si ATR crystal was 50x20x2 mm (LxWxT), the number of internal reflections 45. The hydrogenation of the Si surface was performed according to a procedure described elsewhere [39]. We consider the hydrogenated surface of the Si ATR crystal as a model for an atomic monolayer. The two bands seen in the
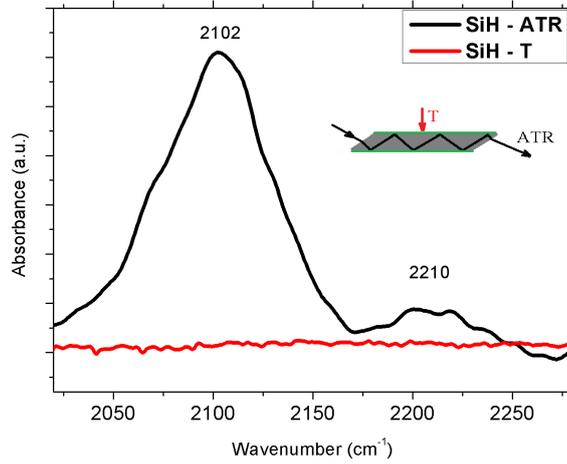
Fig. 3.8: Hydrogenated Si ATR crystal measured in ATR (black curve) and transmission mode (red curve). The measurement technique is visualized in the figure.

ATR spectrum in figure 3.8 are assigned to the Si-H vibrations of SiH and SiH$_2$ groups. Measuring the same surface in transmission mode the spectrum is empty, the transmission technique is not sensitive enough to detect such weak signals. These results prove the potential of ATR in detecting surface related signals. An accurate measurement of the surface structure of SiC quantum dots has represented a central issue during my work as surface terminations play an important role in its physical and chemical properties. During synthesis procedures SiC quantum dots are suspended in different solvents (water, ethanol or methanol) and form colloidal solutions (a colloidal solution is a liquid mixture in which the particles do not dissolve, but rather become equally dispersed throughout the solvent). For the ATR measurements drop drying method was used to cover the surface of the IRE

element with SiC quantum dots. ATR spectra were measured after solvent evaporation. These results are described in chapter 5.3.

3.2.3 Photoluminescence spectroscopy [40, 41]
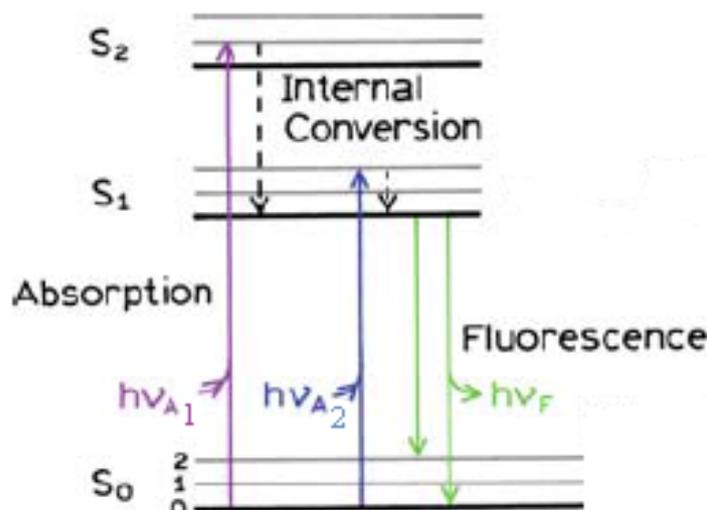
Fig. 3.9: The Jablonski diagram for photoluminescence. S_0 is the ground singlet electronic state, S_1 and S_2 are the higher energy excited singlet electronic states. $0, 1, 2$ are vibrational energy levels (adapted from ref. [40]).

Photoluminescence (PL) is a photon emission process that occurs during relaxation from electronic excited states. Such processes involve transitions between electronic and vibrational states of the fluorescent materials. Processes that occur between the absorption and emission of light are usually illustrated by Jablonski diagrams. Figure 3.9 shows a typical Jablonski diagram for fluorescence.

The transitions between states are depicted as vertical lines to illustrate the instantaneous nature of light absorption (Frank-Condon principle). Transitions occur in about 10^{-15} s, a time too short for significant displacement of nuclei. At room temperature the thermal energy is not enough to considerably populate the excited vibrational states. Absorption and emission occur mostly from the lowest vibrational energy states. Following light absorption, a fluorophore is usually excited to some higher vibrational level of S_1 or S_2. Fluorophores in condensed phases relax rapidly to the lowest vibrational energy level

of S_1 (internal conversion). Generally, such relaxation processes are complete prior to emission (internal conversion occurs within 10^{-12} s while fluorescent lifetimes are much longer, in the order of 10^{-8} s). Return to the ground state typically occurs to a higher excited vibrational level, which then quickly reaches thermal equilibrium.
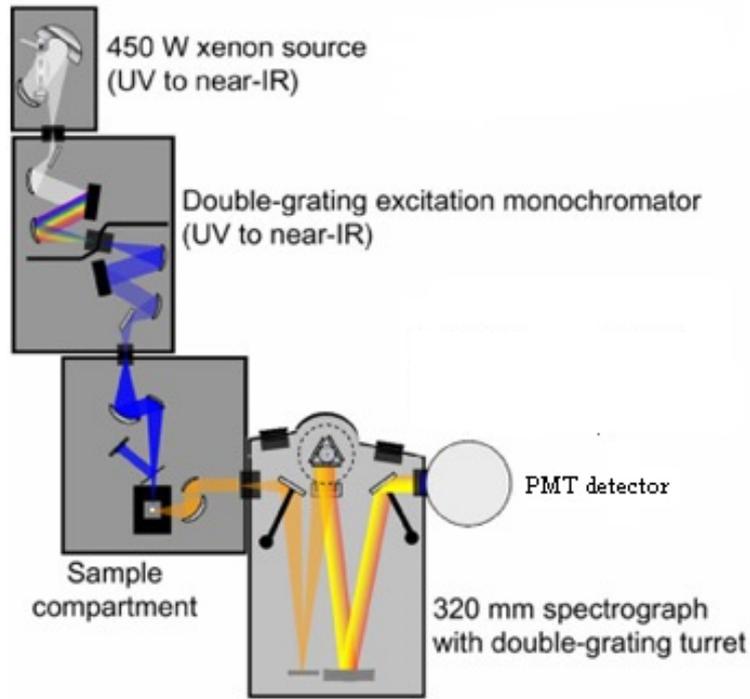
Fig. 3.10: Schematic representation of a Horiba Jobin Yvon Nanolog spectrofluorometer (adapted from ref. [41]).

During my work I have used photoluminescence spectroscopy to study the emission properties of the SiC quantum dots. Photoluminescence spectra were recorded with a HORIBA Jobin Yvon Fluorolog-3 spectrofluorometer (Nanolog) presented in figure 3.10. The samples were measured in colloidal aqueous solution (concentration approx. 0.5 mg/ml).

4. Infrared spectroscopy of hydrogen bonded supramolecular systems

4.1 Introduction

The formation and breaking of hydrogen bonds is one of the most fundamental processes in biology, chemistry, and materials science. For example, hydrogen bonding is responsible for the formation of the DNA double helix and for the highly unusual phase diagram of water or the secondary and tertiary structures in proteins; it is therefore at the very heart of life sciences. Furthermore, with the continuous down-scaling of technology in mind, the self-assembly and molecular recognition properties of hydrogen bonds have found their way into the fabrication of nanoscale materials and devices [42]. It is therefore imperative to understand the microscopic mechanisms that lead to the formation and dissolution of hydrogen bonds, in particular their temperature dependence. These processes are primarily driven by thermal fluctuations, which are particularly large in hydrogen bonded systems as they include very light atoms, and a relatively shallow and anharmonic potential energy well.

To study this process in a simple and controlled manner, numerous different systems have been suggested - for example short polypeptide segments [43, 44] or custom-designed molecular modules [45–48]. In this context, it is crucial to have detailed information from both experiment and theory so that the observed thermal fluctuation effects can be properly assigned. Systems that are particularly suited for the controlled study of hydrogen bond formation are small cyclically bonded nucleic base pairs, which play an important role as basic building blocks in both biology and nanotechnology [42]. Due to the many functional groups of such purines and pyrimidines taking part in hydrogen bonds, there are many ways

that both homomolecular [49] and heteromolecular pairing can be exploited, for instance in defect-free 2D supramolecular network formation with long range order [1, 50, 51].

The main requirement and at the same time the main challenge in molecular-based devices is the control of the materials at the nanoscopic level [52]. This control can be made through self-organization or self-assembly by non-covalent interactions ending up with controlled formation of higher order architectures from small building blocks. Even though extensive work has been published on the study of self-organization of molecular building blocks over an extended length scale [53–56], the preparation of self-assembled macroscopic materials is still far from the fabrication of supramolecular systems usable for applications in industry. On the other hand there are clear advantages for the "bottom-up" approach through weak supramolecular interactions (hydrogen bonds, dipole-dipole interactions, dispersion forces) as they include the simultaneous assembly of the predetermined molecular units, long-range order and the possibility of defect-free structures. Also the energy of these weak interactions between the supramolecular constituents is comparable to the thermal energy slightly above room temperature so such systems are very dynamic: weak interactions can be broken and formed back again within very short time scales [57].

The main structural characterization method of hydrogen bonded systems is scanning tunneling microscopy (STM) as it permits the visualization of the self-assembled two-dimensional (2D) structures. In contrast, my work was performed in solid-state (powder) samples, but as I will present later, my results also proved the supramolecular ordering of the molecular constituents.

This chapter is organized as follows: section 4.2 starts with the description of a supramolecular approach for the preparation of hydrogen bonded porous nanostructures followed by a brief literature overview of formation of supramolecular networks. Section 4.3 and 4.4 presents my work on the study of solids with homo- and heteromolecular ordering through formation of hydrogen bonds.

4.2 Hydrogen bonded networks

The formation of supramolecular networks through hydrogen bonding interaction between the components represents one of the main strategies to form two dimensional molecu-

lar structures [1, 25, 26, 42, 46, 47, 58–65]. An important possibility of forming hydrogen bonded networks is the design and synthesis of multivalent molecular modules which expose at their peripheries complementary recognition sites [27]. It is possible to assemble supramolecular networks from different shaped building units: linear units with the reactive sites positioned at 180^0 relative to each other, and angular units with either two-fold or higher symmetry axes. The geometry of each assembled system will be therefore dictated by the angularity of the non-linear components, while the size of the domains will be determined by the linear units (figure 4.1) [27].
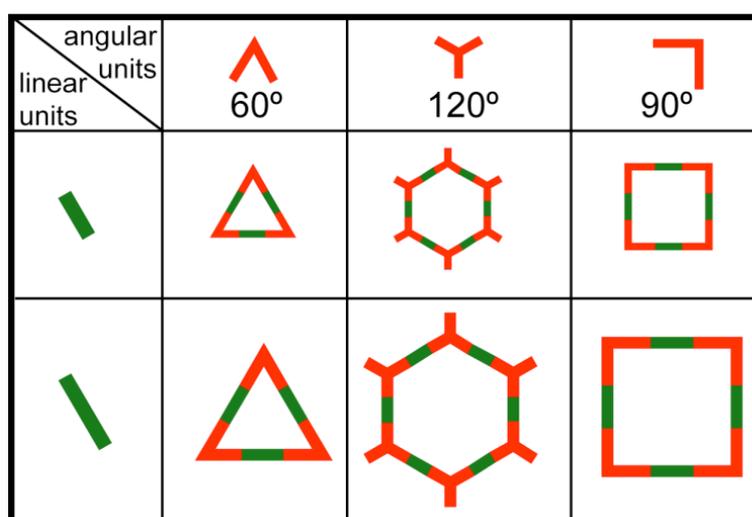
Fig. 4.1: Supramolecular approach for the preparation of hydrogen bonded porous nanostructures [27].

One of the first examples of the formation of a mesophase through hydrogen bonding was reported by Yang *et al.* [66]. They present evidence of self-assembly between a barbituric acid derivative molecule (B) and a melamine derivative molecule (M) (figure 4.2 (a)). The supramolecular assembly (B·M) is possible through triple hydrogen bonds and possible applications in liquid crystals are expected.

The temperature dependent infrared spectra of the (B·M) complex are shown in figure 4.2 (b) and (c). The N-H stretching bands of (B·M) (3402, 3351, and 3310 cm^{-1}) are different from those of the self associated constituents (B) and (M) (3198 cm^{-1}, and 3360 and 3268 cm^{-1}, respectively). Such changes suggest the presence of triple complementary hydrogen bonds between (B) and (M). Analysis of the spectra between 1100 - 1800 cm^{-1} also
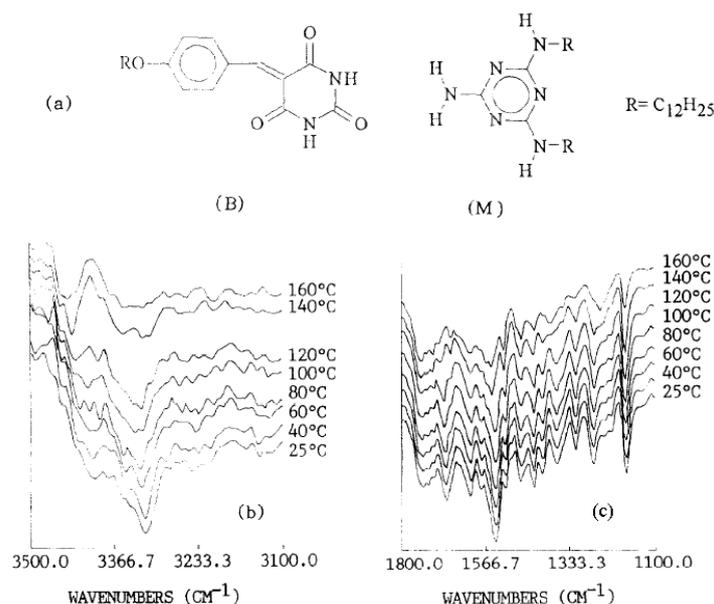
Fig. 4.2: (a) photoactive barbituric acid derivative, 5-[4-dodecyloxybenzylidene]-2, 4, 6,-(1H, 3H)-pyriminidinetrione (B) and melamine derivative, 4-amino-2, 6-didodecylamino- 1, 3, 5-triazine (M). (b) and (c) present the temperature dependent infrared spectra of (B·M) between 3100 - 3500 cm^{-1} and between 1100 - 1800 cm^{-1} (adapted from ref. [66]).

supports this conclusion. At elevated temperatures the molecular self-assembly is destroyed as a consequence of the melting of hydrogen bonds.

Other examples of supramolecular ordering involve the formation of honeycomb networks from the co-deposition of perylene tetra-carboxylic di-imide (PTCDI) and melamine (1,3,5-triazine-2,4,6-triamine) on a silver terminated silicon surface [60], or from the co-deposition of a bis-functionalised uracyl-bearing linear molecule (**1** - left part of figure 4.3) and melamine (**MEL**) at the solid-liquid interface on highly oriented pyrolytic graphite (HOPG) surface [46]. Such empty hexagonal lattices are able to host different types of molecular guests such as fullerenes [60].

The right part of figure 4.3 presents the self-recognition of complementary molecules *via* triple hydrogen bonds. Several aspects were found to be crucial in the formation of highly ordered and preprogrammed porous networks at the solid-liquid interface: at high concentration only melamine molecules were physisorbed on HOPG and honeycomb assemblies were obtained only with rather diluted solutions. Another aspect is related to the peripheral functionalization of the linear molecule which is needed to avoid strong side-to-side interactions between the molecules. Such bicomponent self-assembled monolayers

34

were used to gain detailed insights into phase segregation and polymorphism in two dimensional supramolecular systems by exploring the contribution of hydrogen-bond energy and periodicity, molecular flexibility, concentration and ratio of the components in solution as well as the effect of annealing via time-dependent and temperature-modulated experiments [46].
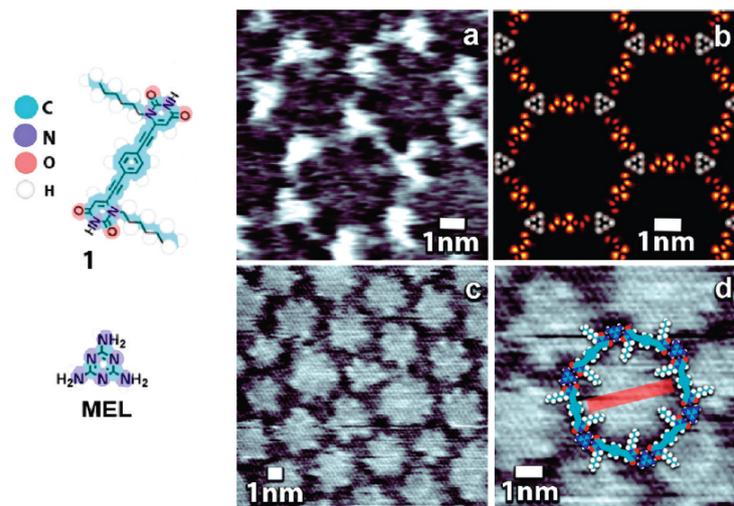
Fig. 4.3: STM images recorded at the solid-liquid interface of bicomponent nanoporous networks [46].

An interesting temperature-induced phase transition was observed on a linear molecular module of a 2D hydrogen bonded assembly by STM on Ag(111) surface. The phase transition proceeds from a hexagonal porous network (left part of figure 4.4) to a close-packed rhombic arrangement (right part of figure 4.4). The two terminal groups of the bis-2,6-di(acetylamino)pyridine module are known to be involved in hydrogen bonding interaction showing a donor-acceptor-donor (DAD) conformation (the meaning of DAD is indicated in figure 4.5). STM measurements performed at 77 K in ultrahigh vacuum (UHV) found that for samples prepared before the annealing process the molecules arrange in a hexagonal porous network. In the proposed model, each unit interacts via two weak hydrogen bonds with two neighboring modules, while after annealing the sample at 420 K, the hexagonal network transforms into a close-packed 2D rhombic pattern shown in the right part of figure 4.4. Matena *et al.* also found that the difference in intensity for the two acetyl units reveals a conformational difference between the two acetyl groups (indicated with two white arrows in the right part of figure 4.4 - panel (a)).

Before annealing   After annealing at 420 K
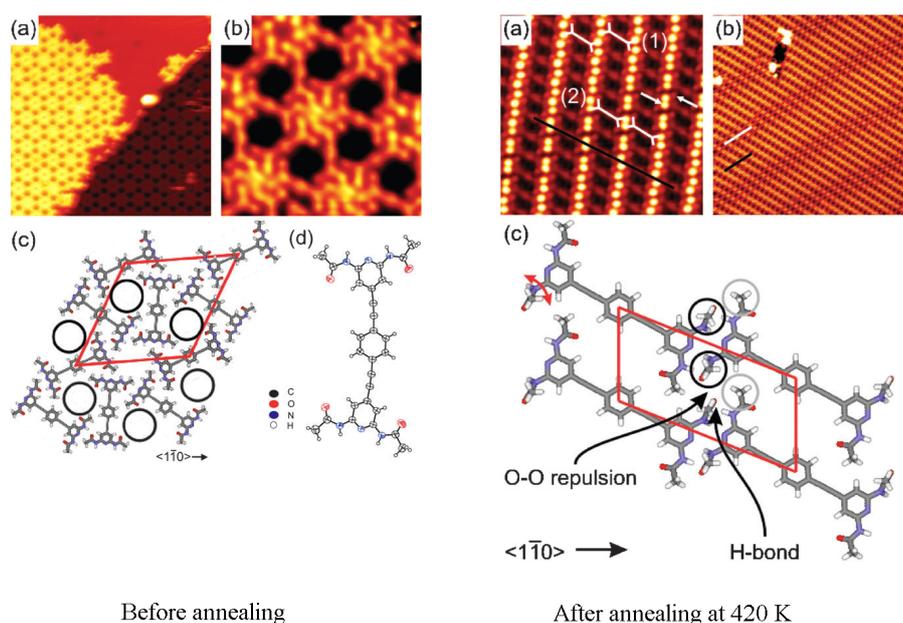
Fig. 4.4: STM images and the proposed model of the bis-2,6-di(acetylamino)pyridine module before and after annealing at 420 K (left part: a: scan range 34 x 34 nm^2, b: 7 x 7 nm^2; right part: a: 10 x 10 nm^2, b: 39 x 39 nm^2; adapted from ref. [63]).

Such an intermolecular interaction is equivalent to a *trans-cis* conformation change leading to a (DADA)x2 dimer structure (as in figure 4.5). The *cis* conformation adopted by two of the four amidic bonds strongly promotes quadruple hydrogen bonding interactions favoring an unidirectional anisotropy. The amide unit in the *cis* conformation displays some flexibility due to a balance between attractive (hydrogen bonds) and repulsive (steric demands) interactions. In this situation the formation of the hexagonal network is kinetically controlled while the rhombic assembly represents the thermodynamically stable phase and the control over the conformational state of adsorbed molecules play an important role in the design of writeable organic-based nanostructures.
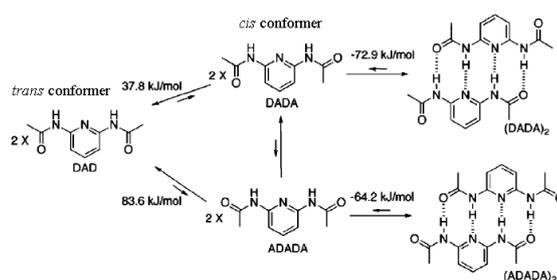
Fig. 4.5: Influence of the *cis* and *trans* conformers on the dimerisation processes [63].

4.3   Study of solids with homomolecular association

The materials I investigated were members of an extended molecular library with molecular units containing hydrogen bond-forming functional groups, which makes possible the self-recognition and self-organization of them in a predictable manner [27]. In particular, molecular modules featuring 2,6-di(acetylamino)pyridine moieties able to selectively recognise uracil-bearing modules were engineered. The components of the molecular library are presented in figure 4.6.
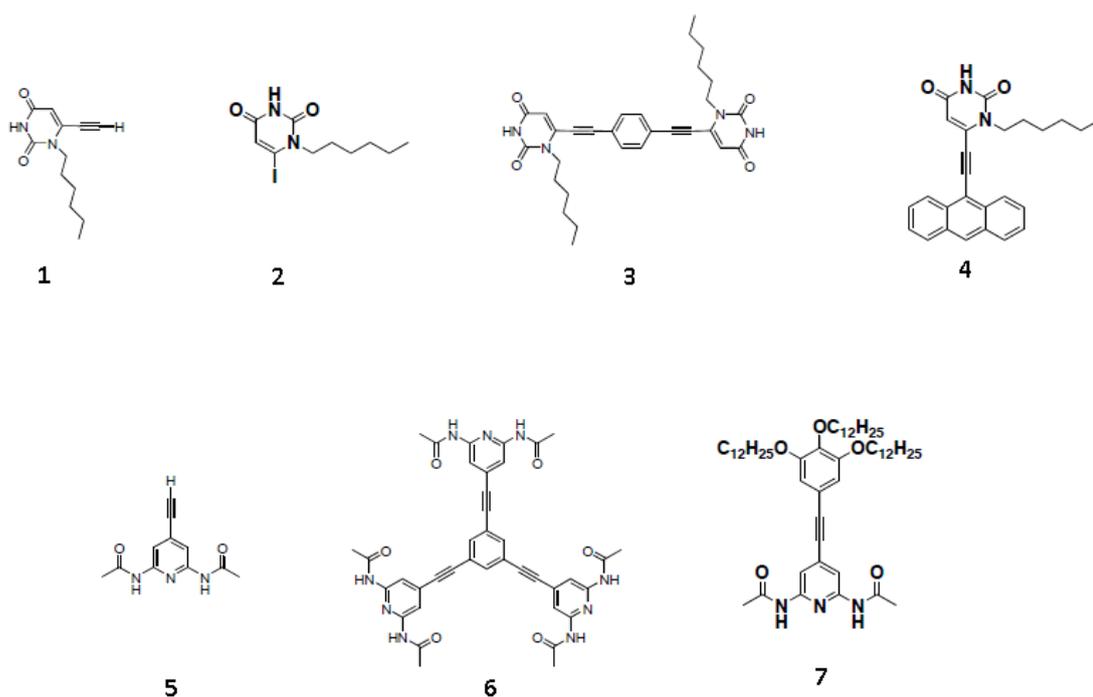
Fig. 4.6: Molecular library

Figure 4.7 shows the homomolecular self-organization of two uracil based modules (**a**) and di(acetylamino)-pyridine based modules (**c**) while the heteromolecular recognition is mediated via triple hydrogen bonds established between the NH-N-NH (DAD) terminations of the 2,6-di(acetylamino)pyridine and the CO-NH-CO (ADA) imidic groups of the uracil based modules (**b**) [27]. These molecules come from a collaboration with Prof. Davide Bonifazi's laboratory at the University of Trieste, Italy.
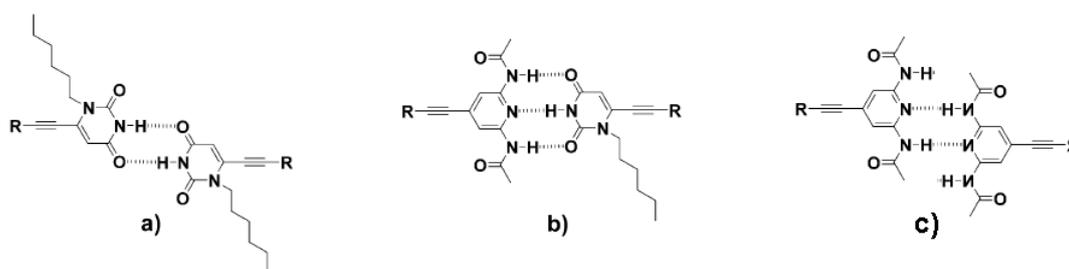
Fig. 4.7: (a) One possible molecular conformer for homo-association geometry between two uracil based modules, (b) heteromolecular self association geometry between di(acetylamino)-pyridine and an uracil based unit, (c) hydrogen bonded conformer for homomolecular geometry of di(acetylamino)-pyridine based module in the *trans* isomer.

4.3.1 Infrared spectral library

The first part of my work consists of preparing an infrared spectral library of the molecules presented in figure 4.6. These molecules have different functional sites which permit the self-assembly through hydrogen bonding (figure 4.7). Starting from the basic molecular units and finishing with the final supramolecular assemblies, I studied the supramolecular ordering of different imide-uracil and acetylaminopiridyne based molecular constituents by temperature dependent infrared absorption spectroscopy combined with other special techniques (matrix isolation and theory). In this section I will present basic properties of the prototypical molecules (figure 4.6). During my presentation of the infrared spectra of the molecules I will focus my attention every time to the spectral ranges where the vibrational bands are influenced by the formation or disruption of the hydrogen bonds (typically the C=O and N-H bending and stretching regions).

Molecule 4

4 contains only one uracil moiety, terminated with an anthracyl unit. Figure 4.8 presents an STM image recorded on Ag(111) surface under UHV conditions. Different molecules were used to obtain linear assemblies by association of monomeric units through triple hydrogen bonds. Molecule **4** was successfully used as a stopper for the linear chain formed from two linear (DAD) and (ADA) molecules (figure 4.8 (b) and (c)) [25]. The temperature-dependent infrared spectra are presented in figure 4.9. For the homomolecular organization a stabilization with double hydrogen bonds is expected (figure 4.7 - **a**). This implies that

one carbonyl group is free while the amine group is always involved in hydrogen bond formation.
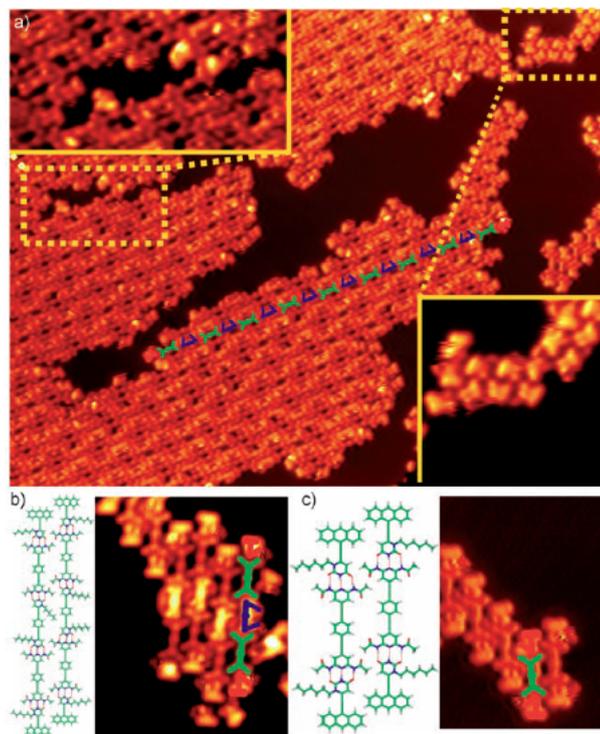
Fig. 4.8: STM images of multicomponent submonolayers on Ag (111) surfaces. Two linear molecules with hydrogen bond forming sites at the opposite end of the molecules form supramolecular wires. Molecule **4** terminates the supramolecular linear chain acting as a molecular stopper. The scan range for panel (a) is 50 x 40 nm^2 (STM results measured by M. Matena, T. Jung, and M. Stöhr from University of Basel, Switzerland) [25].

In figure 4.9 the free C=O vibration is assigned to the band at 1706 cm^{-1} and its position is not changing during temperature raising. The hydrogen bonded C=O and N-H show a strong temperature dependence (at 1680- and at 3165 cm^{-1} respectively). At 523 K the melting of the hydrogen bonds occurs, demonstrated by the appearance of a new band at 3410 cm^{-1} assigned to the free N-H vibration.

Molecules 5, 6, and 7

Molecule **5** is the building unit for **6** and **7** (figures 4.6). I will present first a comparative spectrum of the three molecular modules taken at room temperature followed by the study of temperature dependence. In figure 4.6 module **5** is presented as the *trans* isomer, in this situation it is supposed that hydrogen bonds are formed between N-H$\cdots$N (like in figure 4.7
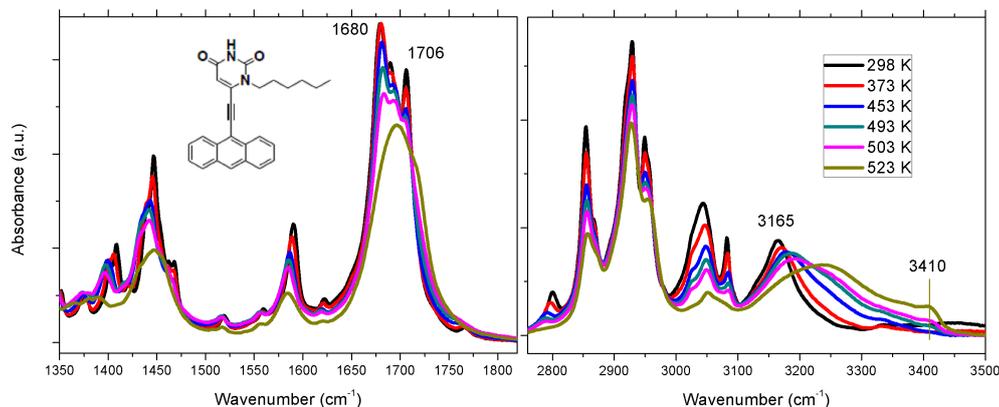
Fig. 4.9: Temperature dependence of the infrared spectra of **4** recorded in KBr pellet from room temperature up to 523 K.

(c)). From figure 4.10 it is evident that even if the hydrogen bond forming sites are identical for each module, there are differences in the C=O and N-H stretching regions. Other factors like the geometry of the molecular modules or other steric interactions can affect the supramolecular ordering even in the solid state. This observation is in agreement with data published in the literature [1, 63, 67]. STM studies in UHV and at solid-liquid interface also revealed that the self-association of di(acetylamino)pyridine containing derivatives is limited by conformation constrains of the amidic functional groups and a favorable geometric disposition of the hydrogen bond forming sites for a frontal self-association is disfavored [65]. However, by studying molecular modules **5**, **6**, and **7** in the solid state, clear evidence can be found for self-association in accordance with previously published data [67, 68]. In the C=O stretching region (1650-1800 cm^{-1}) there are two distinct bands for module **5** (at 1668 and 1713 cm^{-1} marked with the two black vertical lines in figure 4.10) while modules **6** and **7** contain one broader band at approx. 1680 cm^{-1}. The displacement between the two C=O bands for **5** (45 cm^{-1}) suggests that one carbonyl group is hydrogen bonded. This is possible only if a *trans-cis* conformation change takes place. The origin of the broader carbonyl band for **6** and **7** is not evident from the room temperature spectra (if it is free or hydrogen bonded). In the N-H stretching vibration region module **5** shows two distinct and intense bands at 3252 and at 3318 cm^{-1}. These spectral features are different for **6** and **7**. There is a broad featureless band in the range 3200-3350 cm^{-1}, but also an extra band at 3433 cm^{-1} for **6** and at 3466 cm^{-1} for **7**. These two extra bands are typically

assigned to free vibrations (N-H or O-H). The absence of any bands for **5** above 3400 cm^{-1} indicate that both amine groups are involved in hydrogen bonds. Further evidence about the exact conformation structure in the solid state is obtained from temperature dependence.
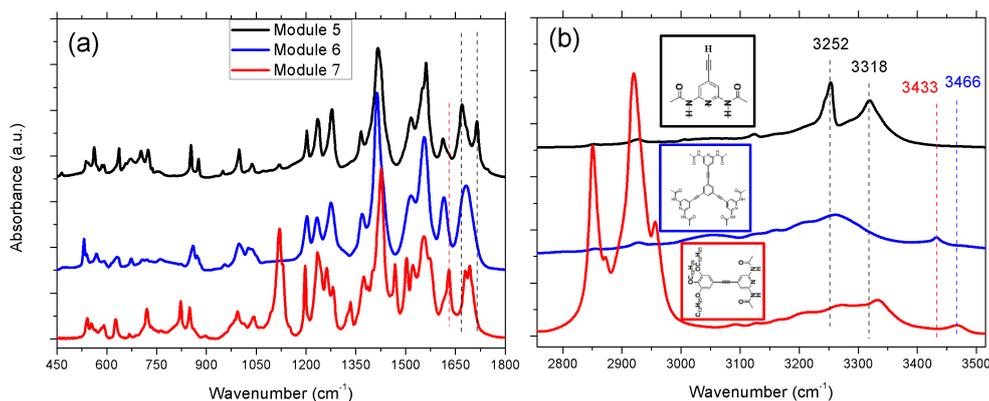
Fig. 4.10: Room temperature infrared spectra of modules **5**, **6** and **7**.

Figure 4.11 presents the effect of temperature on the hydrogen bond forming terminations of **5**. The region between 1475-1575 cm^{-1} corresponds to the N-H bending vibrations, the band at approx. 1600 cm^{-1} is the aromatic C=C and C=N vibration. In the following I focus on the C=O and N-H stretching bands to see their free or hydrogen bonded state in order to extract information about the exact conformational geometry. The band centered at 1668 cm^{-1} shows a slight frequency shift to higher wavenumbers and a strong intensity decrease as the temperature is raised (typical of hydrogen bonded C=O). The other carbonyl band (at 1713 cm^{-1}) seems to be unchanged up to 473 K. Above 483 K they merge into one single broad band. Both N-H stretching bands at 3252- and at 3318 cm^{-1} behave similarly to the hydrogen bonded C=O band (slight frequency shift and strong decrease in intensity), which sustains the observation that both N-H sites are involved in hydrogen bond formation. The spectral shift of the hydrogen bonds affected bands is presented in figure 4.11 as vertical black and magenta lines and the value is typically between 5-10 cm^{-1}. These spectral changes at elevated temperatures indicate the presence of a (DADA)x2 dimer structure which is due to *trans-cis* conformation change due to steric demands (as presented in figures 4.4 and 4.5).
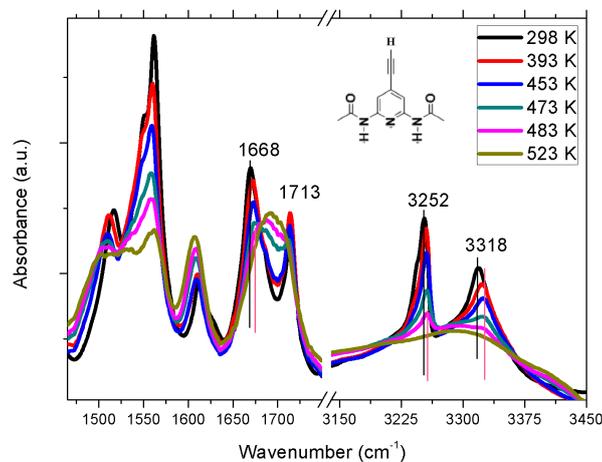
Fig. 4.11: Temperature dependence of the infrared spectra of **5** recorded in KBr pellet from room temperature up to 523 K.

The temperature dependence of the infrared spectra of molecule **6** is presented in figure 4.12. This molecular module could not be investigated by STM as it cannot be sublimed (the sample preparation for STM measurements under UHV conditions includes the sample evaporation to the sample holder). In the case of temperature dependent infrared measurements I have observed that the melting of the hydrogen bonds is related to the sublimation temperature of the constituents. Above the sublimation temperature, the hydrogen bonds are disrupted, illustrating that the sublimation temperature provides a good estimate for hydrogen bond stability in such systems. Knowing that module **6** does not sublime, it was interesting to study the melting of the hydrogen bond is this situation. Though for the previously discussed molecular modules the hydrogen-bond disruption occurred below approx. 550 K, for module **6** the presence of the hydrogen bonded bands is evident even at much higher temperatures. The total melting of the hydrogen bonds seems to occur above 673 K.

The temperature dependent spectra of molecule **7** are presented in figure 4.13. At room temperature two C=O stretching bands at 1680 and 1692 cm^{-1} and two bands above 3000 cm^{-1} (at 3333 and 3466 cm^{-1}) are present. The band at 1680 cm^{-1} does not change with temperature, so this band can be assigned to one free C=O stretching vibration (similarly as for unit **6**). The band at 1692 cm^{-1} disappears at 318 K and two new bands emerge at 1669 and 1715 cm^{-1}. In the N-H stretching vibration region the bands at 3333 and
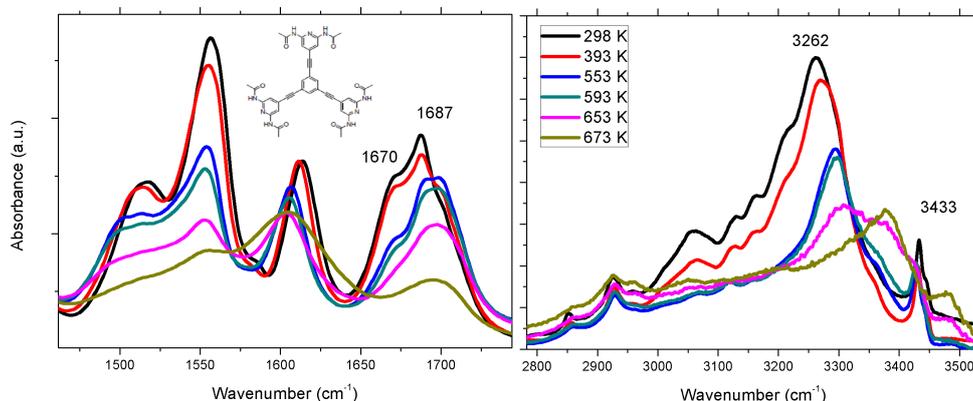
Fig. 4.12: Temperature dependence of the infrared spectra of **6** recorded in KBr pellet from room temperature up to 673 K.

3466 cm^{-1} disappear above 318 K with new bands appearing at 3275 and 3405 cm^{-1}. Such changes open the question of possible tautomerization processes (the H atom forming an N-H bond transfers to O atom of C=O bond forming a C-O-H bond). NMR studies on the tautomerism of 2-acylaminopyridines revealed that the amide tautomer and trans isomer is the most stable conformation [69] (as presented in figure 4.6). The changes observed in the infrared spectra of **7** are assigned to temperature induced phase transitions. At room temperature the two C=O bands (at 1680 and 1692 cm^{-1}) are assigned to free vibrations in accordance with data published in the literature [67]. At this temperature it is not evident if self-association is occurring. From its temperature dependence, the new C=O band at 1669 cm^{-1} appeared above 318 K is assigned to hydrogen bonded C=O. A carbonyl band can be involved in hydrogen bond formation if *trans-cis* isomerism occurs (as for module **5**) or if a phase transition is favored (as the hexagonal porous structure presented in figure 4.4 [63]). On the other hand a *cis* conformation would favor a (DADA)x2 dimeric structure (as for unit **5**) which would imply that both N-H and one C=O are taking part in hydrogen bond formation. The presence of the free N-H vibration at 3405 cm^{-1} suggest that a self-association geometry other than frontal disposition is favored.

43
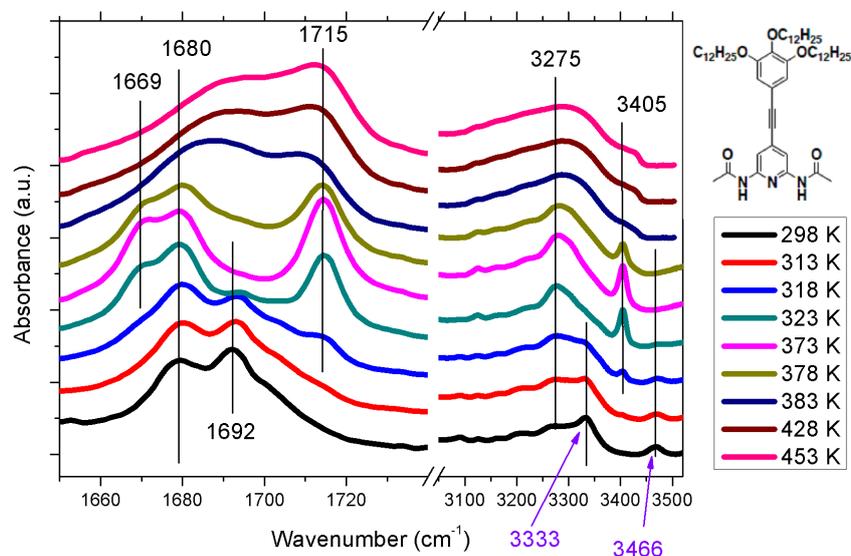
Fig. 4.13: Temperature dependence of the infrared spectra of **7** recorded in KBr pellet from room temperature up to 453 K.

Molecules 1, 2, and 3

In figure 4.14 molecules **1**, **2**, and **3** contain the same hydrogen bond forming functional groups, while molecule **1** is the starting unit for molecule **3**. Molecules **1** and **2** are similar except the functional group on atom 6.
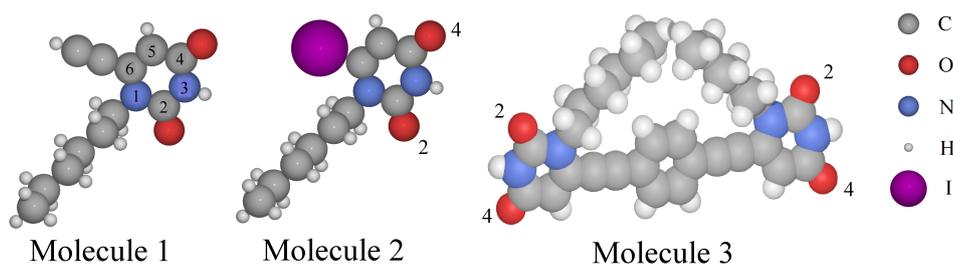
Fig. 4.14: 1-hexyl-6-ethynyluracil (molecule **1**, left), 1-hexyl-6-iodouracil (molecule **2**, middle) and bis-uracil molecular unit (molecule **3**, right) have identical functional groups forming hydrogen bonds (the carbonyl and amine groups). The molecules are shown in the diketo form. The two carbonyl groups including carbon atoms 2 and 4, respectively, may participate in different hydrogen bonding motifs (numbering of the atoms in the uracil ring is presented for molecule **1**).

Figure 4.15 presents the room temperature spectra of **1**, **2**, and **3**. Focusing on the spectral regions where the effects of hydrogen bonds are important I present just the
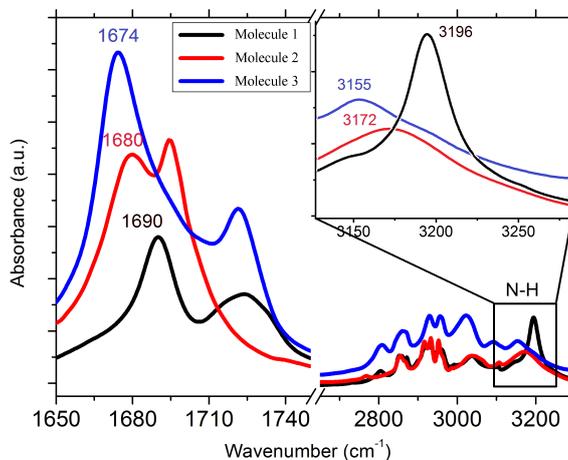
Fig. 4.15: Room temperature infrared spectra of modules **1**, **2**, and **3**.

C=O stretching region (1650-1800 cm^{-1}) and the N-H stretching region (approx. 3100-3300 cm^{-1}). Even though the hydrogen bond forming groups are identical, the vibrational behavior of the three molecular modules is different, visualized by the different frequency and intensity of the free and hydrogen bonded C=O and N-H bands. These three molecular modules are the subject of the next two subchapters and as we will see the different functional groups on atom 6 (as in figure 4.14) do not have a significant effect on the relative energy hierarchy between the different dimer conformations, but they affect the dynamics of the hydrogen bonds at elevated temperatures.

4.3.2 Base uracil molecular units

In this study, I investigate the stability and dissociation dynamics of hydrogen bonds by studying a pair of uracil-derivative molecular modules. Uracil-based molecular building blocks have already shown their potential as basic components in supramolecular chemistry [1, 25, 26, 46, 64, 70, 71], which means that their stability and breakdown mechanisms are of technological importance. In this context, infrared spectroscopy is very effective in the study of such hydrogen bonded complexes [18, 72]. Special methods like matrix isolation spectroscopy combined with a more conventional infrared spectroscopic method provide unique characterization opportunities as they permit the study of the molecular units both in their aggregated and free state. MI spectroscopy in particular is a powerful method to measure an almost perturbation-free spectrum of isolated molecules [73]. Choosing appro-
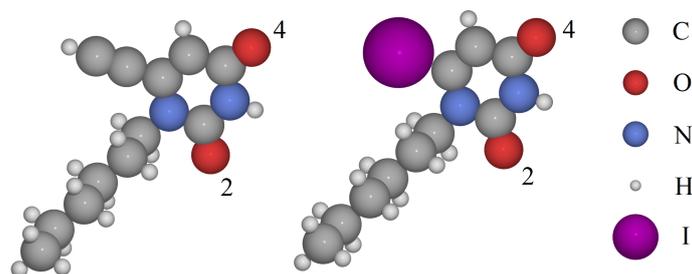
Fig. 4.16: 1-hexyl-6-ethynyluracil -unit **1** (left) and 1-hexyl-6-iodouracil - **2** (right) have identical functional groups forming hydrogen bonds (the carbonyl and amine groups). The molecules are shown in the diketo form. The two carbonyl groups which may participate in different hydrogen bonding motifs are indicated by carbon atoms 2 and 4, respectively.

priate conditions, these spectra can be free from signs of aggregated species even in the case of strong intermolecular interactions [74, 75].

Two uracil-type molecules (molecule **1** and **2** in figure 4.6, the same molecules in figure 4.16) were chosen for investigation: 1-hexyl-6-ethynyluracil (molecule **1**) and 1-hexyl-6-iodouracil (**2**). The two molecules contain identical hydrogen bond-forming functional groups, but differ in the functional group attached to atom 6 of the central aromatic ring (see figure 4.16). MI characterization was performed on isolated molecules and compared to spectra in the solid state, where aggregation is present [76, 77]. The optimum sublimation temperature was 353±5 K for **1** and 393±5 K for **2**. On the other hand, when heating the solids, a sudden drop in intensity of certain spectral lines is observed with temperature which can be attributed to the melting or disruption of hydrogen bonds. The combination of infrared studies with temperature dependent ab initio molecular dynamics simulations allows the unambiguous but non-trivial assignment of the temperature dependent spectral peaks.

Ab initio molecular dynamics (AIMD) calculations were performed for all three dimer structures of **1** and **2** at different temperatures to obtain vibrational spectra. For the lowest energy dimer structure, additional simulations at 5 K, 383 K, and 453 K were used to calculate the temperature dependence of its spectrum. Figure 4.17 presents the three dimer conformations considered in the calculation. The N-H (3) and one C=O (2 or 4) group are always involved in hydrogen bond formation while the other C=O group is free. The notation of Biemann, Häber and Kleinermanns [78] was used for the carbonyl groups as

well as the dimers: in the latter case, the labels of the carbon atoms of the carbonyl groups taking part in the hydrogen bond were indicated. The situation in these two compounds is simplified compared to that of uracil [76, 77], because the N_1 atom is blocked by the side chains and cannot take part in hydrogen bonds.
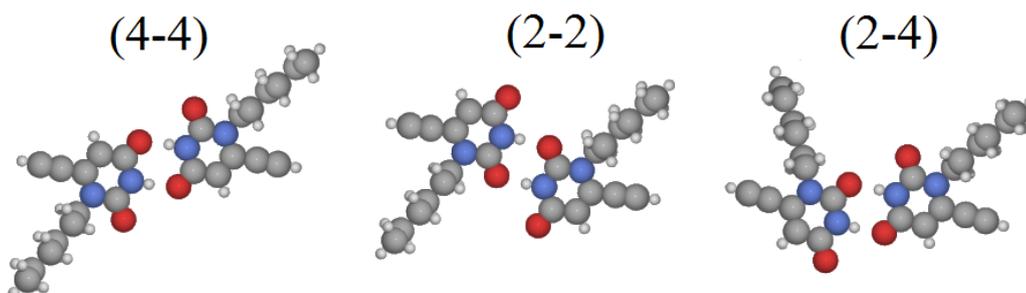
Fig. 4.17: The three investigated dimer configurations of molecule **1** in the AIMD study (the same structures were considered also for molecule **2**).

The characterization of vibrational peaks in the calculated dipole spectra was done by identifying a set of representative bond coordinates, e.g. bond distances or bond angles, and extracting their time dependence $A(t)$ from the AIMD trajectories using the Atomic Simulation Environment [79]. The character of a given mode in terms of various bond coordinates is given by the relative spectral strengths of the vibrational peak in the Fourier transforms $A(\omega)$ of these coordinates, as demonstrated in figure 4.18 which also shows the corresponding harmonic spectrum. For the 5 K MD simulations, the molecules only sample the harmonic region of the potential energy surface. This is reflected in the good correspondence between the harmonic and molecular dynamics vibration spectra, which agree to within 10 cm^{-1} (theoretical calculations done by Felix Hanke and Jonas Bjork).

Moreover, this approach toward identifying vibrational modes can also be used for a given vibrational mode to identify the coupling between the collective coordinates, e.g. between the N-H bend and the two C=O stretches at 1460 cm^{-1} for molecule **1** where the spectrum of all three bond coordinates has peaks in figure 4.18. This is also reflected in the normal mode analysis, where the N-H bend also has a small component of the C=O stretch modes and vice versa [2].
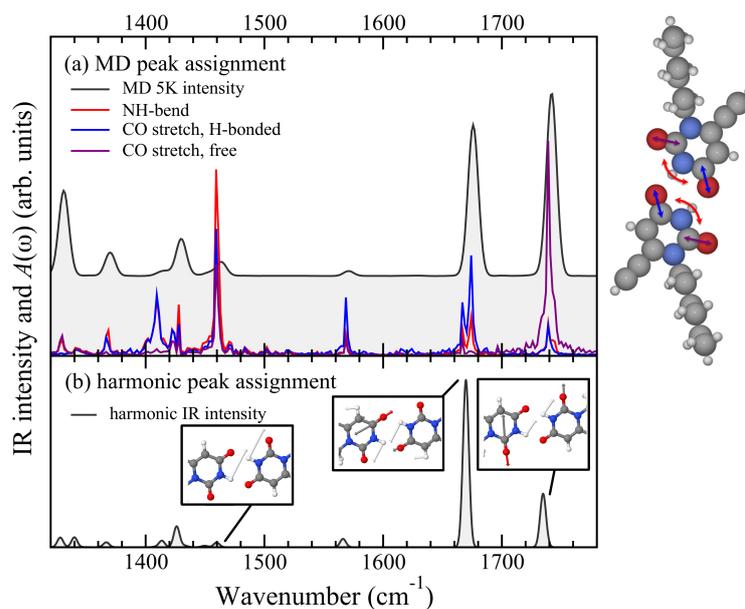
Fig. 4.18: (a) Illustration of the procedure used to assign the peaks in molecular dynamics spectra: each colored line shows the Fourier transform of a given collective coordinate of the (4-4) dimer simulated at 5 K, see molecular model on the right. The shaded area shows the full infrared intensity computed from the MD simulation, and offset by a constant for comparison. (b) The corresponding infrared intensity calculated within the harmonic approximation. The peaks assigned to eigenmodes with most prominent CO-stretch and/or NH-bend are indicated, with the atomic motions illustrated with arrows in the molecular models for each of these three modes (work done by Felix Hanke and Jonas Bjork).

Matrix isolation results

Figures 4.19 and 4.21 present the experimental infrared spectra of **1** and **2**, respectively, in the solid state (black curve - recorded at 298 K) and matrix isolation infrared spectra of isolated monomers (red curve - recorded in argon matrix at 8 K). Mode assignment of the MI spectra was done by comparing these to the theoretical spectra calculated for monomers at 5 K, while the assignments of solid state spectra were obtained by comparison with the theoretical spectra calculated for different dimer configurations. In the solid phase at 298 K the sample state can be considered a static assembly of dimers with hydrogen bonds being the main intermolecular interaction [76, 77] which affects the corresponding infrared bands. Lowering the temperature causes line narrowing in the solid state, but does not affect the frequencies considerably. Therefore, a direct comparison between the solid state and MI spectra is possible even if the temperature is different.
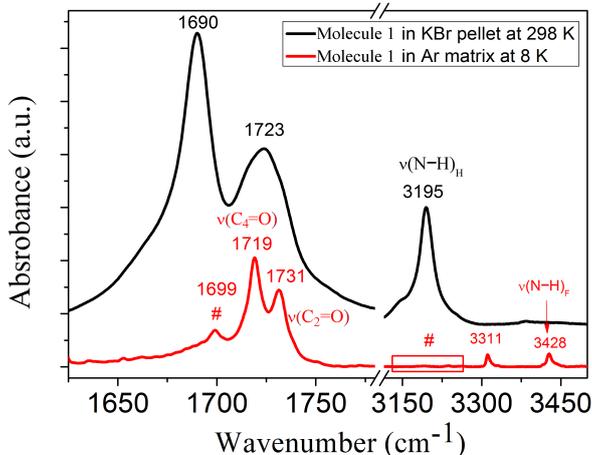
Fig. 4.19: Direct observation of the effect of hydrogen bonds on molecule **1**: comparison between the solid state spectrum (at room temperature - black) and monomers (in Ar matrix - red). Peaks marked with # are from the very low amount of dimers formed during Ar matrix formation. All the spectra were baseline corrected and shifted vertically for clarity. Subscripts 2 and 4 refer to the corresponding carbonyl groups according to figure 4.16, while subscripts F and H denote the free and hydrogen bonded nature of the vibrations, respectively.

Tab. 4.1: Mode assignments for the peaks in the MI spectrum of isolated molecule **1**. Experimental values were derived from the spectrum recorded at 8 K while theoretical values were calculated by MD simulation at 5 K.

$\tilde{\nu}_{EXP}$ (cm^{-1})	$\tilde{\nu}_{AIMD}$ (cm^{-1})	Assignment
3428	3587	ν(N-H)
3311	3478	ν(C-H)
1731	1742	ν(C$_2$=O)
1719	1718	ν(C$_4$=O)

In the experimental MI spectrum of **1** the bands at 1719 and at 1731 cm^{-1} belong to the free C$_4$=O and C$_2$=O vibrations of the monomer, respectively. The comparison of experimental and theoretical band assignments is presented in table 4.1.

One of the bands in the matrix isolation spectrum of **1** in figure 4.19 (marked with #, at 1699 cm^{-1}) merits a more detailed analysis. We have considered two possibilities for the assignment of this band; either the presence of another tautomer or a small number of dimers. Although the temperature dependence in the solid phase (detailed in the next subsection) did not reveal the presence of other tautomers either for **1** or for **2**, tautomerization can occur during sublimation or in the gas phase [80]. Calculations show that the total energies of the enol tautomers relative to that of the diketo tautomer are high (above

Diketo form

$\Delta G^{\circ}_{0\,K} = 0$ kcal mol^{-1}

Enol 1

$\Delta G^{\circ}_{0\,K} = 10.7$ kcal mol^{-1}

Enol 2

$\Delta G^{\circ}_{0\,K} = 17.2$ kcal mol^{-1}

Enol 3

$\Delta G^{\circ}_{0\,K} = 19.1$ kcal mol^{-1}
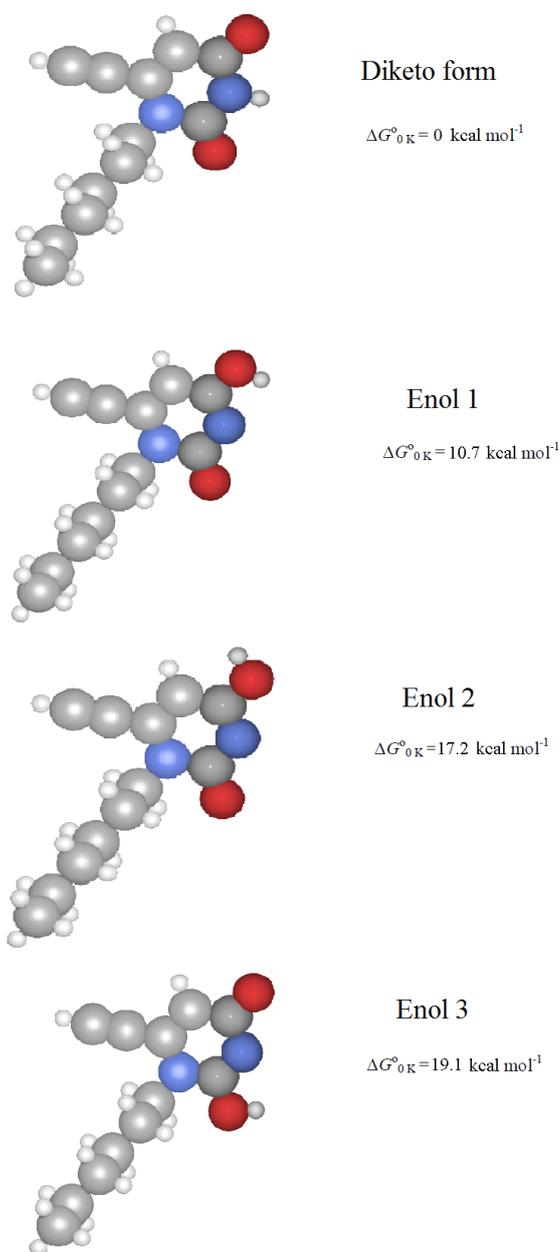
Fig. 4.20: Relative energies of **1** tautomers with respect to the diketo form of the molecule. The energies refer to structurally optimized tautomers (work done by Felix Hanke and Jonas Bjork).

10 kcal mol^{-1}, figure 4.20), which is in agreement with previous experimental and theoretical results for other uracil derivatives [80–86]. These studies show that the diketo form of uracil is the most stable and predominant tautomer in the gas phase, in solution and in the solid state, hence the presence of other tautomers in the matrix is excluded. The band

Tab. 4.2: Vibrational frequency and mode assignment of matrix isolation spectra of **1** and
2 monomers

Sample	$\nu(C_4{=}O)$ (cm^{-1})	$\nu(C_2{=}O)$ (cm^{-1})	$\nu(\text{N-H})$ (cm^{-1})
1H6EU	1719	1731	3428
1H6IU	1713	1732	3428

at 1699 cm^{-1} can be assigned to the C=O mode of the hydrogen bonded isolated dimers,
which are present in the matrix in a small amount.
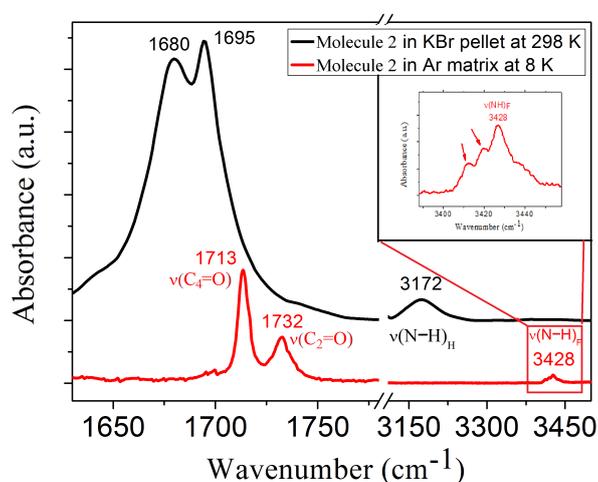
Fig. 4.21: Solid state spectrum at 298 K (black curve) and matrix isolation spectrum at
8 K (red curve) of **2**. Subscripts 2 and 4 refer to the corresponding carbonyl
groups according to 4.16 while subscripts F and H denote the free and hydrogen
bonded nature of the vibrations, respectively.

Figure 4.21 presents the solid state spectrum (black curve) and the matrix isolation
spectrum (red curve) of **2**. As for molecule **1**, the band assignment of the MI spectrum was
performed by comparing with the theoretical spectrum of the monomer of this molecular
module. We assign the band located at 1713 cm^{-1} to a $C_4{=}O$ stretch and the one at 1732
cm^{-1} to a $C_2{=}O$ stretch. Comparison of matrix isolation spectra of **1** and **2** is presented
in table 4.2. While the $C_2{=}O$ bands are at the same position in both cases, the $C_4{=}O$
bands show a 6 cm^{-1} difference between the two molecules which is caused by the different
masses of the ethynyl group and iodine atoms attached to C_6.

To obtain detailed information about the dimer structures of **1** and **2**, different dimer
structures were considered in the theoretical calculations for each of the molecular modules,
illustrated for **1** in figure 4.17. Table 4.3 presents the calculated binding energies for the

different configurations, which show that the (4-4) dimer structure is energetically most stable for both **1** and **2**. This structure is identical to that in crystalline uracil [76, 77]. Furthermore, the relative energy hierarchy between the different dimers remains the same for **1** and **2**. Thus the different functional groups on atom 6 (according to figure 4.16) do not have a significant effect on the hydrogen bonds. This result is also in agreement with results derived from chloroform solution spectra of 1-cyclohexyluracil by Biemann, Häber and Kleinermanns [78].

Tab. 4.3: Formation energies of the different isolated dimers for **1** and **2**, calculated as the difference between the energy of a structurally optimized dimer and two structurally optimized monomers.

dimer	Molecule **1** (kcal mol^{-1})	Molecule **2** (kcal mol^{-1})
(4-4)	-14.8	-15
(2-2)	-13.4	-13.4
(2-4)	-13.8	-14.1

In table 4.4 experimental and computed frequencies are shown for the (4-4) structure of **1**. Note that the experimental value for $\nu(C_2=O)$ for the dimers is equal to the corresponding mode in the isolated molecule, suggesting that it is not at all affected by the surrounding hydrogen bonds.

Temperature dependence

Temperature dependent infrared spectroscopic investigations using solid samples can be used for the characterization of the stability of hydrogen bonded systems as the behavior of bands shows how the hydrogen bonds become weaker or entirely disrupted at elevated temperature [1]: With increasing temperature, the hydrogen bond affected bands decrease in peak height and shift to higher wavenumbers. The electron on the hydrogen atom be-

Tab. 4.4: Mode assignments of isolated dimers in the experimental (8 K) and calculated (5 K) infrared spectrum of the most stable (4-4) dimer structure **1**. Subscripts 2 and 4 refer to the corresponding carbonyl groups according to figure 4.16 while subscripts F and H denote the free and hydrogen bonded nature of the vibrations, respectively.

$\tilde{\nu}_{EXP}$ (cm^{-1})	$\tilde{\nu}_{AIMD}$ (cm^{-1})	Assignment
1731	1742	$\nu(C_2=O)_F$
1699	1676	$\nu(C_4=O)_H$

comes more localized and more strongly bound, which decreases its polarizability and consequently the intensity of the band.

This study also shows that the coexistence of different dimer conformers at elevated temperatures needs to be taken into account in the analysis of the infrared spectra. Figure 4.22 presents the temperature dependent spectra of **1** from room temperature up to 453 K. Apparently the spectra contain two components: one hydrogen bonded C=O stretching band at 1690 cm^{-1} and one free C=O band centered at 1723 cm^{-1} (according to figure 4.17 just one C=O is hydrogen bonded in all dimer conformers). Above 353 K a strong decrease in the peak height can be observed for the hydrogen bonded band (C=O band at 1690 cm^{-1}) along with a slight shift to higher wavenumbers. Above 403 K the free and hydrogen bonded C=O merge into one single broad band. The inset of figure 4.22 shows the peak height of the 1690 cm^{-1} band as a function of temperature. From the inset it can be seen that the peak height starts to decrease from 353 K with a more pronounced decrease above 383 K.

The peak height at 1690 cm^{-1} decreases sharply at 353 K (inset in figure 4.22) indicating a close correlation between the melting temperature of hydrogen bonds in the solid and the sublimation temperature under MI conditions. As the disruption of the secondary bonds strongly affects the cohesion energy of the solid, it is not surprising that the melting of the hydrogen bonds occurs in the same temperature region as the sublimation in the matrix isolation experiment, i.e. the temperature where the isolated molecules enter the argon stream.

Figure 4.23 shows the temperature dependence of the solid state spectra of **2** in the C=O stretching region. At room temperature both free and hydrogen bonded C=O bands are at lower wavenumber than for molecule **1** (figure 4.22). There is another difference between the spectra of the two molecules: while the hydrogen bonded C=O band of **1** is more intense than the free one, the hydrogen bonded C=O band of **2** is less intense than the free one. As the temperature is increased, the hydrogen bond affected C=O bands shift to higher wavenumbers, while the free C=O vibration at 1695 cm^{-1} remains unchanged. The inset of figure 4.23 shows the intensity of the hydrogen bonded C=O stretch mode at 1680 cm^{-1} as a function of temperature. Similar behavior as for **1** can be observed for **2** in the solid state spectra in the temperature region around the sublimation temperature
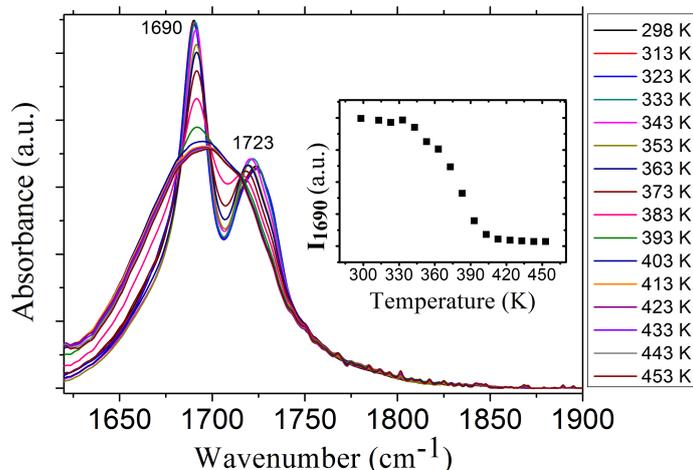
Fig. 4.22: Temperature dependence of the solid state spectrum of **1**. Inset: peak height at 1690 cm^{-1} as a function of temperature.

deduced from the MI experiment (393±5 K for **2**; inset of figure 4.23). Drastic changes occur just below 393 K indicating the correlation between sublimation and hydrogen bond melting temperature mentioned above.
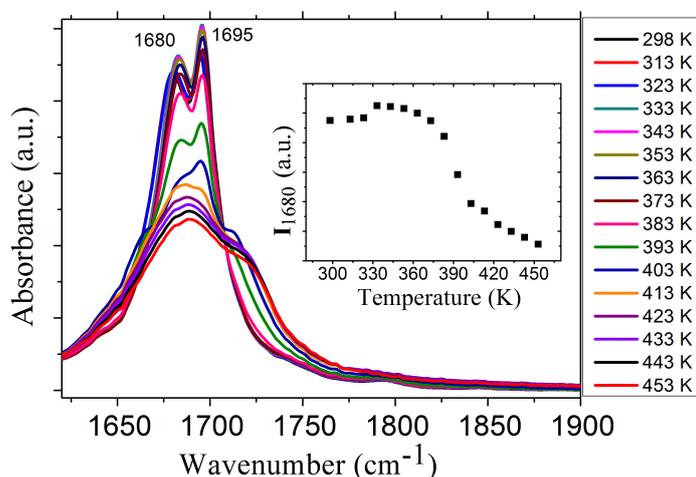
Fig. 4.23: Temperature dependence of the infrared spectrum in the C=O stretching region for solid **2**. Inset: peak height of 1680 cm^{-1} as a function of temperature.

Figure 4.24 presents the temperature dependence of the solid state spectrum for **2** between 383 K and 413 K. In the C=O region two new bands appear at 1664 and at 1713 cm^{-1}. Such a behavior is not characteristic for either **1** or the energetically most stable dimer (according to table 4.2). This is an indication that before the entire disruption of

hydrogen bonds a coexistence between different dimer conformers can occur in the solid state.
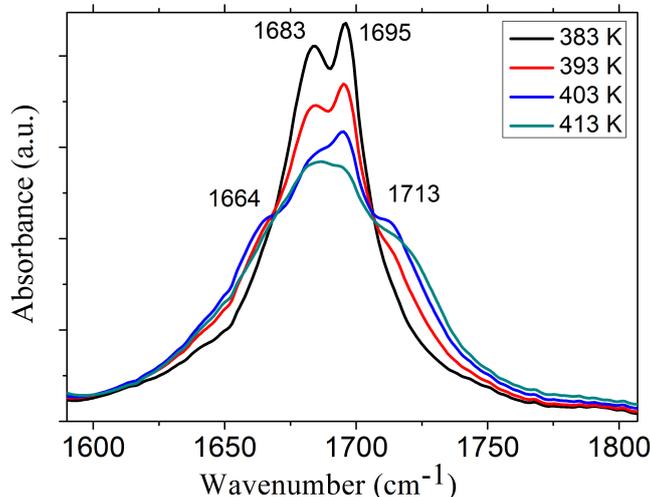
Fig. 4.24: Temperature dependence of the infrared spectrum of the C=O for solid **2** in the range 383 K - 413 K.

In figure 4.25 experimental results are compared to theoretical infrared spectra for **1**. Panel *A* represents the experimental results at 298, 383 and 453 K, while panel *B* shows AIMD results for the (4-4) dimer at the same temperatures. In the experimental results, important changes occur with increasing temperature in the peak height of the observed hydrogen bonded bands, but also in their frequency. After fitting the room temperature spectrum curve (with Lorentzian functions), a multi-component structure of both free and hydrogen bonded C=O stretching bands was revealed (figure 4.26). The hydrogen bonded C=O band consists of two components, at 1669 and 1689 cm^{-1}. Apparently the free C=O band contains three components at 1715, 1723 and 1732 cm^{-1}, respectively. Comparing the free C=O peaks to the matrix isolation results of the monomers it can be seen that the components at 1715 and 1732 cm^{-1} correspond to the free C_4=O and C_2=O vibrations (1719 and 1731 cm^{-1} for the matrix isolation results).

At an elevated temperature of 383 K the spectrum shows an important change in the multi-component structure (figure 4.27). Just four components are found at this temperature (1670, 1691, 1717 and 1731 cm^{-1}), the 1723 cm^{-1} component is completely missing. Such a change with temperature is an indication that the 1723 cm^{-1} band represents a hydrogen bonded component of a different dimer conformer according to figure 4.17 and table

4.3. This behavior is an indication that at given temperatures different dimer conformers coexist in the solid phase. Moreover, this conclusion is corroborated by the following results from AIMD calculations. To compare the different calculated AIMD infrared spectra (figure 4.25 *B*), the peak height was normalized to the free C=O band at 1733 cm^{-1} at room temperature. Similar behavior to the experimental results is observed, above 383 K the free and hydrogen bonded C=O bands merge into one broader band.
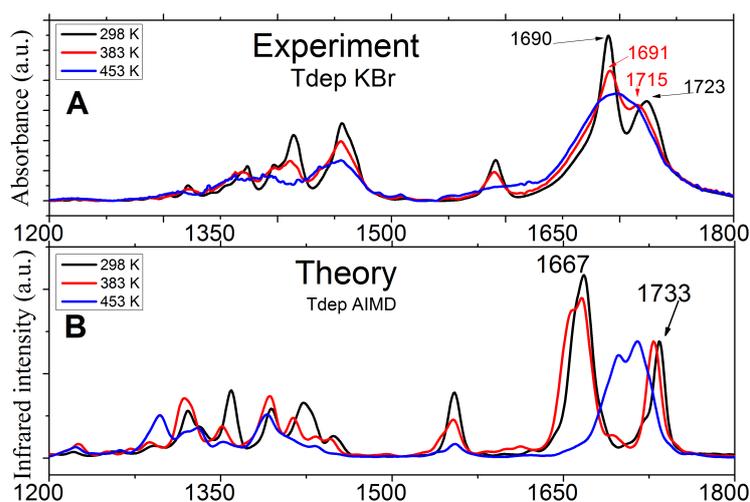
Fig. 4.25: Temperature dependence: A: Measured infrared spectra of solid **1** at 298 K, 383 K and at 453 K. B: AIMD-computed spectra of the (4-4) dimer (theoretical calculations done by Felix Hanke and Jonas Bjork).

As in the experimental results, a multi-component structure of the C=O band is present in the simulated spectra, given in figure 4.28. The analysis of the simulated spectra shows that the number of peaks stems from different symmetric and antisymmetric vibrations arising from the coupling between the two hydrogen bonds present in each dimer. For the symmetric (2-2) and (4-4) dimers, one observes two components for the C=O stretch, corresponding to the antisymmetric vibrations of both the free and hydrogen bonded sets of C=O groups. The symmetric vibrations do not yield a significant change in the dipole moment and therefore are not visible in the infrared spectra. The same argument shows that the asymmetric (2-4) dimer should have four separate components, which all happen to fall into the same broad peak seen in figure 4.28. Interestingly, the strongest red shift of the asymmetric hydrogen bonded C=O stretch in dimer (4-4) also demonstrates that this dimer is the most favorable conformer at room temperature. However, the number of peaks for
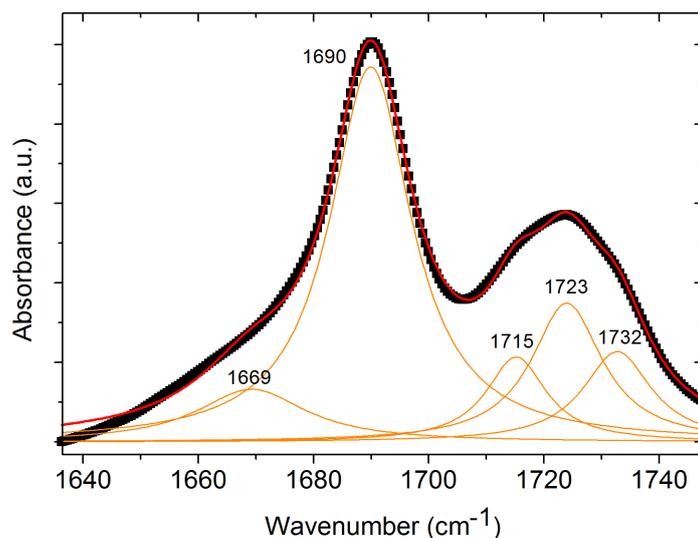
Fig. 4.26: Multi-component structure of both free and hydrogen bonded C=O of molecule **1** at room temperature. The reason is the coexistence of different dimer structures.
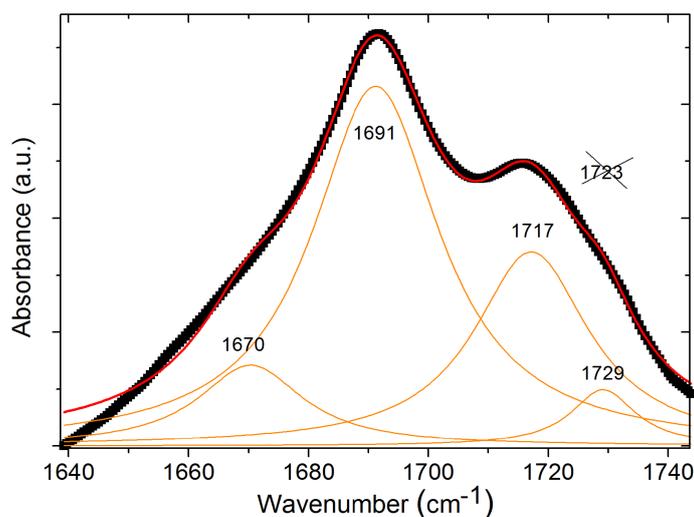
Fig. 4.27: Multi-component structure of both free and hydrogen bonded C=O of **1** at 383 K. The 1723 cm^{-1} band is missing which is an indication of coexistence of the (4-4) and (2-4) dimers.

each dimer (either two or four) does not correspond to the experimental observation. The explanation for the apparent disagreement between the number of peaks found in theoretical vibrational spectra for separate dimers on one hand, and the experimental observation on the other, is based on the coexistence of different dimer conformers at room temperature.

With increasing temperature the relative occupancy of different dimer structures is also changing and is much more pronounced in the experimental results.
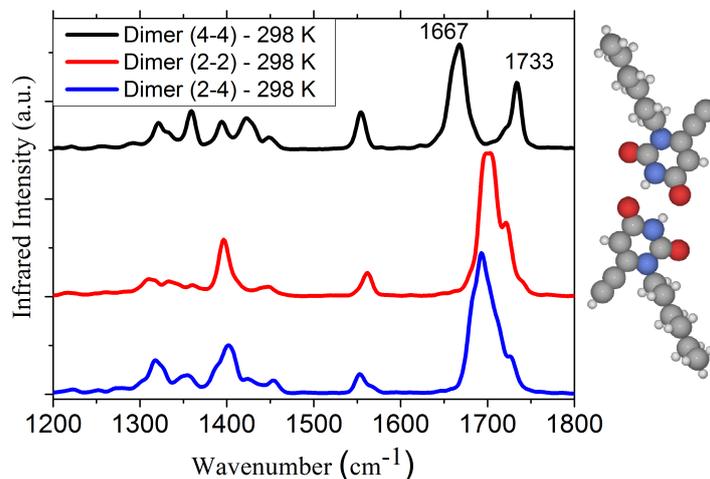
Fig. 4.28: Comparison between simulated infrared spectra of the (4-4), (2-2) and (2-4) dimer of **1** at 298 K. The molecular model on the right represents the most stable (4-4) dimer of **1**. The molecular model of the (2-2) and (2-4) dimer is presented in 4.17 (work done by Felix Hanke and Jonas Bjork).

Figure 4.29 shows the calculated spectra of the three iodized dimers of **2** at room temperature. The calculated spectrum of the most stable (4-4) structure (black curve) contains four separate components for the C=O stretches, corresponding to two symmetric and two antisymmetric stretches of the four separate C=O bonds. The experimental spectrum in figure 4.23 on the other hand shows very broad features that cannot be described in terms of the well-separated spectrum of any of the calculated dimers. Therefore, the comparison of experimental spectra of **2** (figure 4.23 and 4.24) with the corresponding calculated spectra of the (4-4) and (2-4) structure (figure 4.29) suggests that several different dimer structures are seen in the experiment. A thermal equilibrium of different bonding motifs should also be expected from the small difference in binding energies.

It is interesting to compare these results with more quantitative AIMD simulations on the O···H distances at different temperatures for the different dimer configurations of **1**. The results are shown in figure 4.30. Panel *A* presents the temperature dependence of the (4-4) dimer. At 5 K, the bond lengths are essentially fixed to their minimum energy value of the O···H distance (1.74 Å). At room temperature the fluctuations of the hydrogen
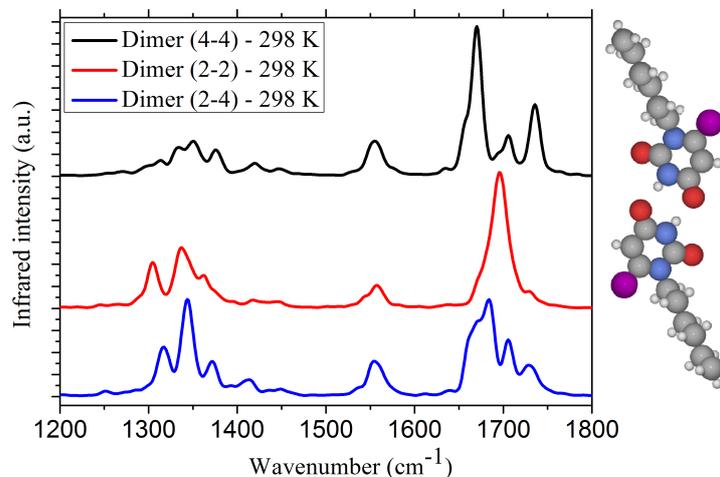
Fig. 4.29: Comparison of the C=O stretching region in the simulated infrared spectra of the (4-4), (2-2) and (2-4) dimer of **2** at 298 K. The molecular model on the right represents the most stable (4-4) dimer of **2** (work done by Felix Hanke and Jonas Bjork).

bond lengths are significantly larger and the highest probability occurs at 1.8 Å. At 383 K the dimer structure remains stable with a similar bond length distribution as at room temperature, while at 453 K hydrogen bond disruption occurs. This is evidenced by a broad and uniform bond length distribution which extends to "bond lengths" well beyond 3 Å. Following the temperature development of the bond lengths for the (2-4) and (2-2) dimers (panels B and C), the double peak structure shows that partial disruption can occur already at room temperature for the (2-4) dimer, while the disruption is nearly complete for the (2-2) dimer. The computed difference in thermal stability between different dimer conformers is consistent with the binding energy hierarchy, presented in table 4.3. Dimer (4-4) has the largest binding energy and is also the dimer that stays intact at highest temperatures. For example, at 383 K dimer (4-4) is intact, although the hydrogen bonds for dimer (2-2) and (2-4) are completely disrupted.

These results support the hypothesis on the coexistence of different dimer conformers at room temperature obtained from the behavior of the experimental spectra. The 1723 cm^{-1} band was assigned to a hydrogen bonded component of a different dimer conformer (figure 4.26) and represents the (2-4) dimer which is still stable at room temperature (figure 4.30, panel B). The absence of the 1723 cm^{-1} band at 383 K (figure 4.27) is also in agreement with the theoretical results that the (2-4) dimer is no longer stable at 383 K.
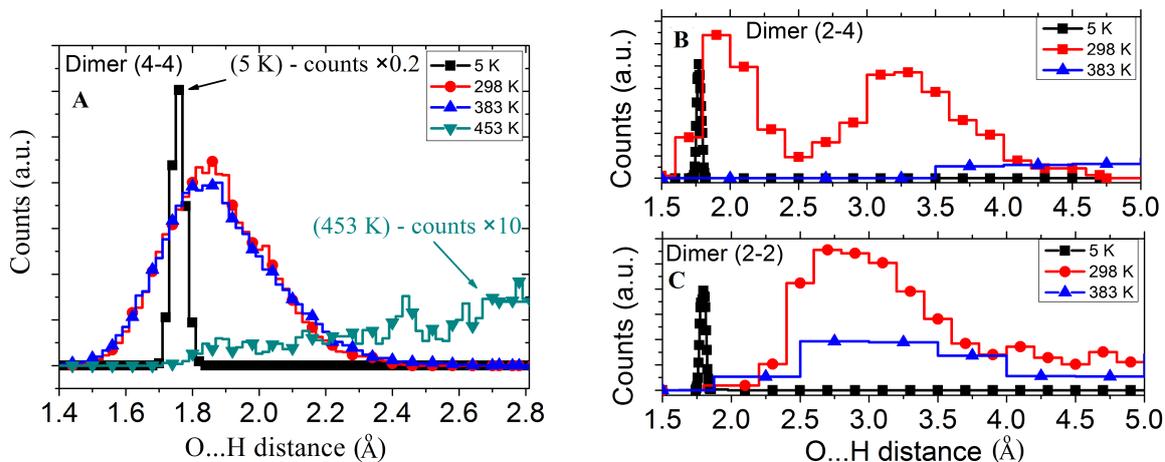
Fig. 4.30: Histogram of the evolution of the O$\cdots$H distance at different temperatures as obtained from the AIMD calculations. A: (4-4) dimer, B: (2-4) dimer, C: (2-2) dimer. Some data were scaled as indicated in the figure.

By following the evolution of vibrational peaks affected by hydrogen bonds with increasing temperature, the weakening and subsequent disruption of hydrogen bonds was identified at temperatures around 330-390 K. The following processes are responsible for hydrogen bond disruption: starting with more or less rigid dimers at room temperature, the melting is gradually induced by large thermal fluctuations in the dimers that lead a thermal equilibrium between different dimer configurations at intermediate temperatures. Above the sublimation temperatures for the two molecules the hydrogen bonds are finally disrupted, illustrating that the sublimation temperature provides a good estimate for hydrogen bond stability in such systems.

4.3.3 Bis-uracil linear molecular unit

In this part of this work I present a study on a uracil-based molecular solid, formed of 1,4-bis[(1-hexylurac-6-yl)ethynyl]benzene (molecule **3** in figure 4.6), investigating the nature of the interaction between molecular units in the crystalline environment by infrared spectroscopy. Theoretical results presented in this chapter were performed by Péter Nagy from Eötvös Loránd University, Budapest. This study is a continuation of the work on the simple monouracil derivative (1-hexyl-6-ethynyluracil (molecule **1**)) presented in the previous chapter [2]. Two units of **1** (figure 4.31 (a)), connected by a benzene ring, form **3** (figure 4.31 (b)). Molecule **1** is a monotopic molecule with hydrogen bond-forming sites at

one end, a prospective ingredient of dimer structures, while **3** is a ditopic molecule enabling the formation of a linear backbone as hydrogen bond-forming functional groups are present at its opposite ends. This ditopic uracil derivative unit is a very good candidate for a linear linker in self-assembled supramolecular networks. **3** has already proved its potential in forming 2D bicomponent hexagonal porous structures at the solid-liquid interface [64] as well as in molecular recognition through triple hydrogen bonds [25].
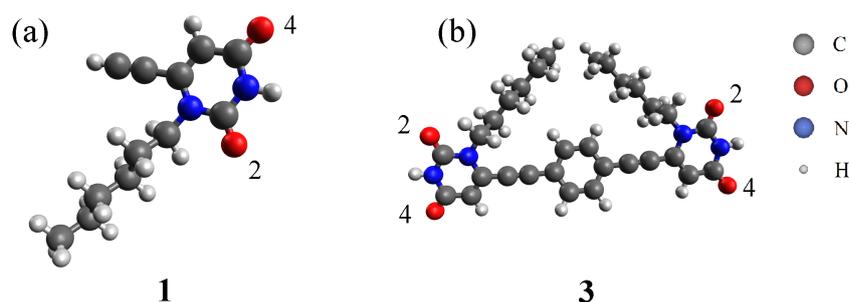
Fig. 4.31: 1 (a) and **3** (b) have identical hydrogen bond forming functional groups (the carbonyl and amine groups). The two carbonyl groups numbered 2 and 4, respectively, may participate in different hydrogen bonding motifs (work done by Péter Nagy).

Figure 4.32 presents the infrared spectra of **1** and **3** recorded in the solid state at room temperature and matrix isolation infrared spectra of isolated monomers recorded in an argon matrix at 8 K. Evaluating the possible dimer conformers of **1** (described in the previous chapter) the N-H (3) and one of the C=O groups (2 or 4) is always involved in hydrogen bond formation, while the other C=O group is free. In analogy, for **3** the hydrogen bonded C=O and N-H stretch modes are assigned to the bands at 1675 cm^{-1} and 3155 cm^{-1} and the free C=O to that at 1723 cm^{-1}. While the free carbonyl mode is at the same frequency for **1** and **3**, there is a considerable difference for the hydrogen-bond affected infrared bands. These bands shift to lower wavenumbers for **3** suggesting a stronger interaction of the molecular modules through hydrogen bonds. In the MI spectra (figure 4.32 (b)) the mode assignment of the isolated monomers of **1** was done by comparing with the theoretical spectrum calculated for monomers at 5 K [2]. The bands at 1719 cm^{-1} and at 1731 cm^{-1} belong to the free C_4=O and C_2=O (according to figure 4.31) vibrations of the monomer, respectively. For **2** the free vibration of C_4=O and C_2=O is assigned to the band at 1713 cm^{-1} and at 1731 cm^{-1}. The 6 cm^{-1} difference between the C_4=O vibrational

frequencies of the two molecules could be attributed to their structural differences. The band situated at 3428 cm^{-1} is assigned to the free N-H vibration and is at the same frequency for both units. Finally, the band at 3311 cm^{-1}, present only in **1**, corresponds to the ethynyl stretch mode $\nu(\equiv$C-H$)$.
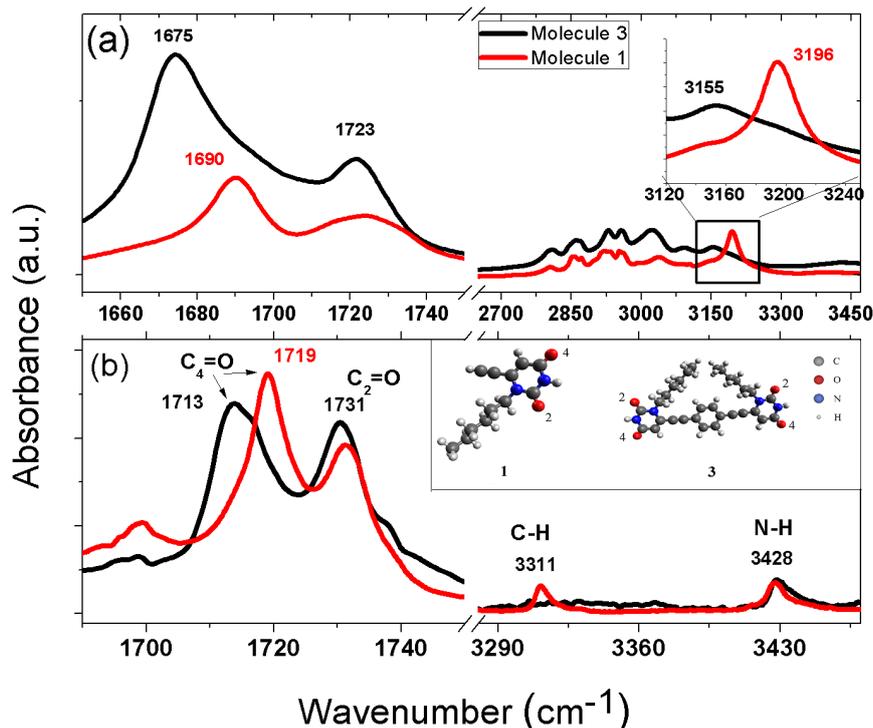
Fig. 4.32: (a) Experimental room temperature spectra of **1** and **3** and (b) MI spectra of the isolated molecular units. Subscripts 2 and 4 refer to the corresponding carbonyl groups according to figure 4.31.

In Table 4.5 the calculated dimerization energies for **1** and **3** for three different configurations are presented (according to figure 4.33). Looking at **1** first, the order of stability and the dimerization energies match previous theoretical results and experimental observations for **1** (dimerization energies were calculated with different method in the previous chapter). Comparing **1** and **3** we observe the same tendency, the most stable dimer configuration being the (4-4) conformer followed by the (2-4) and (2-2) conformers. The dimerization energy of **3** indicates a slightly stronger coupling through hydrogen bonds than for **1**, in agreement with the infrared results presented in figure 4.32.

Figure 4.34 presents the temperature dependence of the infrared spectrum of **3** from room temperature up to 573 K. There is an intermediate state between the stable hy-
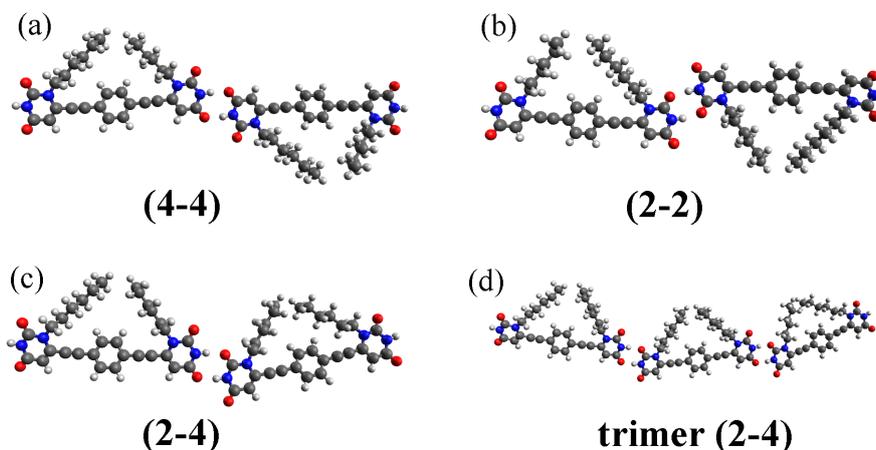
Fig. 4.33: The investigated dimer and trimer configurations of **3** in the theoretical study. For the dimer notation we indicate the labels of the carbon atoms (2 or 4) of the carbonyl groups taking part in the hydrogen bond (according to figure 4.18) (work done by Péter Nagy).

Tab. 4.5: Formation energies of the different isolated dimers for **1** and **3** (work done by Péter Nagy).

Dimer	**1** (kcal mol^{-1})	**3** (kcal mol^{-1})
(4-4)	-13.3	-14.8
(2-2)	-12.4	-13.4
(2-4)	-12.6	-13.9

drogen bonded phase at room temperature and the case of melted hydrogen bonds above 543 K. Between 473 K and 543 K the intense C=O hydrogen bonded band (at 1675 cm^{-1}) disappears and a new band appears at 1695 cm^{-1}. This temperature induced transition can also be characterized by studying the behavior of the amine group. N-H groups are always involved in hydrogen bonding between **3** molecules. One-step melting of hydrogen bonds would result in the appearance of free N-H vibration bands; here, however, the hydrogen bonded N-H band (at 3150 cm^{-1}) persists up to 543 K. All this indicates an intermediate phase, i.e. a phase transition at 473 K into a different, but still hydrogen bonded, structure. The hydrogen bonded N-H vibration, similarly to the hydrogen bonded C=O stretch, shifts towards higher wavenumbers at 473 K. Above 543 K the hydrogen bonded N-H band decreases in intensity and a new band appears at 3411 cm^{-1}, in the region characteristic of the free N-H vibrations.

In the following, a possible three dimensional arrangement of **3** is presented in agreement with all available experimental and theoretical data. Structural organization on a surface
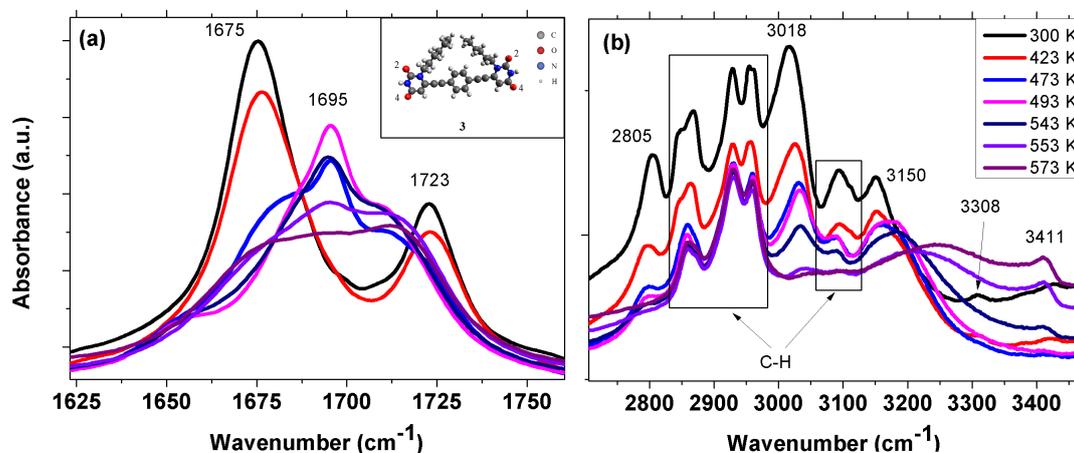
Fig. 4.34: Experimental temperature dependent infrared spectra of **3**. Above 473 K the band at 1675 cm^{-1} disappears and a new band appears at 1695 cm^{-1} which starts to decrease in intensity above 543 K. In the high frequency region the amine vibrations (3150 cm^{-1}) persist up to 543 K, above this temperature the free amine vibration band appears at 3411 cm^{-1} indicating the total melting of the hydrogen bonds.

was previously observed for **3** in an STM study [25]. This STM investigation, performed under ultrahigh vacuum on Ag(111) surfaces, provides important insight into the system of noncovalent interactions that governs the self-assembly of **3** (figure 4.35). The observed double-row supramolecular structure is illustrated also in figure 4.36(a) for four units. Although the (4-4) dimer is found to be slightly more preferred energetically (cf. table 4.5), the STM image verifies that a close-packed crystal structure can only be built with (2-4) type hydrogen bonds. Furthermore, the all-cis configuration of the hexyl chains was found to be more abundant in Ref. [25] even at submonolayer coverage in two dimensions. Therefore we continue with the theoretical study of the supramolecular structure shown in figure 4.36(a).

First of all, parallel linear assemblies are created by double hydrogen bonds between **3** units (cf. figure 4.33(d)). Theoretical investigation reveals that double hydrogen bonds can be formed on both ends of **3** molecules practically independently. Therefore this linear structure can grow to any length, since the stabilization energy, corresponding to the energy required for the extension of the chain by a single unit, is independent of chain size. This tendency is illustrated for the cases of trimers and tetramers in table 4.6.
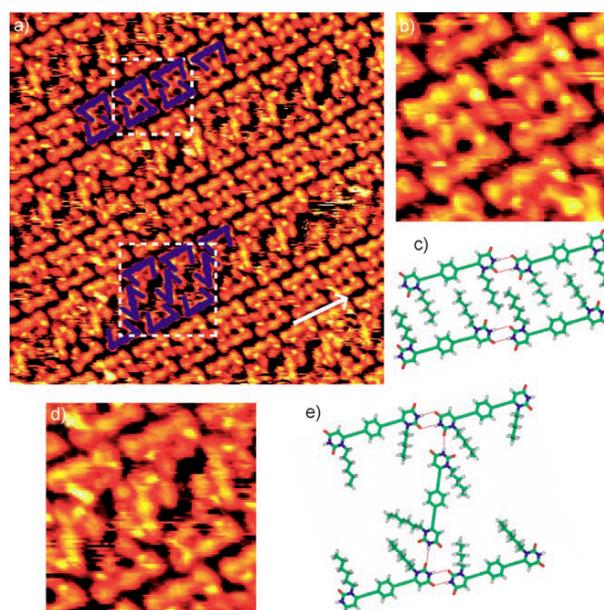
Fig. 4.35: (a) STM image of molecule **3** on Ag(111) (scan range 16 x 16 nm^2). (b) and (d) STM images of the two zoomed regions in (a). (b) scan range 4 x 4 nm^2 and (d) scan range 4.5 x 4.5 nm^2. (c) and (e) proposed hydrogen bonding models of the assemblies [25].

(a)   (b)

Tetramer   Stacked dimer
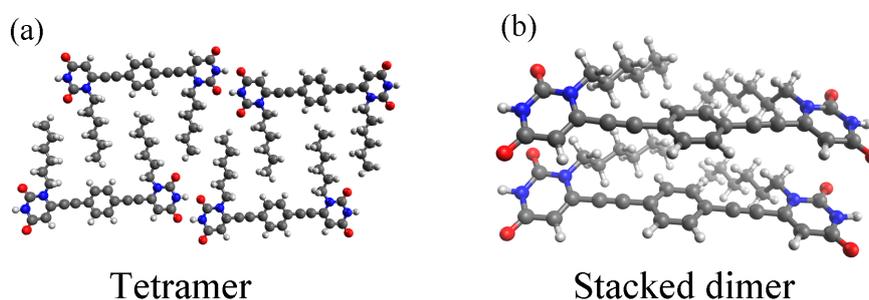
Fig. 4.36: Double-row wire structure organized by double hydrogen bonds and van der Waals interactions between linear molecular assemblies (a). Organization perpendicular to the molecular plane due to π–π stacking (b) (work done by Péter Nagy).

Tab. 4.6: Formation energies for dimer, trimer and tetramer of the (2-4) conformer of **3** (work done by Péter Nagy).

Dimer (kcal mol^{-1})	Trimer (kcal mol^{-1})	Tetramer (kcal mol^{-1})
-12.97	**-25.92**	**-38.85**
	($\sim$ 2 x -12.97)	($\sim$ 3 x -12.97)

The second organizing principle is the interdigitation of the laterally placed hexyl chains stabilized by van der Waals attractions. To approximate the magnitude of the van der Waals stabilization energy compared to hydrogen bonding, theoretical calculations were carried

out on the substructures of the tetramer in figure 4.36 (a). Dimerization energies for the van der Waals and hydrogen bonded dimers were found to be -8.3 kcal/mol and -14.6 kcal/mol, respectively.

Organization in the third direction, perpendicular to the aromatic planes, is governed by π-π stacking of the aromatic rings (figure 4.36 (b)). This is supported by previous investigations of π-π interactions in uracil based crystals [87] and in stacked uracil dimers [88, 89]. In case of **3**, π-π stacking is particularly strong due to the three parallel aromatic rings. Dimerization energy for the dimer in figure 4.36 (b) is -33.6 kcal/mol, which consists of mainly π-π stacking and partly hexyl-hexyl van der Waals interaction.

Since the van der Waals interaction turns out to be the lowest in energy, it is probable that it provides the "weakest link" to induce the transition at 473 K. Due to the large difference in the stabilization energies, the stronger double hydrogen bonds are expected to be relatively intact at that temperature. This argument is supported by previous room temperature AIMD infrared computations on the (2-4)-type double hydrogen bonded **1** dimer [2]. This structural change can also explain the transition of the hydrogen bonded C=O band from 1675 cm^{-1} to 1695 cm^{-1}. At lower temperature the additional van der Waals attraction, being parallel to the double hydrogen bonds, shortens the hydrogen bond lengths. This is illustrated in table 4.7 by comparing the computationally obtained geometrical parameters of the (2-4) dimer, the (2-4) linear tetramer and the double-row tetramer of figure 4.36 (a). Structures without the extra van der Waals stabilization have hydrogen bond lengths around 1.825 Å and 1.815 Å, while a significant decrease of cca. 0.06 Å can be found for the double-row structure. A shorter hydrogen bond length implies a lower force constant and thus lower frequency for the hydrogen bonded C=O vibration, in accord with the experiment.

Tab. 4.7: Computed hydrogen bond length values for different complexes of **3** (work done by Péter Nagy).

Hydrogen bond length (Å)	C$_4$=(**O**$\cdots$**H**)-N	C$_2$=(**O**$\cdots$**H**)-N
dimer (2-4)	1.825	1.815
tetramer (2-4), linear chain	1.822-1.825	1.816-1.818
tetramer (2-4), double-row	1.76, 1.78	1.73, 1.77

In light of all data, the room temperature spectrum is assigned to a crystal structure of ordered double-row linear assemblies. These assemblies are formed via double hydrogen

bonds from monomers, and are organized into a double-row structure due to van der Waals interactions between laterally placed hexyl groups. Different layers of this practically planar arrangement are kept together by π-π stacking.

At an intermediate temperature of 473 K the hydrogen bonded C=O band is shifted to a higher wavenumber, but the hydrogen bonds are not disrupted yet, according to the frequency of the amine band. The increase in the C=O frequency can be attributed to the disintegration of the weakest cohesive force, the van der Waals interactions between the hexyl chains. The full melting of the hydrogen bonds was observed at 543 K, where the intensity of the hydrogen bonded amine band decreases and a new band appears in the wavenumber region characteristic of free N-H vibrations. In conclusion the supramolecular order in the three perpendicular directions of the solid crystal is governed by three different noncovalent interactions: double hydrogen bonds, van der Waals attraction and π-π stacking. This structure is consistent with temperature dependent infrared and 2D STM measurements and theoretical results as well. This arrangement is particularly interesting, since the strength of these interactions vary in a wide range, which may permit direction-specific manipulations of this structure.

4.4 Heteromolecular ordering in the solid state

In this chapter, I describe the heteromolecular association between the (ADA) molecule **4** and the (DAD) molecule **7** (figure 4.37) [1]. These molecules were studied in the solid
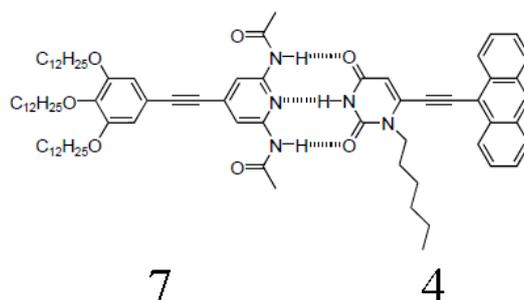
Fig. 4.37: Hetero-molecular self association between the (ADA) molecule **4** and the (DAD) molecule **7**.

state by infrared spectroscopy, and at the solid-liquid interface by means of STM (STM results presented in this section were measured by L. Piot, C.-A. Palma, and P. Samorì

from Louis Pasteur University, Strasbourg). Molecules **4** and **7**, bearing complementary hydrogen bonding sites, have been designed to undergo physisorption on HOPG into highly ordered monolayers at the solid-liquid interface. Physisorption on graphite has been promoted by the presence of alkyl chain side groups in the molecular structures [27]. Figure
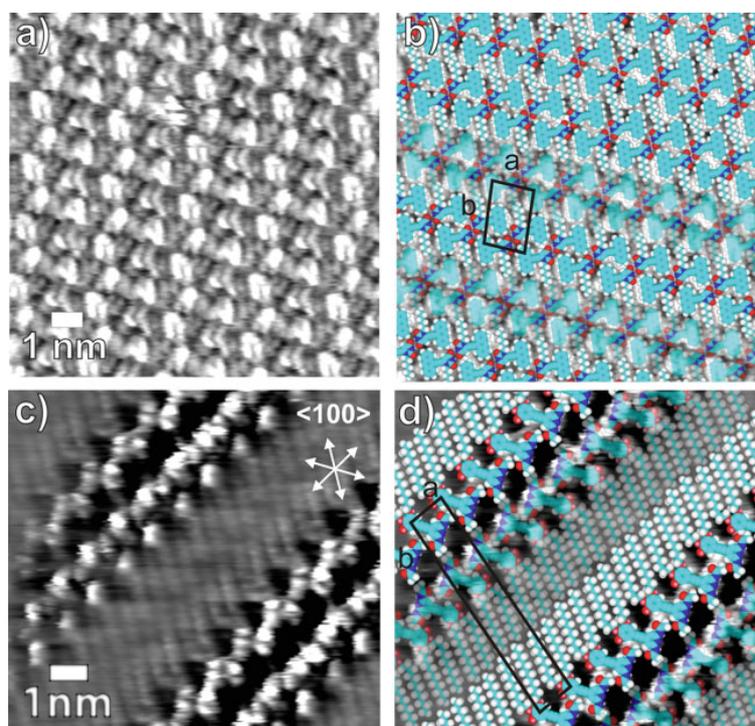
Fig. 4.38: STM images recorded at the graphite-solution interface. (a) Height image of mono-component monolayers of molecule **4** and (b) its proposed packing model. (c) Current image of monolayer of **7**, and (d) its proposed packing motif showing that one alkoxy chain per molecule is not adsorbed on the surface [1] (work done by L. Piot, C.-A. Palma, and P. Samorì).

4.38 presents the mono-component monolayers of **4** (a) and **7** (c) as well as the proposed self-assembling models of them (b) and (d). The corresponding packing motif shown in the cartoon reveals the occurrence of homo-association, that is, the formation of two (i.e., double) N-H$\cdots$O bonds among adjacent molecules thus forming (**4**)$_2$ dimers. Similarly, molecule **7** was deposited from a 1-phenyloctane solution on the HOPG surface, resulting in the formation of a monolayer with a lamellar structure displayed in figure 4.38 (c).

Figure 4.39 presents the monolayer formed by co-adsorption of **4** and **7**. Both molecules have chemical structures which can be expected to give rather different STM contrasts when physisorbed on HOPG. The STM image reveals bright rods, the length of which is in good accordance with the cumulative contour lengths of molecule **4** and the conjugated

fragment of molecule **7**, whereas the darker areas correspond to the adsorbed alkoxy chains of molecule **7**. In figure 4.39 a molecular pattern of the molecules **7** (in blue) and **4** (in yellow) is proposed. In combination with the underlying STM image, it provides strong evidences for the existence of [1·2] dimers on the surface held together by triple hydrogen bonds.
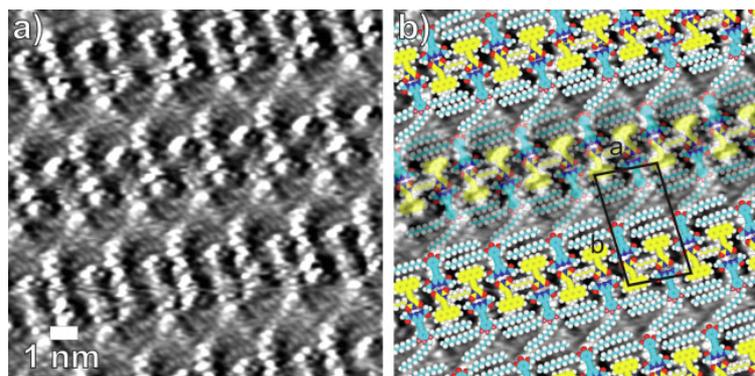
Fig. 4.39: (a) STM current image of the monolayers formed by mixing molecule **4** and **7** on the HOPG-solution interface. Each dimer is composed by one molecule **7** (blue) and one molecule **4** (yellow). (b) Proposed model of the assembly [1] (work done by L. Piot, C.-A. Palma, and P. Samorì).

The unambiguous assignment of the heteromolecular hydrogen-bond-related features is not straightforward, due to the complexity of the systems under study, in particular given that molecule **4** forms a dimer through homo-molecular association in the solid state and in solution. Such homomolecular dimers exhibit similar vibrations to those of the heteromolecular complexes. However, the vibrational modes can be determined exactly: i) upon comparison of the differences in the spectra of the starting materials and those of the hydrogen bonded adducts and ii) from variable temperature spectra, because at high temperatures (393 - 413 K) the hydrogen bonds become weaker or entirely disrupted [66].

Although the 2,6-di(acetylamino)pyridine-uracil pair has been extensively used for the formation of supramolecular polymers, [58, 59, 90] only a limited number of reports deal with spectroscopic investigations in the infrared region for such heteromolecular dimers [68]. The supramolecular dimer [**4**-**7**] was prepared by mixing an equimolar solution of molecules **4** and **7** followed by solvent evaporation. The spectra were recorded by mixing the as obtained powder with KBr. Figure 4.40 reveals that the [**4**-**7**] dimer spectrum is not the spectral sum of its constituents **4**+**7**, but essential differences appear in the typical hydrogen bond perturbed regions. Figure 4.40 (b) displays the N-H and C-H stretch region
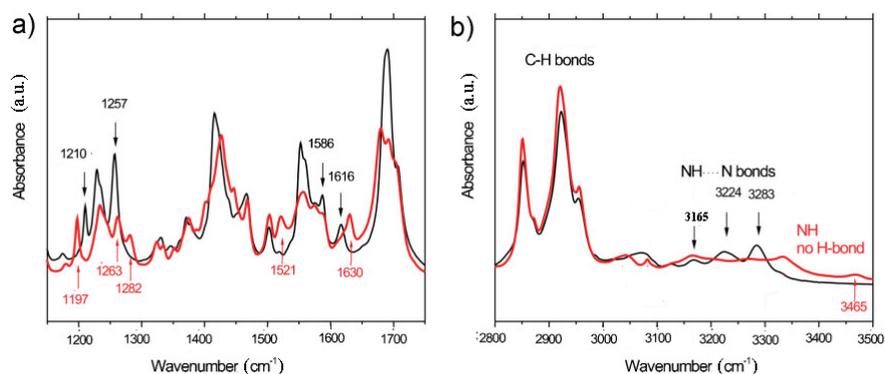
Fig. 4.40: a) Mid-frequency-range infrared spectra of dimer [**4**-**7**] (black) and of the sum **4**+**7** (red) of the separated molecular constituents. b) infrared spectra in the N-H and C-H stretching region of dimer [**4**-**7**] (black) and the sum **4**+**7** (red) of its separated molecular constituents. All spectra were recorded on powders ground in KBr pellets at room temperature.

in detail. The peaks at 2800-2900 cm^{-1}, corresponding to C-H stretching vibrations, [91] remain unaffected upon the formation of the hydrogen bonding interactions. In contrast, the peaks between 3000 and 3500 cm^{-1} are strongly perturbed. The spectral sum of **4** and **7** features homo-molecular hydrogen bonds typical of $(\mathbf{7})_2$, as evidenced from the peaks at 3165 cm^{-1}. The peak at 3465 cm^{-1} can be assigned to the stretching frequency
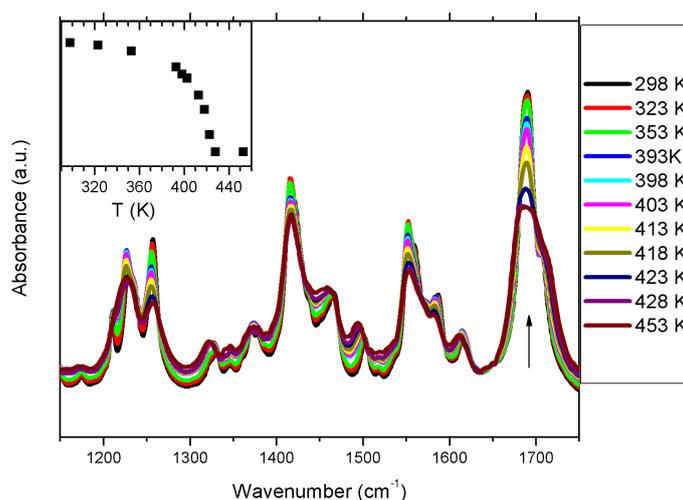
Fig. 4.41: Mid-frequency spectrum and its dependence on the temperature for dimer [**4**-**7**] in KBr pellets. Inset: peak intensity of the 1690 cm^{-1} mode as a function of the temperature.

of the hydrogen bond free N-H groups existing in 2,6-di(acetylamino)pyridine moiety (**7**).

This frequency is comparable to that found in the vapor phase spectra of 2-aminopyridine [92] and matrix isolation spectra of thymine [93]. In dimer [**4**-**7**], this feature disappears completely. New features appear at typical N-H stretch modes, [94] i.e., those at 3165, 3224, and 3283 cm^{-1}. These modes are redshifted when compared to the hydrogen bond free N-H frequency of the 2,6-(diacetylamino)pyridine moiety at 3465 cm^{-1}, providing evidences for the formation of hydrogen bonds [95]. Thus the heteromolecular dimer [**4**-**7**] appears as having all three nitrogen atoms bridged through hydrogen bonds (figure 4.37). The region between 1200 and 1700 cm^{-1}, typical of skeletal vibrations, C=O stretching and N-H in-plane bending modes can be analyzed along the same lines (figure 4.40). We have indicated in the figure the unique modes of the constituents and of the complex. The temperature-dependent spectra of dimer [**4**-**7**] detailed in figure 4.41 prove that the peaks at 1210, 1329, 1464, 1501, 1581, and 1690 cm^{-1} are considerably affected by the hydrogen bonds. Among these, three peaks (positioned at 1214, 1464, and 1501 cm^{-1}) coincide with the features assigned by Rozenberg *et al.* to the uracilic vibrations with major contributions from N-H in-plane bending modes [96], and one (located at 1690 cm^{-1}) with the uracilic C=O stretching as reported by Barnes et al. [91]. This further confirms the formation of three parallel hydrogen bonds between molecules **4** and **7**. As discussed by Iogansen, [95] the intensities of the vibrational bands are correlated to the strength of the hydrogen bonds. The inset of figure 4.41 shows the intensity of the 1690 cm^{-1} peak as a function of temperature; as expected, profound changes in the typical temperature range (between 393 and 413 K) of hydrogen bond weakening occur [66]. Figure 4.42 summarizes the hydrogen bond related structures in the infrared spectrum upon comparison of [**4**-**7**] dimer at room temperature and 453 K and the spectral sum of its constituents. Additionally, the far-infrared spectral region, where the direct vibrations of the hydrogen bonds appear, is also displayed. Far-infrared spectra have been taken on neat powders between polyethylene disks. The vibrational mode at 119 cm^{-1} originates from the 2,6-(diacetylamino)pyridine moieties of molecule **7** thus corresponding to the N-H$\cdots$N bond [33]. A new feature also appears in the spectra of complex [**4**-**7**] at 217 cm^{-1}, which, based on analogy with other systems, [34] is assigned to the N-H$\cdots$O bond.
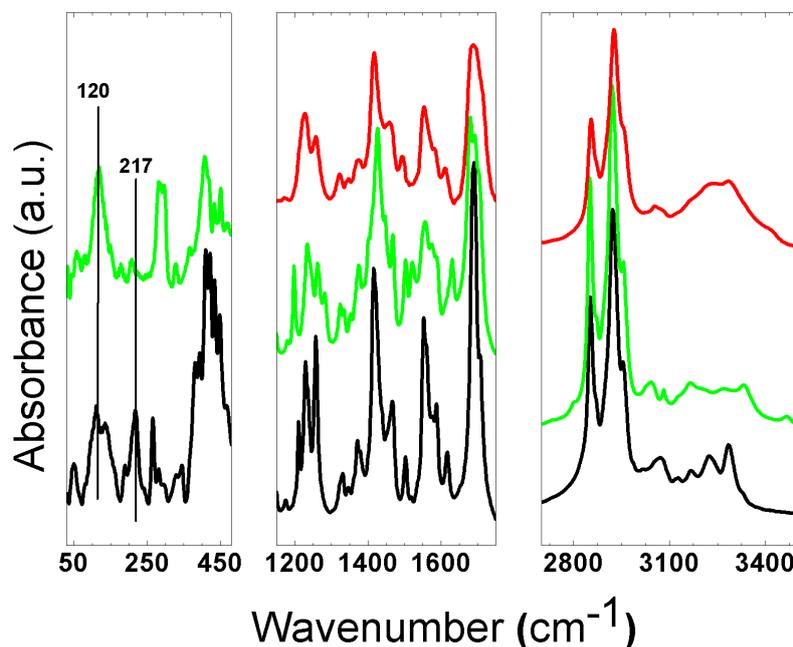
Fig. 4.42: Comparison of the infrared spectrum of complex [**4**-**7**] at 300 K (black) and at 453 K (red) with that of the sum **4**+**7** (green) of its constituents alone at room temperature. In the far-infrared (left panel), the vibrations of the hetero-molecular hydrogen bonds appear at 120 and 217 cm^{-1}. In the C=O stretching region (middle panel), both homo-molecular $(\mathbf{4})_2$ and hetero-molecular [**4**-**7**] intermolecular interactions influence the spectra between 1200-1300 and 1500-1750 cm^{-1} regions. Similarly, the signatures of N-H$\cdots$N bonding interaction appear between 3200 and 3400 cm^{-1}.

4.5 Summary

The dynamics of hydrogen bonds in supramolecular systems have been studied using spectroscopic characterization. Different prototypical molecules were investigated using different methods of infrared spectroscopy. Matrix isolation infrared spectroscopy provided spectra of isolated monomers. The combination of matrix isolation and temperature dependent infrared spectroscopy opens new possibilities in the study of supramolecular hydrogen bonded systems. Experimental and theoretical (performed by collaborators) investigations reveal the mechanism behind hydrogen bond breaking. Hydrogen bonding patterns are completely locked in at cryogenic temperatures. Around room temperature, the amplitude of the hydrogen bond affected vibrations increases significantly, and a dynamic conformer exchange is possible which leads to broadening of the hydrogen bonded peaks. Further temperature increase above the sublimation temperature of each molecule (determined during the ma-

trix isolation experiment) leads to melting of the system. Based on the experimental and theoretical results reliable predictions can greatly reduce the cost and effort of determining hydrogen bond dynamics in systems important for biology or nanoscience.

Thesis points related to the chapter:

[1] I prepared an infrared spectral library for the molecular constituents for hydrogen bonded systems. Starting from the basic molecular units and finishing with the final supramolecular assemblies I measured and interpreted the infrared spectra of the supramolecular ordering of different imide-uracil and acetylaminopiridyne based molecular constituents by infrared transmission spectroscopy. [1, 2, 3]

[2] I studied the direct evidence of the presence of hydrogen bonds for a pair of monotopic uracil-derivative molecules measuring the spectra of the isolated molecules and that of the aggregated state. For this I applied different methods of infrared spectroscopy: matrix isolation and conventional transmission spectroscopy. I could identify the weakening and subsequent disruption of hydrogen bonds by following the temperature dependence of the affected vibrational bands. The assignment of the processes responsible for the melting of hydrogen bonds was done: a gradual increase of the temperature to intermediate values induces large thermal fluctuations in the dimers that leads to a thermal equilibrium between different dimer configurations. I found that further increase of the temperature above the sublimation point of the molecules the hydrogen bonds are disrupted, indicating that the sublimation temperature provides a good estimate for hydrogen bond stability in such systems. These results are consistent with theoretical results. [2]

[3] I studied the supramolecular ordering in the solid state of bis-uracil based linear molecules by different infrared spectroscopic methods. A temperature-induced transition from a highly ordered tetrameric into a linear assembly was observed by temperature dependent infrared measurements. The interaction between molecules in the three perpendicular directions of the solid crystal is governed by three different noncovalent interactions: double hydrogen bonds, van der Waals attraction and π-π stacking. [3]

Publications related to the chapter:

[1] L. Piot, C. A. Palma, A. Llanes-Pallas, Zs. Szekrényes, K. Kamarás, M. Prato, D. Bonifazi and P. Samorì, Selective formation of bi-component arrays through H-bonding of multivalent molecular modules, *Adv. Funct. Mater.*, 19:1207, 2009 (cover page).

[2] Zs. Szekrényes, K. Kamarás, G. Tarczay, A. Llannes-Pallas, T. Marangoni, M. Prato, D. Bonifazi, J. Bjork, F. Hanke, M. Persson, Melting of Hydrogen Bonds in Uracil Derivatives Probed by Infrared Spectroscopy and ab Initio Molecular Dynamics, *J. Phys. Chem. B*, 116:4626, 2012.

[3] Zs. Szekrényes, K. Kamarás, P. Nagy, G. Tarczay, A. Llannas-Pallas, L. Maggini, M. Prato, D. Bonifazi, Direction-dependent secondary bonds and their stepwise melting in a uracil-based molecular crystal studied by infrared spectroscopy and theoretical modeling, *under submission.*

5. Characterization of silicon carbide quantum dots

5.1 Introduction

SiC is a stable, chemically inert wide band gap semiconductor with excellent hardness, heat resistance and chemical resistivity [97]. Among applications in electronic devices and circuits [98–102] SiC is also known as a biocompatible material [103–105] with very promising results in living cell implantation for bioimaging techniques [7, 106–109]. The emergence of nanotechnology in the field of cell biology gave rise to the implementation of quantum dots in cell labeling [110]. Considering the requirements for the ideal in vivo luminescent biomarkers (to be nontoxic, bioinert, photostable, not blinking, ultra small size) and comparing to the widely used II-VI semiconductor quantum dots (e.g. CdSe), SiC quantum dots are among the best candidates for biological applications [5, 110]. Indeed, ultra small SiC quantum dots have been successfully applied as biological labels in cells without any protective shells [106, 107]. Depending on the starting bulk powder, the surface of SiC quantum dots is often rich in various functional groups which can result in diverse behavior in biological environments ranging from bioinertness to changes in cell function and cytotoxicity [7, 111]. While the successful application of the SiC quantum dots in bioimaging techniques is related to their bioinert and photostable properties [5, 106], further applications of the SiC quantum dots in medicine and drug delivery rely on the ability of engineering the desired surface properties by attaching different functional molecular groups. To obtain tailor-made functionalized surfaces it is necessary to understand the complex structure of the quantum dots surface.

There are several experimental and theoretical studies in the literature about the surface chemistry of SiC quantum dots where the presence of Si-O-Si, C-O-C, C=O, and -OH

groups was observed [4, 5, 112–118]. Photoluminescent properties of the SiC quantum dots, as those of other quantum dots, are greatly influenced by their surface chemical structure as some surface radicals can form new energy levels in the band gap and can act as new radiative centers [117, 118]. Even though some studies explain the optical properties of SiC quantum dots by the existence and dissociation of hydroxyl groups, clear evidence of Si-OH or C-OH terminations is still absent because of the complex vibrational region above 3000 cm^{-1}, where vibrations of adsorbed water overlap with the surface related -OH vibrational bands. Experiments concerning the solvent polarity dependence of the photoluminescence (PL) of SiC quantum dots yielded conflicting results in the literature. While Zakharko *et al.* [119] measured a red shift with decreasing solvent polarity in the emission spectra, Chu *et al.* [120] found the opposite trend, a red shift with increasing solvent polarity. The importance of understanding and controlling the surface structure is also significant from the point of view of pH sensitivity [111]. One possible explanation for the different physical and chemical properties of similar SiC quantum dots solutions is related to the diversity in surface terminations which can be related to the variations of the carboxyl concentration or the amount of Si on the surface.

This chapter is organized as follows. In section 5.2 I present a literature overview of basic luminescent and vibrational properties of SiC starting from luminescence of bulk and microstructured SiC (section 5.2.1). In section 5.2.2 I present experimental evidence of quantum confinement effect on the PL properties of SiC quantum dots. Section 5.2.3 describes vibrational modes of crystalline SiC studied with infrared spectroscopy. In section 5.3 and 5.4 I present my results on the study of complex surface structure of SiC quantum dots revealed by infrared spectroscopy and the chemical transformation of carboxylic groups on the surface of SiC quantum dots as determined from the temperature dependence of their infrared spectra.

5.2 Optical and vibrational properties of silicon carbide

5.2.1 Luminescence of bulk and microstructured silicon carbide

SiC is an indirect band gap semiconductor with band gap values of 2.4, 2.9, and 3.2 eV for the cubic 3C, hexagonal 6H, and hexagonal 4H polytype, respectively. In an indirect band gap semiconductor the maximum of the valence band and the minimum of the conduction band are at different k values in the Brillouin zone [121]. Figure 5.1 shows the interband emission processes that occur in an indirect band gap semiconductor. The interband transition must involve the absorption or emission of a phonon to fulfil the criteria for momentum conservation [121]. The radiative transition probability is relatively small because of the
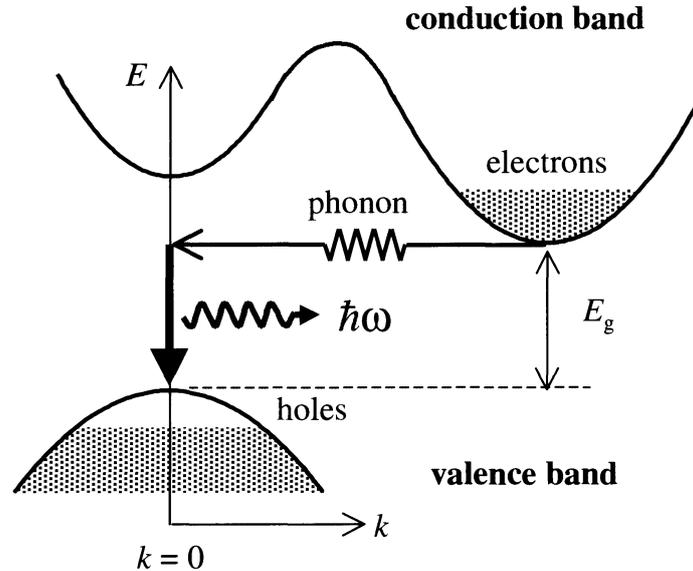
Fig. 5.1: Schematic representation of the interband luminescence in an indirect band gap material [121].

involvement of phonon emission as well as of the competition with non-radiative recombination. For these reasons the luminescence efficiency of indirect gap semiconductors is small and light emitting properties are poor [121–123]. On the other hand experiments on silicon have shown a significant increase in the emission intensity when the crystallite size decreased to several tens of nanometers [123, 124]. Such experiments were done by

electrochemical dissolution steps to define a mesoporous Si layer of high porosity. X-ray absorption fine structure (XAFS) experiments have proved that quantum size effects are at the origin of the increased luminescence [125].

Hwang *et al.* [126] observed anomalous photoluminescence at room temperature on 3C-SiC epitaxial layer grown on Si(111) after removal of the Si substrate by etching. Figure 5.2 presents the photoluminescence spectra of the SiC/Si sample in comparison with the free SiC film. As expected in the case of an indirect band gap semiconductor, SiC/Si does not show any luminescence. In contrast, the back surface of the free SiC film exhibits very strong emission centered at around 2.4 eV (516 nm) and also a weak peak at 3 eV (413 nm). Scanning electron microscopy (SEM) and infrared investigations of the free SiC film suggested that the origin of the blue/green luminescence may be attributed to OH containing light emitting centers (as a consequence of the chemical compounds produced during the etching reaction of the back surface) or some localized states such as a CH bond near the interface [126].
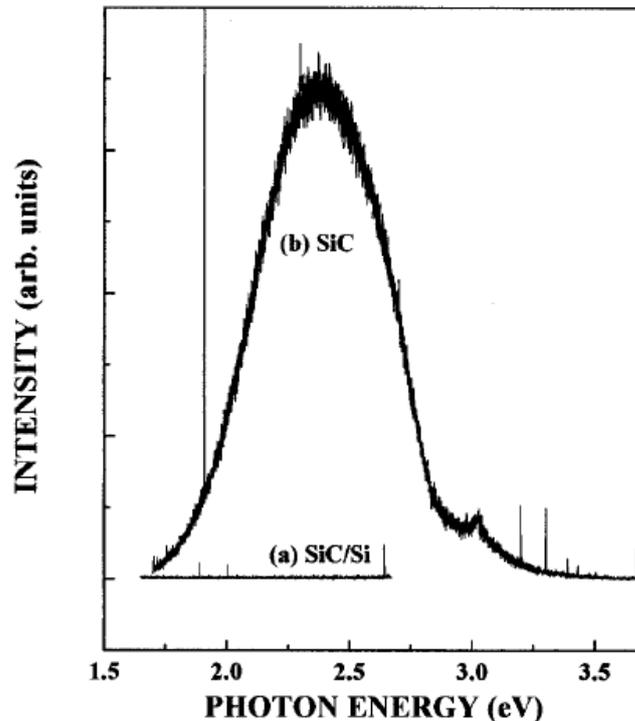
Fig. 5.2: PL spectra of (a) SiC/Si and (b) free SiC film excited with a 325 nm line from a He-Cd laser recorded at room temperature [126].

5.2.2 Evidence for quantum confinement photoluminescence of silicon carbide quantum dots

Blue-green PL on porous 6H-SiC was first reported in Ref. [127]. Porous SiC was fabricated with the same electrochemical anodization process as porous Si. Figure 5.3 shows the PL spectra of two porous SiC samples together with the spectrum of the bulk SiC substrate. The luminescence intensity for the sample (a) was found to be approx. 500 times stronger than that of the donor-acceptor recombination in the crystalline 6H-SiC and the PL band has moved to higher energy with increasing anodization current density. However the PL band position (460 nm for the 60 mA/cm^2 sample) is below the band gap of the 6H-SiC crystal (430 nm) and is different from what is expected from the quantum confinement effect. Time-resolved luminescent measurements as a function of porosity indicated that the carrier generation occurs in the core-crystal part and the excited carriers are rapidly transferred (within 10 ps) to surface states. The surface regions are responsible for the strong emission.
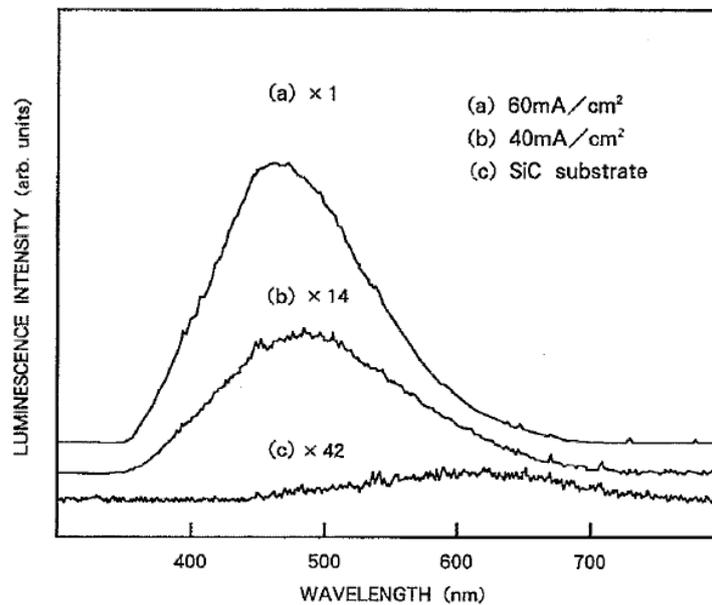
Fig. 5.3: PL spectra of porous SiC with an anodization current density of (a) 60 mA/cm^2, (b) 40 mA/cm^2 and (c) crystalline SiC substrate [127]. Spectra were measured with excitation wavelength of 325 nm of a He-Cd laser at room temperature.

For very small crystals the optical properties will show size dependence [121]. The first experimental evidence of quantum confinement effect on SiC was reported by Chu *et al.*

[128]. Suspensions of 3C-SiC nanocrystallites in the size range 1-6 nm were prepared by electrochemical etching of 3C-SiC target followed by ultrasonic treatment in water solution. The colloidal suspension of SiC quantum dots shows clear evidence for quantum confinement effect exhibiting strong photoluminescence ranging from 440 to 560 nm [128]. Figure 5.4 presents a TEM image of nearly spherical SiC particles. The average size was found to be 3.9 nm.
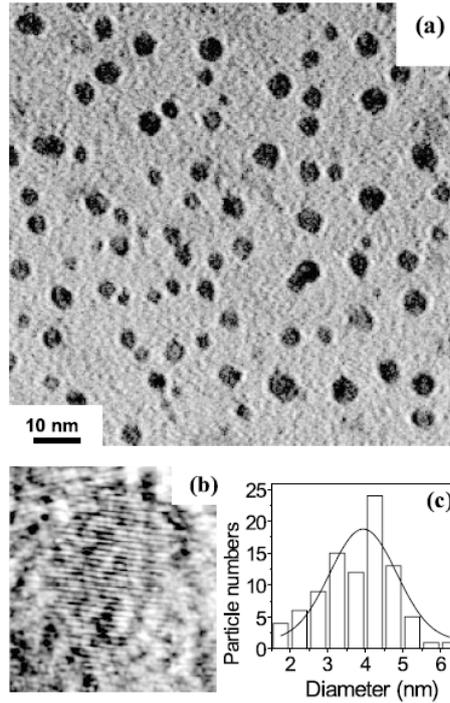
Fig. 5.4: (a) TEM image of SiC quantum dots with near spherical geometry. (b) HRTEM image of one quantum dot. Lattice spacing corresponds to the (111) plane of 3C-SiC. (c) Size distribution of SiC quantum dots obtained using Gaussian fitting. The average size is 3.9 nm [128].

While the size distribution is almost continuous [according to figure 5.4 (c)] at lower excitation energies only larger quantum dots will show luminescence. Due to such quantum confinement effects the PL band of the colloidal solution should red shift with increasing excitation wavelength [4, 128]. Figure 5.5 presents this red shift of the photoluminescence as a function of excitation wavelength. Theoretical calculations using effective mass theory [129] on the exciton ground states in 3C-SiC show that the band diagram of quantum dots is quite different from the bulk. The band gap increases as the particle size is decreasing. The band gap of the bulk 3C-SiC is 2.4 eV and due to quantum confinement effect it increases to approx. 2.5, 2.6, 2.75, and 3 eV for SiC quantum dots with diameters of 4,

3, 2, and 1.5 nm, respectively [128, 129]. The spectral red shift of the photoluminescence represents the evidence for quantum confinement: at lower excitation energies the small quantum dots with high band gaps will not be excited. To measure the photoluminescence from the entire particle distribution it is necessary to use excitation energies in the UV range.
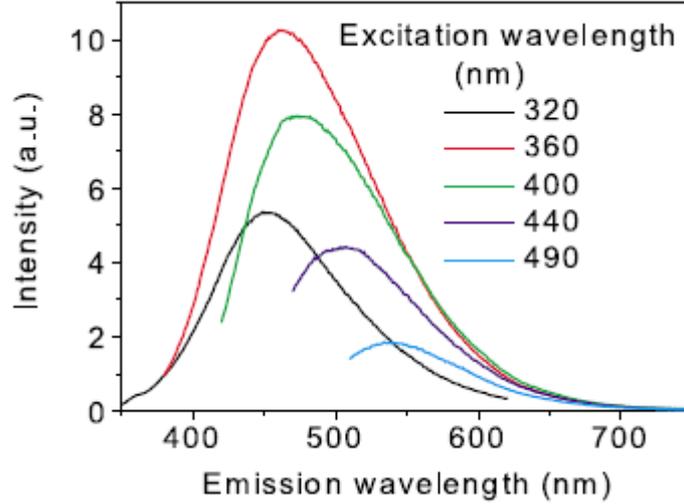
Fig. 5.5: PL spectra of the 40 mA/cm^2 sample measured with different excitation wavelengths [128].

5.2.3 Vibrational modes of crystalline silicon carbide

The interaction of infrared light with crystalline SiC is dominated by the vibrations of Si and C atoms against each other [130]. Due to the transverse nature of the electromagnetic waves, they can apply driving forces only to the transverse vibrations of the crystal (i.e. they can couple only to the transverse optic (TO) phonon mode) [121]. The longitudinal optic (LO) phonon mode, on the other hand, plays an important role in the infrared properties of a crystal [121]. Curve (1) of figure 5.6 presents a typical reflectance spectrum of a single-crystal 3C-SiC layer [131]. The nearly 100 % reflectivity between $\approx$ 700 and 1000 cm^{-1} is the so-called reststrahlen band and is related to the excitation of the fundamental phonon mode of SiC ($\tilde{\nu}_{TO} = 794\ cm^{-1}$, $\tilde{\nu}_{LO} = 973\ cm^{-1}$ [132]). The reflectivity (R) (introduced in chapter 2.2) is related to the complex refractive index (η) and complex dielectric function ($\hat{\epsilon}$) according to equation 5.1.

$$R = \left| \frac{\eta - 1}{\eta + 1} \right|^2 = \left| \frac{\sqrt{\hat{\epsilon}} - 1}{\sqrt{\hat{\epsilon}} + 1} \right|^2 , \qquad (5.1)$$
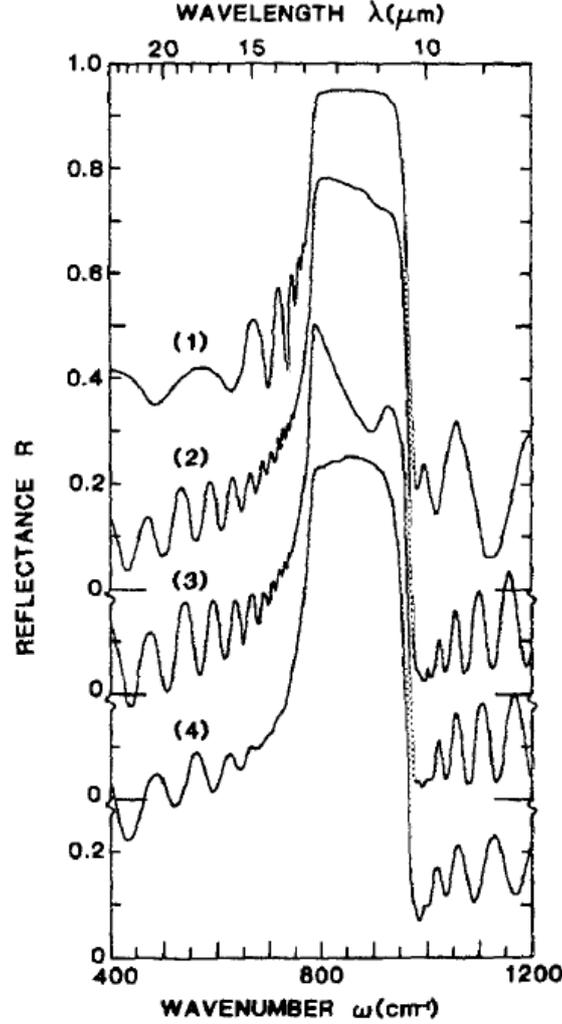
Fig. 5.6: Experimental reflectance spectra of SiC samples with different surface conditions in the reststrahlen region : ((1) crystalline, as prepared SiC surface, (2) slightly rough surface, (3) moderately rough, and (4) mechanically polished SiC surface) [131].

According to figure 5.6, R increases to unity as $\tilde{\nu}$ approaches $\tilde{\nu}_{TO}$. In the frequency region between $\tilde{\nu}_{TO}$ and $\tilde{\nu}_{LO}$ the reflectivity remains $\approx 100\,\%$. At $\tilde{\nu} = \tilde{\nu}_{LO}$, $\epsilon_r = 0$ [10, 121, 133] and $R = 1$. R drops rapidly to zero as $\tilde{\nu}$ increases above $\tilde{\nu}_{LO}$. The reason why in the experimental data R is less than 1 as predicted by the theoretical model (eq. 5.1) is caused by ignoring the damping [121]. Another reason is that the reflectance at the top of the reststrahlen band is sensitive to the surface structure of the material [131]. This dependence is illustrated in

figure 5.6 by curves (2)-(4). Spectrum (2) is recorded on a slightly rough SiC surface, (3) on a moderately rough, and (4) on a mechanically polished SiC surface. With an increase of the surface roughness a dip can appear in the high frequency part of the reststrahlen band (spectrum (2)) which can become a deep notch for higher imperfections (spectrum (3)) [131]. In such cases scattering of the infrared light becomes strong. Similar effects in the reststrahlen band are expected in process of fabrication of SiC quantum dots.
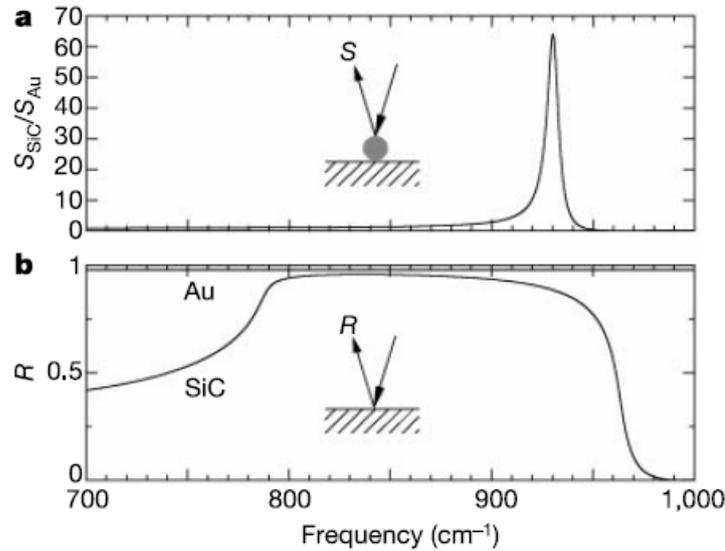
Fig. 5.7: (a) Enhancement and narrowing of the spectral response of crystalline SiC by the near-field interaction. (b) Reststrahlen band of SiC in the far-field and reflectivity of Au. [134].

Another interesting method to study the fundamental lattice vibrations is their coupling with optical near fields in the infrared [134]. This can be done by combining infrared spectroscopy with near-field microscopy accessible by a recent development in the 'apertureless', scattering-type scanning near-field optical microscopy (s-SNOM) [135–140]. Figure 5.7 (a) presents the resonant near-field response of SiC. This behavior is very different from the far-field response presented in figure 5.7 (b) where in the reststrahlen band region (from ≈ 790 to 950 cm^{-1}) the propagation of infrared light is forbidden. The sharp resonance in the near-field spectrum is at 930 cm^{-1} exceeding the value of Au by nearly two orders of magnitude [134].

Figure 5.8 presents the near-field contrast image between tip and sample recorded at different illumination frequencies. The contrast is much stronger at the phonon resonance frequency predicted in figure 5.7 (a). The image recorded at 929 and at 978 cm^{-1} proves the
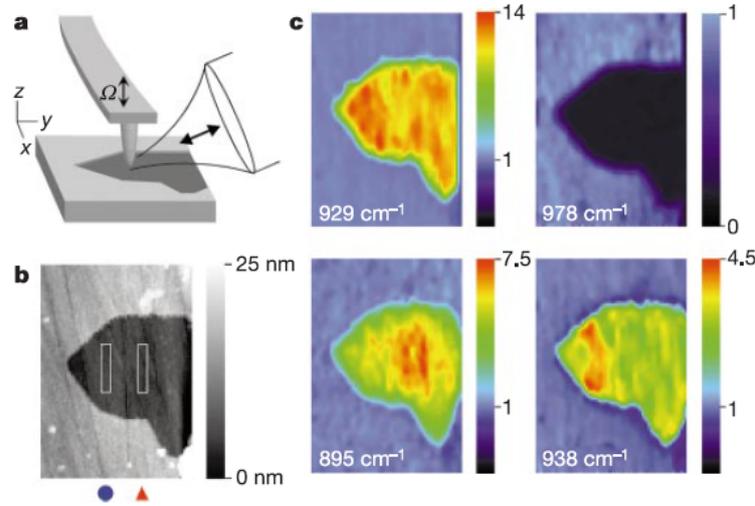
Fig. 5.8: (a) experimental scheme of s-SNOM. The local interaction is possible through an illuminated Pt coated metal tip. (b) presents the topography image of a SiC sample partly covered with Au. (c) displays the scattering amplitude recorded at different frequencies. At phonon resonance, the SiC area appears much brighter than the surrounding Au film (at 929 cm^{-1}). Local variations of the near-field amplitude are observed at either side of the resonance. [134].

very strong phonon effect in SiC [134]. Such material-specific nanoscopic contrast opens new possibilities in the detection and structural assignment of different nanostructured materials [141].

5.3   Basic photoluminescent properties and surface structure of silicon carbide quantum dots

In this section I will present fluorescence and infrared characterization of SiC quantum dots showing clear evidence for quantum confinement and revealing very useful surface properties. Fluorescence properties of SiC quantum dots were studied in water (H$_2$O), ethanol (EtOH), and n-butanol (ButOH) (figures 5.9). All the fluorescence results show a monotonic red shift (figure 5.9 (a) for aqueous solution) with increasing excitation wavelength. The highest band intensity appears at excitation wavelengths of 350-380 nm with a corresponding emission band position in the range of 405-435 nm. Figure 5.9 (b) presents the solvent polarity effect on the emission properties of SiC quantum dots, which results in a red shift of the fluorescence with increasing solvent polarity.
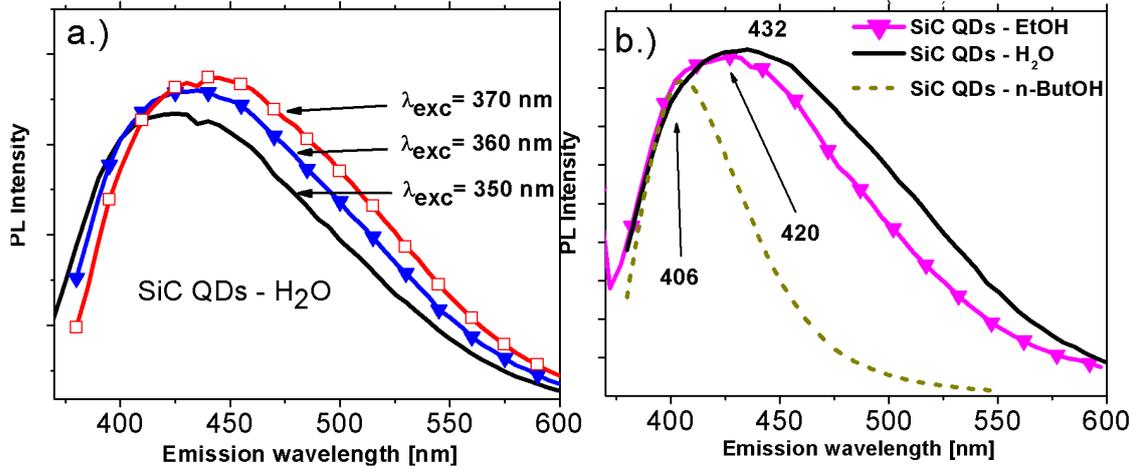
Fig. 5.9: (a) Red shift of the fluorescence of SiC quantum dots in aqueous solution for different excitation wavelengths. (b) PL results of the colloidal SiC quantum dots in different solvents (excitation wavelength 360 nm).

Figure 5.10 shows the infrared spectra of SiC microstructures and quantum dots in the reststrahlen band region. As already described for bulk SiC, in the spectral region between approx. 750 and 1000 cm^{-1} (corresponding to the spectral region between $\tilde{\nu}_{TO}$ and $\tilde{\nu}_{LO}$) the propagation of infrared light is not allowed (reflectivity almost 100 %). The situation is different when the surface of SiC is getting rough or porous (curve (3) in figure 5.6 [131]) where strong changes in the high frequency part of the reststrahlen band are observed. Similar differences compared to the bulk spectrum of SiC (curve (1) in figure 5.6 [131]) can be seen in figure 5.10 with a more pronounced reduction in the LO part of the reststrahlen band. Such spectral changes are related to the surface modification and size reduction of the starting SiC material.

Because of the large surface-to-volume ratio of the SiC quantum dots, it is important to determine accurately the surface structure as it plays an important role in their physical and chemical properties. Such studies require surface sensitive infrared techniques like attenuated total internal reflection (ATR) infrared spectroscopy. I used ATR spectroscopy to reveal the complex nature of the surface geometry of SiC quantum dots, which provides numerous surface terminations to interact with the surrounding solvent molecules. The measurements were carried out after solvent evaporation from the ATR crystal surface. Clear evidence was found of surface related infrared bands characteristic of Si-O-Si, C-O-C, CH as well as COOH and COO-. The functionalization of these surface terminations with

85
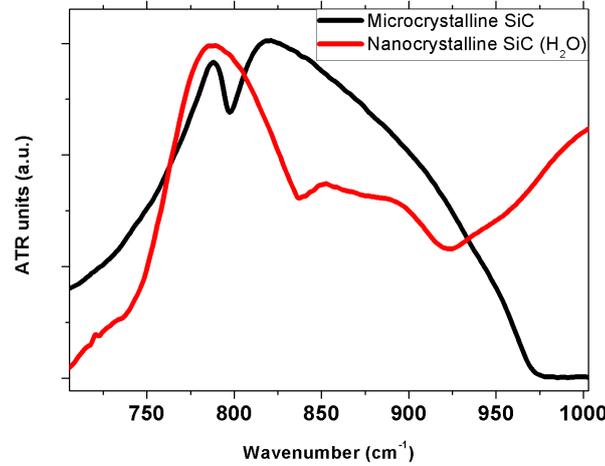
Fig. 5.10: Infrared spectra of SiC micro and nanocrystals in the reststrahlen band region. Comparing to the reststrahlen band of a bulk SiC, clear differences are observed in the LO part of the band. These changes are related to the surface structure modification and size reduction of SiC.

chemical methods is important for further applications. Another important observation is the total absence of Si-H related bands which can be explained by the presence of the more stable surface Si-O-Si groups.

Figure 5.11(a) presents the infrared spectra of the dried SiC microcrystals in comparison with the dried SiC quantum dots from H_2O, EtOH, and ButOH. Each spectrum was baseline corrected and normalized to the Si-C band (at 800 cm^{-1}) of the SiC microcrystals. The spectrum of the SiC microcrystals contains only the Si-C band at 800 cm^{-1}. In contrast, the SiC quantum dots show a multitude of other bands which indicate the surface sensibility of these quantum dots to the surrounding solvents. In order to distinguish between surface-related infrared bands, figure 5.11(b) presents the infrared spectra of the dried SiC quantum dots from EtOH, H_2O, and ButOH in comparison with corresponding pure solvents. Each spectrum was baseline corrected and normalized to enhance the visualization of the results.

Evidently, in some regions, pure solvent infrared bands are still present in the SiC quantum dots spectra (e.g., for the aqueous colloid, the OH bands at 1600 cm^{-1} and at 3350 cm^{-1}), which means that in the present situation, it was not possible to evaporate all the solvents; however, clear evidence of the SiC quantum dots surface related bands is present in these spectra. The Si-C band at 800 cm^{-1} is present for each sample. A clear band at
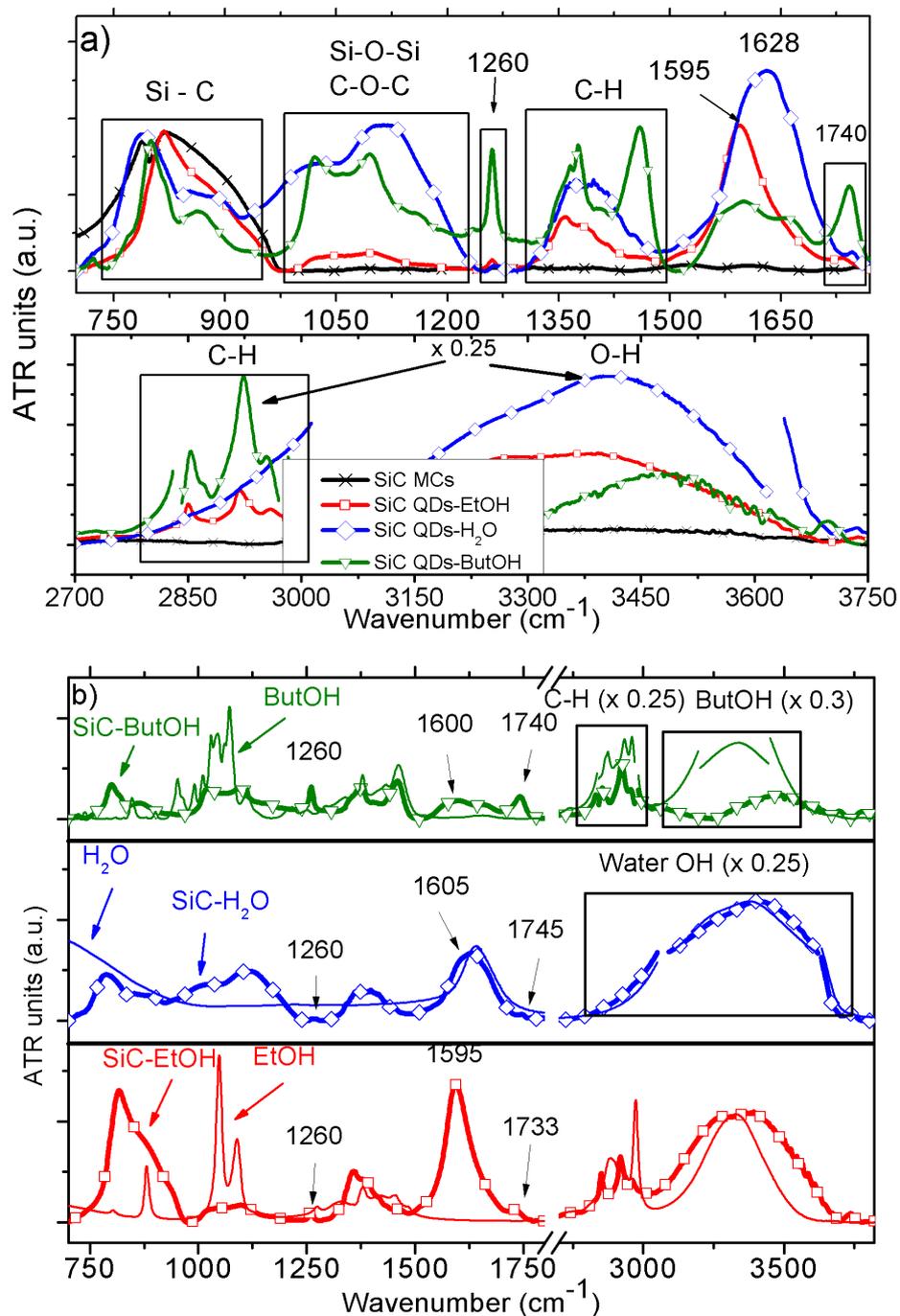
Fig. 5.11: (a) ATR spectra of the dried SiC microcrystals (black curve with cross) compared to the SiC quantum dots spectra in EtOH (red curve with square), H_2O (blue curve with diamond), and ButOH (green curve with triangle). The spectra were recorded on a multi bounce germanium ATR crystal after solvent evaporation. (b) ATR spectra of the dried SiC quantum dots in ButOH (green curve with triangle), H_2O (blue curve with diamond), and EtOH (red curve with square) in comparison with pure ButOH (green curve), H_2O (blue curve), and EtOH (red curve).

1595 cm^{-1} is seen for the EtOH and ButOH colloids which can be assigned to the surface -OH bending vibrations and C=O stretching vibrations, respectively. For the aqueous colloid, this band is also present, but highly overlapped with the OH bending vibration of the non-evaporated water. In the region between 1000 and 1200 cm^{-1}, the C-O stretching of the pure EtOH and ButOH is overlapped with the expected Si-O-Si and C-O-C surface vibrations, but their presence is also evident in each sample if we consider that in the case of the aqueous colloid there are no such overlapping bands between the colloid and the pure solvent. Further surface related bands are present at 1260, 1350-1400, and 1750 cm^{-1} for each colloid. These results are in good agreement with theoretical calculations[117, 118] where the bands at 1260 and at 1750 cm^{-1} represent the symmetric and asymmetric COO-stretching vibrations. The bands at 1350 cm^{-1} correspond to CH bending vibrations and are highly overlapped with the CH bands of EtOH and ButOH. The presence of these bands in the case of the aqueous colloid suggests the existence of surface related CH groups. The origin of the CH stretching bands at 2750-3000 cm^{-1} seems to be related to the quantum dot surface, as their displacements and relative peak height ratios differ from the corresponding CH vibrations of the pure solvents. In the case of the aqueous colloid, the CH stretching region overlaps with the very broad OH signal of the solvent. Even if we expected to observe Si-OH or C-OH groups attached to the surface of the SiC quantum dots, the detection of the OH stretching vibration bands is not trivial. The very strong OH stretching bands above 3000 cm^{-1} of water and ethanol entirely mask the weak OH signals arising from the SiC quantum dots surface. Si-H vibrations could not be detected; so they are not representative of our fabricated SiC quantum dots. Theory suggested that Si-O-Si bonds are more stable than Si-H bonds on SiC quantum dots, which is in line with our finding [117, 118]. Such a surface geometry and especially the presence of the COOH and COO- molecular groups open the possibility for functionalization necessary in various applications.

5.4 Chemical transformation of carboxylic groups on the surface of silicon carbide quantum dots

After presenting the basic PL and infrared properties of SiC quantum dots, in this section I describe the temperature dependence of surface molecular terminations (especially of carboxylic groups). SiC quantum dots were obtained from two different sources (one synthesized in our laboratory by Dávid Beke and one commercial). The surface structure is highly sensitive to the starting SiC powder properties like grain size and porosity (based on previously published results the source SiC grain size is in the range of 10-20 μm and possesses properties which are close to the bulk SiC properties [4]). There are important differences in the infrared spectra of the studied samples: there is a more dominant carboxylic C=O vibrational band in the sample prepared from SiC powder synthesized in our laboratory (sample **1**) than in the sample prepared from commercial SiC powder (sample **2**). A temperature dependent investigation on the dried SiC quantum dots from room tem-
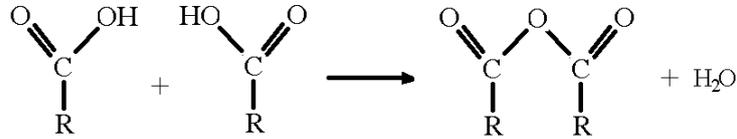
Fig. 5.12: Formation of acid anhydride by two condensed carboxylic acid molecules. R represents either the Si or the C side of SiC quantum dot.

perature up to 450 K was performed to follow the effect of dehydration and to get extra information on the surface and the carboxyl group transformations. These processes were followed by infrared and photoluminescence spectroscopy and yielded clear evidence of acid anhydride formation from carboxyl groups above 370 K. Figure 5.12 presents the equation of synthesis of carboxylic acid anhydrides.

Ab initio modeling (performed by Bálint Somogyi and Adam Gali) supports the correlation between infrared and PL properties as a function of surface termination. Calculations were done on a small-sized, spherical SiC quantum dot containing 79 Si and 68 C atoms with diameter of 1.4 nm (figure 5.13) [6].
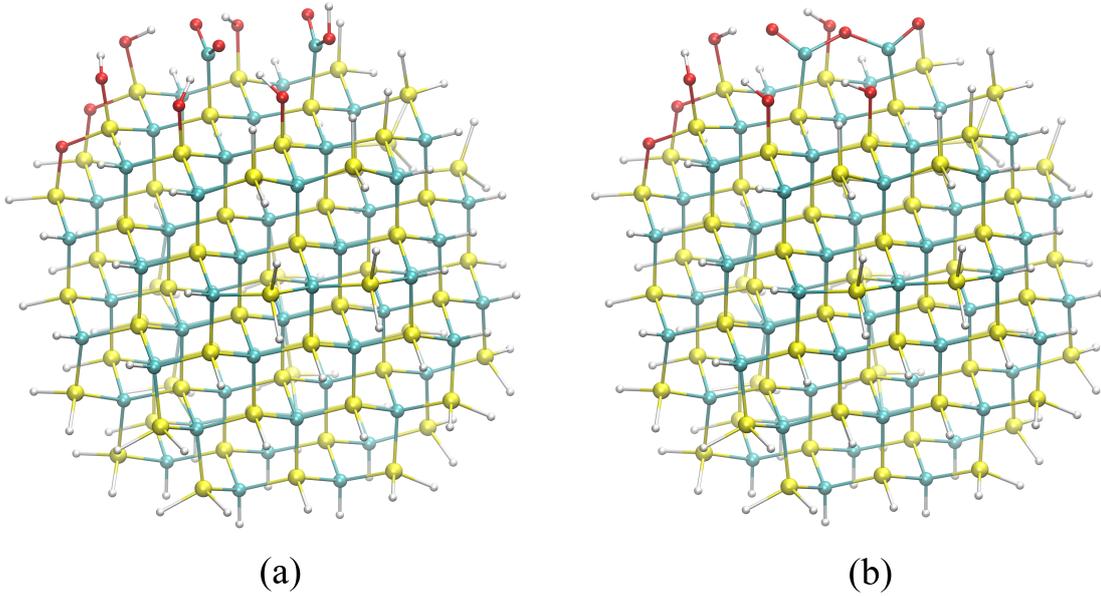
Fig. 5.13: Ball and stick geometries of the two considered surface groups. (a) Si-COOH group near a Si-COO⁻ group, (b) an anhydride group bonding to two Si atoms. For a realistic description of the surface, the Si-H bonds close to the defects were replaced by Si-OH groups and Si-O-Si bridges. White, cyan, yellow and red balls depict H, C, Si and O atoms, respectively (work done by Bálint Somogyi).

Temperature dependence

Figure 5.14 presents the infrared spectra measured at room temperature for sample **1** and sample **2**. The band at approx. 800 cm^{-1} is assigned to SiC. The featureless broad band centered at 1100 cm^{-1} is assigned to C-O-C and Si-O-Si vibrations. The most important region is located at 1720 cm^{-1} and is the C=O vibration of the COOH group. This is also the molecular group which represents the main interest for further functionalization. Taking into account the relative intensity ratio between the oxide band and the carbonyl band we estimate a higher carboxyl concentration for sample **1** (intensity ratio of 1 : 3) in comparison with sample **2** (intensity ratio of 8 : 1). Above 3000 cm^{-1} the spectra are dominated by a broad -OH band assigned to the hydrogen bonded -OH and the hydrate shell around the quantum dots.

Figure 5.15 (a) and (b) present the temperature dependent infrared spectra of sample **1** and **2**, respectively. Interesting behavior occurs at elevated temperatures. Two new bands appear at 1792 and 1860 cm^{-1} as the C=O band is decreasing in intensity. This doublet band is characteristic of the acid anhydride C=O vibrations [142]. Additional information comes from the temperature dependence of the hydration shell related -OH band.
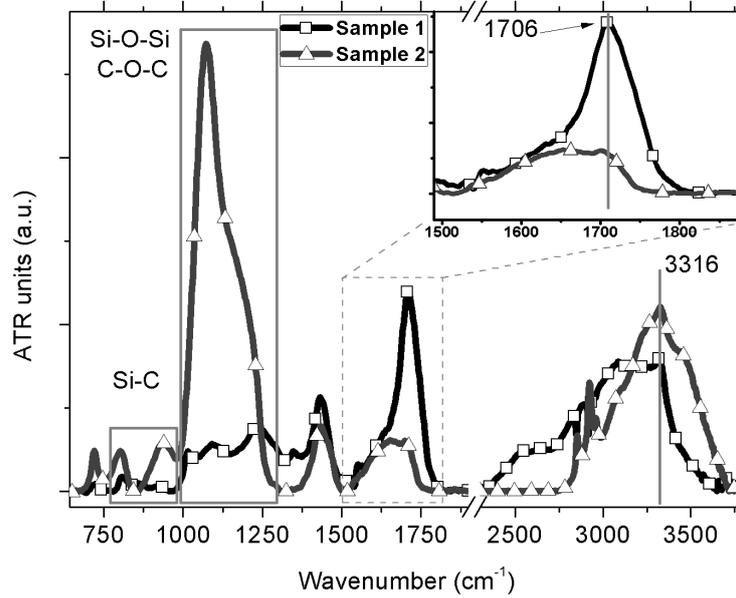
Fig. 5.14: Infrared spectra of sample **1** (black line with empty squares) and sample **2** (grey line with empty triangles). There is a clear difference in the C=O bands of the carboxyl group at 1720 cm^{-1} as well as in the region between 1000-1300 cm^{-1}.

According to figure 5.15 (a) and (b) anhydride formation is observed from 370 K whereas no drastic changes occur above 3000 cm^{-1} (water related -OH band). Above 400 K the carboxyl-carboxyl pair to anhydride transformation saturates as the intensity of the anhydride related bands becomes constant. The very broad -OH band between 3000 - 3600 cm^{-1} also shows a very strong temperature dependence. Above 400 K the decrease in intensity and narrowing of this broad band is getting more evident and is assigned to the complete dehydration of the SiC quantum dots. Similar transformations are observed also for sample **2** where the carboxyl concentration was supposed to be much lower. This behavior suggests that carboxyl sites should be in close proximity both in the high and low concentration situations or rather cases. Two possibilities are considered for the process of carboxyl to anhydride transformation:

(i) anhydride formation between two different SiC quantum dots leading to an inter-dot anhydride. This situation would be possible if the inter-dot carboxyl-carboxyl coupling through hydrogen bonds would be dominant during the drying process. The bound water evaporation and anhydride formation should occur simultaneously. According to figure
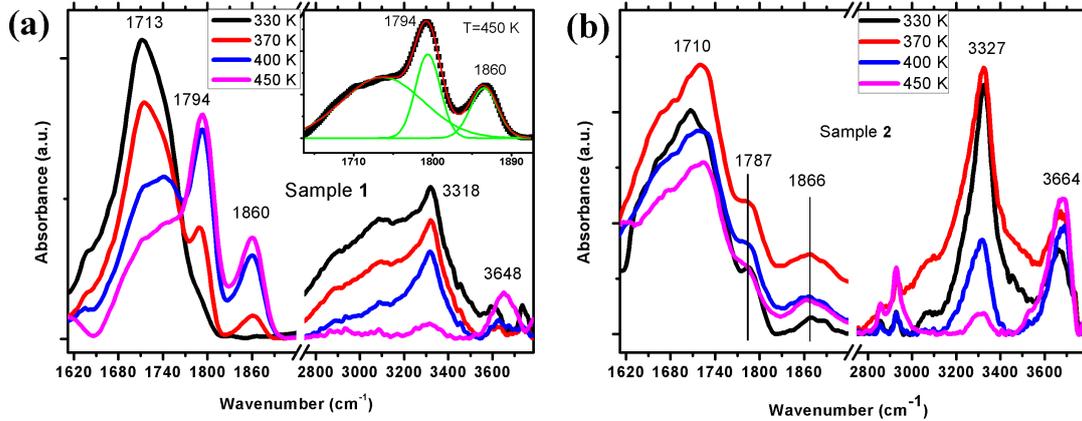
Fig. 5.15: Temperature dependent infrared spectra of sample **1** (a) and sample **2** (b). Above 370 K there is a strong decrease in intensity of the carboxylic C=O band (1720 cm^{-1}) and a doublet band characteristic of the anhydride group appears at 1792 and at 1860 cm^{-1}. The strong decrease in intensity of the O-H band above 3000 cm^{-1} is assigned to the evaporation of the hydrate shell. Inset in (a): Gaussian fit to the infrared spectrum taken at 450 K in the C=O vibration region. Single Gaussian bands situated at 1794 cm^{-1} and at 1860 cm^{-1} indicate the formation of anhydride groups on the Si side of SiC quantum dots.

5.15 I conclude that this situation may not be probable as the saturation of the anhydride formation process can be observed well before the bound water evaporation.

(ii) on-dot anhydride formation by water elimination between two neighboring carboxyl groups. If the synthesis process can favor carboxyl group formation (*e.g.*, during the porous carbide formation where local charges play an important role, or during sonication when the weakly interconnected nanocrystallites are broken [143]) then the neighboring carboxyl sites can form anhydride groups. On-dot anhydride formation requires the presence of carboxyl groups in close proximity to each other and would require that at least one of the two carboxyl sites is not hydrogen bonded [144]. The presumably short lifetime of a hydrogen bonded COOH above 370 K would ensure that unbounded carboxylic groups are available [6].

The nature of the interaction between on-dot surface sites merits a detailed investigation. The OH and COOH groups on the SiC quantum dot surfaces interact with the water molecules of the solvent by hydrogen bonding [145]. The existence of hydrogen bonding between neighboring COOH groups is excluded due to steric effects and proved by the

absence of anhydride formation at room temperature in vacuum (as the situation in figure 5.14). At 450 K a distinct band emerges above 3600 cm^{-1} which is characteristic of the free -OH group. As the anhydride formation is complete at this temperature, the presence of COOH-related OH groups is less probable. We assign this band to Si-OH and C-OH hydroxyl groups which are present also at room temperature at the surface together with COOH groups. As shown in figure 5.15 (a) and (b), after anhydride formation the -OH groups still form hydrogen bonds with water molecules (broad band above 3000 cm^{-1}). This means that the hydrogen bonds between the water molecules and hydroxyl termination sites are stronger than the hydrogen bonds with carboxyl groups, even though in organic molecules carboxylic acids form much stronger hydrogen bonds than alcohols.
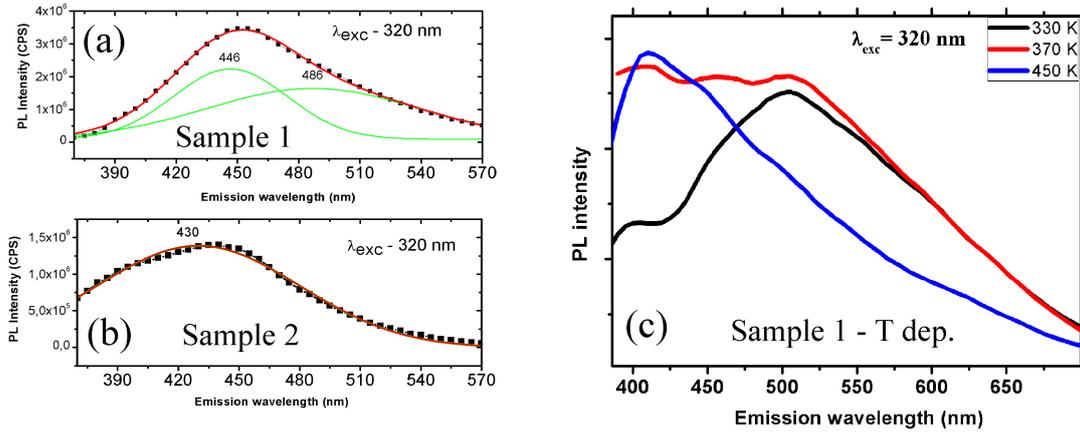
Fig. 5.16: Photoluminescence spectra of (a) sample **1** and (b) sample **2** recorded in water at the maximum emission line with 320 nm excitation wavelength. (c) presents the temperature dependent photoluminescence spectra of sample **1** recorded in solid form of SiC quantum dots on silicon wafer recorded after water evaporation at 330 K. The main emission band is located around 500 nm, at 370 K a clear transition is observed to lower wavelengths, indicating important changes on the surface of SiC quantum dots, and at 450 K the emission maximum is close to 400 nm. In this temperature region bound water has evaporated and anhydride functional groups are formed.

The effect of anhydride formation on the PL properties of SiC quantum dots were also studied. Figure 5.16 (a) and (b) show the PL spectra of sample **1** and sample **2** recorded at 320 nm excitation. The origin of the emission bands is assigned to a complex contribution of the SiC quantum dot LUMO-HOMO transition as well as of the surface states. The emission maximum is at 450 nm for sample **1** and at 430 nm for **2**. Sample **1** shows an

extra emission band at 486 nm which, based on theoretical predictions [117, 118], can be related to the higher carboxyl concentration.

Figure 5.16 (c) presents the PL of sample **1** at three different temperatures (330 K, 370 K, and 450 K). These measurements were carried out after water evaporation from the colloidal suspension of SiC quantum dots on a clean Si wafer. Compared to figure 5.16 (a) the dominant component at 330 K is the emission band situated at 500 nm. Reaching the temperature region where the carboxyl to anhydride reaction and the hydration shell evaporation starts, two bands situated at 410 and 460 nm are increasing in intensity. At even higher temperature (450 K) it is supposed that the total evaporation of the hydrate shell occurs and the maximum of the emission band shifts to ∼400-420 nm. On the other hand, the solvent (water in this case) has a much more important effect on the SiC quantum dot emission through the surface-solvent interactions. Rossi et al. studied the luminescence of SiC quantum dots in hydrofluoric acid solution to eliminate the possible oxide layer on the surface and they reported that the emission maximum shifts to lower frequencies [146] similar as in our study after water evaporation [figure 5.16 (c)]. Based on the similarities between dry and HF dispersed SiC quantum dots we conclude that the PL properties of colloidal suspensions of SiC quantum dots in water depend mainly on the surface structure of SiC quantum dots and the water-quantum dot interactions.

The correlation between the vibrational and optical excitation properties as a function of surface termination was studied by *ab initio* modeling. First, the vibrational properties of the C=O containing groups were investigated. The vibrational properties of individual carboxyl [117] and carboxylate [118] groups were already reported that are in good agreement with the experimental findings. An anhydride-SiC quantum dot surface bond can form in three different ways (see Fig. 5.17): by second-neighbor C-C (a) or Si-Si (b) atoms forming a six-membered ring, or it can bond to first-neighbor Si-C (c) atoms forming a five-membered ring. The calculated two characteristic vibrational frequencies for configurations a), b) and c) are (1715, 1770), (1702, 1770) and (1737, 1835) cm^{-1}, respectively. While the absolute values of the calculated frequencies are within 5% smaller than the experimental ones, it is expected that the chosen methodology is able to well reproduce the relative positions of the two characteristic vibrational modes. This indicates that the five-membered ring (c) can be definitely excluded as the origin of the observed infrared peaks, as the calculated
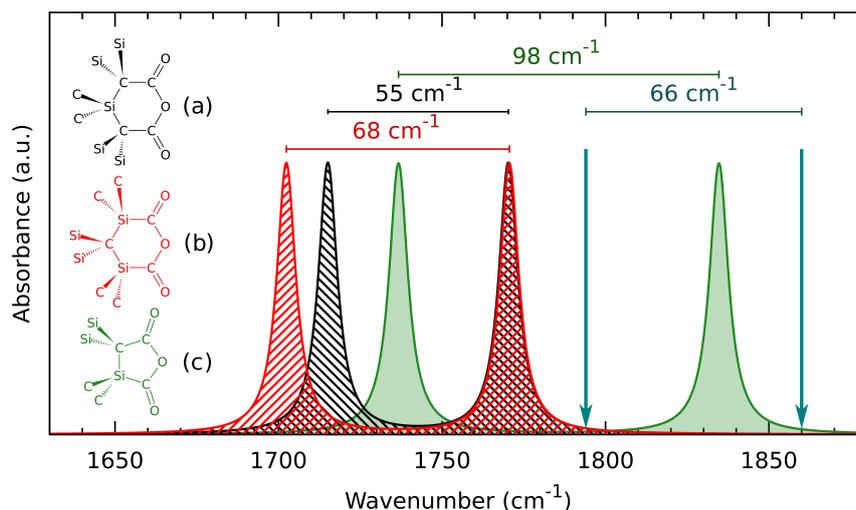
Fig. 5.17: The skeletal formulas and calculated vibrational energies for the three possible anhydride group configurations on the surface of a SiC quantum dot. Black, red and green colors represent anhydride configurations a), b) and c), respectively. We applied an artificial Lorentz broadening of 10 cm^{-1} for the sake of visibility. The blue vertical arrows mark the positions of the experimentally measured absorption peaks in Fig. 5.15 (a). The differences between the characteristic vibrational frequencies of the anhydride group are labeled over the horizontal arrows in all the three cases (work done by Bálint Somogyi).

relative position of $\sim$100 cm^{-1} is significantly larger than the observed 66 cm^{-1}. This is quite plausible as the number of possible sites for these five-membered rings is much smaller than that for the six-membered rings, and the geometry of six-membered rings is much less strained. The calculated relative position of the Si-Si (b) configuration vibrational modes is within 0.5% compared to experiment, while it is within 20% for the C-C configuration (a). According to the experimental analysis [see inset in figure 5.15 (a)] the two characteristic vibrational modes belong to a single anhydride configuration which implies together with the *ab initio* results that the anhydride forms on the Si side of SiC quantum dots. Further details related to the theoretical results can be found in reference [6].

The anhydride formation on the SiC quantum dot surface is an important result as acid anhydride groups are more reactive than the starting carboxylic acid groups. The discovery of anhydride formation on the SiC quantum dot surface allows to make more simple chemistry for subsequent functionalization and opens new possibilities for further surface engineering steps.

5.5 Summary

Well defined spherical colloidal cubic SiC quantum dots with average diameter below 5 nm were studied with infrared and photoluminescence spectroscopy. These quantum dots show strong violet-blue PL emission. Infrared spectroscopy revealed the surface structure of SiC quantum dots which consists of Si-O-Si, C-O-C, CH, COOH, and COO- surface terminations. After revealing the basic photoluminescence and infrared properties of SiC quantum dots, chemical transformation of carboxylic group to acid anhydride group were studied as a function of temperature. The complex surface structure of SiC quantum dots may open an opportunity to use standard chemistry methods for further biological functionalization of such quantum dots.

Thesis points related to the chapter:

[4] I performed room temperature infrared and photoluminescence measurements on silicon carbide quantum dots dispersed in different solvents (water, ethanol, and butanol). Infrared spectroscopy has revealed the complex surface structure of quantum dots involving the presence of COOH and COO- molecular groups which are important for further functionalization processes. [4, 5]

[5] Performing temperature dependent infrared and photoluminescence investigations I found evidence for chemical transformation of carboxylic groups to acid anhydride groups on the surface of silicon carbide quantum dots. Acid anhydride formation was observed above 370 K by water elimination between two neighboring carboxyl groups. Photoluminescence results show that silicon carbide quantum dots emission properties are highly sensitive to the surface structure of quantum dots and to the surface-solvent interactions. [6]

Publications related to the chapter:

4. D. Beke, Zs. Szekrényes, I. Balogh, M. Veres, É. Fazakas, L. K. Varga, K. Kamarás, Zs. Czigány, and A. Gali, Characterization of luminescent silicon carbide nanocrystals

prepared by reactive bonding and subsequent wet chemical etching, *App. Phys. Lett.* 99:213108, 2011.

5. D. Beke, Zs. Szekrényes, I. Balogh, Zs. Czigány, K. Kamarás, A. Gali, Preparation of small silicon carbide quantum dots by wet chemical etching, *J. Mater. Res.*, 28:44, 2013.

6. Zs. Szekrényes, B. Somogyi, D. Beke, Gy. Károlyházy, I. Balogh, K. Kamarás, and A Gali, Chemical transformation of carboxyl groups on the surface of silicon carbide quantum dots, *J. Phys. Chem. C*, 118:19995, 2014.

6. Conclusions and outlook

After studying prototypical molecules able to form hydrogen bonded supramolecular systems and presenting basic spectroscopic properties of silicon carbide quantum dots one major question arises: how 'potential' are the potential applications? Even if many supramolecular approaches were suggested for the preparation of self-assembled systems, to the best of my knowledge, no final devices for real life applications have been created yet. However, the increasing knowledge in controlling the location and accessibility of the molecules in a supramolecular network demonstrates that the "bottom-up" approach is getting closer and closer to industrial applications. Challenging requirements are set up also for quantum dots. For applications in bioimaging and biolabelling techniques a quantum dot must fulfill, at the same time, the following criteria: it should be nontoxic, bioinert, photostable, should be no blinking, be small, be producible in large amounts and show luminescent emission in a range specific to the desired application. Even if no ideal quantum dot was found yet, there are several potential candidates like core-shell quantum dots prepared from group II-VI elements, nanodiamond, carbon dot, and of course silicon carbide. Which of these will be finally used in real world applications? Hopefully the right answer is silicon carbide.

7. Thesis points

1. I prepared an infrared spectral library for the molecular constituents for hydrogen bonded systems. Starting from the basic molecular units and finishing with the final supramolecular assemblies I measured and interpreted the infrared spectra of the supramolecular ordering of different imide-uracil and acetylaminopiridyne based molecular constituents by infrared transmission spectroscopy. [1, 2, 3]

2. I studied the direct evidence of the presence of hydrogen bonds for a pair of monotopic uracil-derivative molecules measuring the spectra of the isolated molecules and that of the aggregated state. For this I applied different methods of infrared spectroscopy: matrix isolation and conventional transmission spectroscopy. I could identify the weakening and subsequent disruption of hydrogen bonds by following the temperature dependence of the affected vibrational bands. The assignment of the processes responsible for the melting of hydrogen bonds was done: a gradual increase of the temperature to intermediate values induces large thermal fluctuations in the dimers that leads to a thermal equilibrium between different dimer configurations. I found that further increase of the temperature above the sublimation point of the molecules the hydrogen bonds are disrupted, indicating that the sublimation temperature provides a good estimate for hydrogen bond stability in such systems. These results are consistent with theoretical results. [2]

3. I studied the supramolecular ordering in the solid state of bis-uracil based linear molecules by different infrared spectroscopic methods. A temperature-induced transition from a highly ordered tetrameric into a linear assembly was observed by temperature dependent infrared measurements. The interaction between molecules in the three perpendicular directions of the solid crystal is governed by three different noncovalent interactions: double hydrogen bonds, van der Waals attraction and π-π stacking. [3]

4. I performed room temperature infrared and photoluminescence measurements on silicon carbide quantum dots dispersed in different solvents (water, ethanol, and butanol). Infrared spectroscopy has revealed the complex surface structure of quantum dots involving the presence of COOH and COO- molecular groups which are important for further functionalization processes. [4, 5]

5. Performing temperature dependent infrared and photoluminescence investigations I found evidence for chemical transformation of carboxylic groups to acid anhydride groups on the surface of silicon carbide quantum dots. Acid anhydride formation was observed above 370 K by water elimination between two neighboring carboxyl groups. Photoluminescence results show that silicon carbide quantum dots emission properties are highly sensitive to the surface structure of quantum dots and to the surface-solvent interactions. [6]

Publications related to the thesis points:

[1] L. Piot, C. A. Palma, A. Llanes-Pallas, Zs. Szekrényes, K. Kamarás, M. Prato,D. Bonifazi and P. Samorì, Selective formation of bi-component arrays through H-bonding of multivalent molecular modules, *Adv. Funct. Mater.*, 19:1207, 2009 (cover page).

[2] Zs. Szekrényes, K. Kamarás, G. Tarczay, A. Llannes-Pallas, T. Marangoni, M. Prato, D. Bonifazi, J. Bjork, F. Hanke, M. Persson, Melting of Hydrogen Bonds in Uracil Derivatives Probed by Infrared Spectroscopy and ab Initio Molecular Dynamics, *J. Phys. Chem. B*, 116:4626, 2012.

[3] Zs. Szekrényes, K. Kamarás, P. Nagy, G. Tarczay, A. Llannas-Pallas, L. Maggini, M. Prato, D. Bonifazi, Direction-dependent secondary bonds and their stepwise melting in a uracil-based molecular crystal studied by infrared spectroscopy and theoretical modeling, *under submission*.

[4] D. Beke, Zs. Szekrényes, I. Balogh, M. Veres, É. Fazakas, L. K. Varga, K. Kamarás, Zs. Czigány, and A. Gali, Characterization of luminescent silicon carbide nanocrystals

prepared by reactive bonding and subsequent wet chemical etching, *App. Phys. Lett.* 99:213108, 2011.

[5] D. Beke, Zs. Szekrényes, I. Balogh, Zs. Czigány, K. Kamarás, A. Gali, Preparation of small silicon carbide quantum dots by wet chemical etching, *J. Mater. Res.*, 28:44, 2013.

[6] Zs. Szekrényes, B. Somogyi, D. Beke, Gy. Károlyházy, I. Balogh, K. Kamarás, and A Gali, Chemical transformation of carboxyl groups on the surface of silicon carbide quantum dots, *J. Phys. Chem. C*, 118:19995, 2014.

Further publications:

[F1] E. Horváth, M. Spina, Zs. Szekrényes, K. Kamarás, R. Gaal, D. Gachet, L. Forró, Nanowires of lead-methylamine iodide ($CH_3NH_3PbI_3$) prepared by low temperature solution-mediated crystallization, *Nano Lett.*, 14:6761, 2014.

[F2] H. M. Tóháti, Á. Pekker, B. Á. Pataki, Zs. Szekrényes, K. Kamarás: Bundle vs. network conductivity of carbon nanotubes separated by type, *Eur. Phys. J. B*, 87:126, 2014.

[F3] B. Botka, M. E. Füstös, H. M. Tóháti, K. Németh, Gy. Klupp, Zs. Szekrényes, D. Kocsis, M. Utczás, E. Székely, T. Váczi, Gy. Tarczay, R. Hackl, T. W. Chamberlain, A. N. Khlobystov, K. Kamarás: Interactions and Chemical Transformations of Coronene Inside and Outside Carbon Nanotubes, *Small*, 10:1369, 2014.

[F4] C. Frigeri, M. Serényi, A. Csik, Zs. Szekrényes, K. Kamarás, L. Nasi, N.Q. Khánh, Evolution of the structure and hydrogen bonding configuration in annealed hydrogenated a-Si/a-Ge multilayers and layers, *App. Surf. Sci.*, 269:12, 2013.

[F5] M. Serényi, C. Frigeri, Zs. Szekrényes, K. Kamarás, L. Nasi, A. Csik, N. Q. Khánh, On the formation of blisters in annealed hydrogenated a-Si layers, *Nanoscale Res. Lett.*, 8:84, 2013.

[F6] D. Beke, Zs. Szekrényes, D. Pálfi, G. Róna, I. Balogh, P. A. Maák, G. Katona, Zs. Czigány, K. Kamarás, B. Rózsa, L. Buday, B. Vértessy and A. Gali, Silicon carbide quantum dots for bioimaging, *J. Mater. Res.*, 28:205, 2013.

Bibliography

[1] L. Piot, C.-A. Palma, A. Llanes-Pallas, M. Prato, Zs. Szekrényes, K. Kamarás, D. Bonifazi, and P. Samorì. Selective Formation of Bi-Component Arrays Through H-Bonding of Multivalent Molecular Modules. *Adv. Funct. Mater.*, 19:1207, 2009.

[2] Zs. Szekrényes, K. Kamarás, G. Tarczay, A. Llannes-Pallas, T. Marangoni, M. Prato, D. Bonifazi, J. Bjork, F. Hanke, and M. Persson. Melting of Hydrogen Bonds in Uracil Derivatives Probed by Infrared Spectroscopy and ab Initio Molecular Dynamics. *J. Phys. Chem. B*, 116:4626, 2012.

[3] Zs. Szekrényes, P. Nagy, G. Tarczay, A. Llannas-Pallas, L. Maggini, M. Prato, D. Bonifazi, and K. Kamarás. Direction-dependent secondary bonds and their stepwise melting in a uracil-based molecular crystal studied by infrared spectroscopy and theoretical modeling. *under submission.*

[4] D. Beke, Zs. Szekrényes, I. Balogh, M. Veres, É. Fazakas, L. K. Varga, K. Kamarás, Zs. Czigány, and A. Gali. Characterization of luminescent silicon carbide nanocrystals prepared by reactive bonding and subsequent wet chemical etching. *Appl. Phys. Lett.*, 99:213108, 2011.

[5] D. Beke, Zs. Szekrényes, I. Balogh, Zs. Czigány, K. Kamarás, and A. Gali. Preparation of small silicon carbide quantum dots by wet chemical etching. *J. Mat. Res.*, 28:44, 2013.

[6] Zs. Szekrényes, B. Somogyi, D. Beke, Gy. Károlyházy, I. Balogh, K. Kamarás, and A Gali. Chemical transformation of carboxyl groups on the surface of silicon carbide quantum dots. *J. Phys. Chem. C*, 118:19995, 2014.

[7] D. Beke, Zs. Szekrényes, D. Pálfi, G. Róna, I. Balogh, P. A. Maák, G. Katona, Zs. Czigány, K. Kamarás, B. Rózsa, L. Buday, B. Vértessy, and A. Gali. Silicon carbide quantum dots for bioimaging. *J. Mat. Res.*, 28:205, 2013.

[8] U. Rossler. *Solid State Theory: An Introduction.* Springer Verlag Berlin Heidelberg, 2009.

[9] R.D. Guenther. *Modern Optics.* John Wiley and Sons, Ltd, 1990.

[10] J.D. Jackson. *Classical electrodynamics.* Wiley: New York, 1998.

[11] M. Born and E. Wolf. *Principles of Optics.* Cambridge University Press, 1999.

[12] M. Dressel and G. Grüner. *Electrodynamics of solids.* Cambridge University Press, 2002.

[13] M. Bass. *Fundamental Optical Properties of Solids (Chapter 9); Handbook of Optics: Fundamentals, techniques, and design,*. McGraw-Hill, 1994.

[14] G. Burns. *Solid State Physics*. Academic Press, 1985.

[15] M. Milosevic. Internal Reflection and ATR Spectroscopy. *Appl. Spectrosc. Rev.*, 39(3):365, 2004.

[16] B.H. Stuart. *Infrared Spectroscopy: Fundamentals and Applications.*

[17] W.T. Silfvast. *Laser Fundamentals*. Cambridge University Press, 2004.

[18] P.R. Griffiths and J.A. de Haseth. *Fourier Transform Infrared Spectrometry, Second Ed.* John Wiley & Sons, Inc., Hoboken, N.J., 2007.

[19] G.C. Pimentel and A.L. McClellan. *The hydrogen bond*. W.H. Freeman and Company, San Francisco, 1960.

[20] G.R. Desiraju. A Bond by Any Other Name. *Angew. Chem., Int. Ed.*, 50(1):52, 2011.

[21] J. Emsley. Very strong hydrogen bonding. *Chem. Soc. Rev.*, 9:91, 1980.

[22] http://old.iupac.org/publications/compendium/.

[23] E. Arunan, G.R. Desiraju, R.A. Klein, J. Sadlej, S. Scheiner, I. Alkorta, D.C. Clary, R.H. Crabtree, J.J. Dannenberg, P. Hobza, H.G. Kjaergaard, A.C. Legon, B. Mennucci, and D.J. Nesbitt. Definition of the Hydrogen Bond (IUPAC Recommendations 2011). *Pure Appl. Chem.*, 83:1637, 2011.

[24] G.A. Jeffrey. *An Introduction to Hydrogen Bonding*. Topics in Physical Chemistry - Oxford University Press. Oxford University Press, 1997.

[25] A. Llanes-Pallas, M. Matena, T. Jung, M. Prato, M. Stöhr, and D. Bonifazi. Trimodular Engineering of Linear Supramolecular Miniatures on Ag(111) Surfaces Controlled by Complementary Triple Hydrogen Bonds. *Angew. Chem., Int. Ed.*, 47:7726, 2008.

[26] A. Llanes-Pallas, C.-A. Palma, L. Piot, A. Belbakra, A. Listorti, M. Prato, P. Samorì, N. Armaroli, and D. Bonifazi. Engineering of Supramolecular H-Bonded Nanopolygons via Self-Assembly of Programmed Molecular Modules. *J. Am. Chem. Soc.*, 131:509, 2009.

[27] A. Llanes-Pallas. *Nanostructuring of organic materials templated by hydrogen bonding*. Unpublished Ph.D. thesis, Universitá Degli Study Di Trieste, 2009.

[28] H. Ibach and H. Lüth. *Solid-State Physics*. Springer-Verlag, 2009.

[29] G. Pohl, A. Perczel, E. Vass, G. Magyarfalvi, and G. Tarczay. Study on Ac-Gly-NHMe and Ac-L-Ala-NHMe, the Simplest Chiral and Achiral Building Blocks of Petides and Proteins. *Phys. Chem. Chem. Phys.*, 9:4698, 2007.

[30] S. Góbi, K. Knapp, E. Vass, Z. Majer, G. Magyarfalvi, M. Hollósi, and G. Tarczay. Is β-homo-proline a pseudo-γ-turn forming element of β-peptides? An IR and VCD spectroscopic study on Ac-β-HPro-NHMe in cryogenic matrices and solutions . *Phys. Chem. Chem. Phys.*, 12:13603, 2010.

[31] A. Witkowski and M. Wójcik. Infrared spectra of hydrogen bond a general theoretical model . *Chem. Phys.*, 1(1):9, 1973.

[32] W.J. Hurley, I.D. Kuntz, and G.E. Leroi. Far-Infrared Studies of Hydrogen Bonding. *J. Am. Chem. Soc.*, 88(14):3199, 1966.

[33] R. Bauer and G. Zundel. Homoconjugated $(NH\cdots N)^-$ Hydrogen Bonds with Great Proton Polarizability - FTIR and NMR Studies. *J. Phys. Chem. A*, 106(24):5828, 2002.

[34] R. Langner and G. Zundel. FT-IR Investigation of $OH\cdots N \rightleftharpoons O^-\cdots H^+N$ Hydrogen Bonds with Large Proton Polarizability in Phosphinic Acid + N-Base Systems in the Middle and Far Infrared Region. *J. Phys. Chem. A*, 102(33):6635, 1998.

[35] C. Norfolk, A. Mukasyan, D. Hayes, P. McGinn, and A. Varma. Processing of meso-carbon microbeads to high-performance materials: Part II. Reaction bonding by in situ silicon carbide and nitride formation . *Carbon*, 44(2):293, 2006.

[36] P. Sangsuwan, J.A. Orejas, J.E. Gatica, S.N. Tewari, and M. Singh. Reaction-Bonded Silicon Carbide by Reactive Infiltration. *Ind. Eng. Chem. Res.*, 40(23):5191, 2001.

[37] D. Axelrod, J.C. Long, and M.W. Davidson in the Interactive Java Tutorial of Total Internal Reflection Fluorescence Microscopy. http://www.olympusmicro.com/primer/java/tirf/evaintensity/.

[38] FT-IR Spectroscopy-Attenuated Total Reflectance (ATR). Perkin Elmer Life and Analytical Sciences. *http://shop.perkinelmer.com/content/TechnicalInfo/TCH_FTI-RATR.pdf*, 2005.

[39] É.B. Vázsonyi, M. Koós, G. Jalsovszky, and I. Pócsik. The role of hydrogen in luminescence of electrochemically oxidized porous Si layer . *J. Lumin.*, 57(1-6):121, 1993. 1-357.

[40] J.R. Lakowicz. *Principles of Fluorescence Spectroscopy.* Springer, 2007.

[41] http://www.horiba.com.

[42] A. Ciesielski, C.-A. Palma, M. Bonini, and P. Samorì. Towards Supramolecular Engineering of Functional Nanomaterials: Pre-Programming Multi-Component 2D Self-Assembly at Solid-Liquid Interfaces. *Adv. Mat.*, 22:3506, 2010.

[43] M. Rossi, V. Blum, P. Kupser, G. von Helden, F. Bierau, K. Pagel, G. Meijer, and M. Scheffler. Secondary Structure of Ac-Alan-LysH+ Polyalanine Peptides (n= 5, 10, 15) in Vacuo: Helical or Not? *J. Phys. Chem. Lett.*, 1:3465, 2010.

[44] A. Tkatchenko, M. Rossi, V. Blum, J. Ireta, and M. Scheffler. Unraveling the Stability of Polypeptide Helices: Critical Role of van der Waals Interactions. *Phys. Rev. Lett.*, 106(11):118102, 2011.

[45] M. O. Blunt, J. C. Russell, M. del Carmen Giminez-Lopez, J. P. Garrhan, X. Lin, M. Schröder, N. R. Champess, and P. H. Beton. Random Tiling and Topological Defects in a Two-Dimensional Molecular Network. *Science*, 322:1077, 2008.

[46] C.-A. Palma, J. Bjork, M. Bonini, M. S. Dyer, A. Llanes-Pallas, D. Bonifazi, M. Persson, and P. Samorì. Tailoring Bicomponent Supramolecular Nanoporous Networks: The Role of Phase Segregation and Polymorphism at the Solid-liquid interface. *J. Am. Chem. Soc.*, 131:13062, 2009.

[47] A. Ciesielski, A. R. Stefankiewicz, F. Hanke, M. Persson, J. M. Lehn, and P. Samorì. Rigid Dimers Formed through Strong Interdigitated H-Bonds Yield Compact 1D Supramolecular Helical Polymers. *Small*, 7(3):342, 2011.

[48] B. A. Blight, C. A. Hunter, D. A. Leigh, H. McNab, and P. I. T. Thomson. An AAAA–DDDD quadruple hydrogen-bond array. *Nat. Chem.*, 3(3):246, 2011.

[49] G. A. Jeffrey and W. Saenger. *Hydrogen Bonding in Biological Structures.* Springer-Verlag, Berlin, New York, Heidelberg, 1991.

[50] J. V. Barth, G. Costantini, and K. Kern. Engineering atomic and molecular nanostructures at surfaces. *Nature*, 437:671, 2005.

[51] M. Surin and P. Samorì. Multicomponent Monolayer Architectures at the Solid-Liquid Interface: Towards Controlled Space-Confined Properties and Reactivity of Functional Building Blocks. *Small*, 3:190, 2007.

[52] D. Philp and J.F. Stoddart. Self-Assembly in Natural and Unnatural Systems. *Angew. Chem., Int. Ed.*, 35(11):1154, 1996.

[53] J.V. Barth, G. Costantini, and K. Kern. Engineering Atomic and Molecular Nanostructures at Surfaces. *Nature*, 437:671, 2005.

[54] J.V. Barth. Molecular Architectonic on Metal Surfaces. *Ann. Rev. Phys. Chem.*, 58(1):375, 2007. PMID: 17430091.

[55] N. Miyashita and D.G. Kurth. Directing supramolecular assemblies on surfaces. *J. Mater. Chem.*, 18:2636, 2008.

[56] X. Ma, Y. Yang, K. Deng, Q. Zeng, K. Zhao, C. Wang, and C. Bai. Molecular miscibility characteristics of self-assembled 2D molecular architectures. *J. Mater. Chem.*, 18:2074, 2008.

[57] A. Embrechts. *Single Molecule Force Spectroscopy of self-complementary hydrogen-bonded supramolecular systems: dimers, polymers and solvent effects.* Unpublished Ph.D. thesis, University of Twente, Enschede, The Netherlands, 2011.

[58] M.J. Brienne, J. Gabard, J.-M. Lehn, and I. Stibor. Macroscopic expression of molecular recognition. Supramolecular liquid crystalline phases induced by association of complementary heterocyclic components. *J. Chem. Soc., Chem. Commun.*, 24:1868, 1989.

[59] M. Kotera, J.-M. Lehn, and J.-P. Vigneron. Self-assembled supramolecular rigid rods. *J. Chem. Soc., Chem. Commun.*, page 197, 1994.

[60] J.A. Theobald, N.S. Oxtoby, M.A. Phillips, N.R. Champness, and P.H. Beton. Controlling molecular deposition and layer structure with supramolecular surface assemblies. *Nature*, 424(-):1029, 2003.

[61] L. Kampschulte, S. Griessl, W.M. Heckl, and M. Lackinger. Mediated Coadsorption at the Liquid - Solid Interface: Stabilization through Hydrogen Bonds. *J. Phys. Chem. B*, 109(29):14074, 2005. PMID: 16852767.

[62] W. Xu, M. Dong, H. Gersen, E. Rauls, S. Vázquez-Campos, M. Crego-Calama, D. Reinhoudt, I. Stensgaard, E. Laegsgaard, T. Linderoth, and F. Besenbacher. Cyanuric Acid and Melamine on Au(111): Structure and Energetics of Hydrogen-Bonded Networks. *Small*, 3(5):854, 2007.

[63] M. Matena, A. Llanes-Pallas, M. Enache, T. Jung, J. Wouters, B. Champagne, M. Stöhr, and D. Bonifazi. Conformation-controlled networking of H-bonded assemblies on surfaces. *Chem. Comm.*, page 3525, 2009.

[64] C-A. Palma, M. Bonini, A. Llanes-Pallas, T. Breiner, M. Prato, D. Bonifazi, and P. Samorì. Pre-programmed bicomponent porous networks at the solid-liquid interface: the low concentration regime. *Chem. Comm.*, 2008:5245, 2008.

[65] T. Marangoni and D. Bonifazi. Nano- and microstructuration of supramolecular materials driven by H-bonded uracil-2,6-diamidopyridine complexes. *Nanoscale*, 5:8837, 2013.

[66] W. S. Yang, S. G. Chen, X. D. Chai, Y. W. Cao, R. Lu, W. P. Chai, Y. S. Jiang, T. J. Li, and J. M. Lehn. Formation of mesophase by hydrogen bond directed self-assembly between barbituric acid and melamine derivatives. *Synth. Met.*, 71:2107, 1995.

[67] B. Ośmiałowski, E. Kolehmainen, R. Dobosz, R. Gawinecki, R. Kauppinen, A. Valkonen, J. Koivukorpi, and K. Rissanen. Self-Organization of 2-Acylaminopyridines in the Solid State and in Solution. *J. Phys. Chem. A*, 114(38):10421, 2010.

[68] F.H. Beijer, R.P. Sijbesma, J.A.J.M. Vekemans, E.W. Meijer, H. Kooijman, and A.L. Spek. Hydrogen-Bonded Complexes of Diaminopyridines and Diaminotriazines:âĂĽ Opposite Effect of Acylation on Complex Stabilities. *J. Org. Chem.*, 61(18):6371, 1996.

[69] A. R. Katritzky and I. Ghiviriga. An NMR study of the tantomerism of 2-acylaminopyridines. *J. Chem. Soc., Perkin Trans. 2*, page 1651, 1995.

[70] D. Bonifazi, S. Mohnani, and A. Llanes-Pallas. Supramolecular Chemistry at Interfaces: Molecular Recognition on Nanopatterned Porous Surfaces. *Chem. A Eur. J.*, 15:7004, 2009.

[71] S. Mohnani, A. Llanes-Pallas, and D. Bonifazi. Mastering nanostructured materials through H-bonding recognitions at interfaces. *Pure Appl. Chem.*, 82:917, 2010.

[72] D. Hadzi and S. Bratos. *Vibrational Spectroscopy of the Hydrogen Bond.* North-Holland, Amsterdam, 1976.

[73] V. Kavitha, K. Sankaran, and K. S. Viswanathan. Conformations of Dimethoxymethylsilane: A Matrix Isolation and Ab Initio Study. *J. Mol. Struct.*, 791:165, 2006.

[74] A. J. Barnes. Matrix isolation vibrational spectroscopy as a tool for studying conformational isomerism. *J. Mol. Struct.*, 113:161, 1984.

[75] I. R. Dunkin. *Matrix-Isolation techniques: a practical approach.* Oxford University Press USA, New York, 1998.

[76] G. S. Parry. The Crystal Structure of Uracil. *Acta Cryst.*, 7:313, 1954.

[77] R. F. Stewart and L. H. Jensen. Redetermination of the crystal structure of uracil. *Acta Cryst.*, 23:1102, 1967.

[78] L. Biemann, T. Hüber, and K. Kleinermanns. Fourier transform infrared spectroscopy of 1-cyclohexyluracil aggregates in $CDCl_3$ solutions. *J. Chem. Phys.*, 130:125102, 2009.

[79] S. Bahn and K. Jacobsen. An Object-Oriented Scripting Interface to a Legacy Electronic Structure Code. *Comp. Sci. & Eng.*, 4:56, 2002.

[80] V. Feyer, O. Plekan, R. Richter, M. Correno, G. Vall-llosera, K. C. Prince, A. B. Trofimov, I. L. Zaytseva, T. E. Moskovskaya, E. V. Gromov, and J. Schirmer. Tautomerism in Cytosine and Uracil: An Experimental and Theoretical Core Level Spectroscopic Study. *J. Phys. Chem. A*, 113:5736, 2009.

[81] M.Y. Choi and R.E. Miller. Infrared Laser Spectroscopy of Uracil and Thymine in Helium Nanodroplets: Vibrational Transition Moment Angle Study. *J. Phys. Chem. A*, 111:2475, 2007.

[82] S.X. Tian, C.F. Zhang, Z.J. Zhang, X.J. Chen, and K.Z. Xu. How many uracil tautomers there are? Density functional studies of stability ordering of tautomers. *Chem. Phys.*, 242:217, 1999.

[83] C. López, R. M. Claramunt, I. Alkorta, and J. Elguero. Solution and solid state (CPMAS) NMR studies of the tautomerism of six-membered heterocyclic compounds related to 2-pyridones. *Spectroscopy*, 14:121, 2000.

[84] A. Les and L. Adamowicz. Oxo-Hydroxy Tautomerism of Uracil and 5-Fluorouracil. *J. Phys. Chem.*, 93:7078, 1989.

[85] J. Leszczynski. Tautomerism of uracil: the final chapter? Fourth-order electron correlation contributions to the relative energies of tautomers. *J. Phys. Chem.*, 96:1649, 1992.

[86] D. A. Estrin, L. Paglieri, and G. Corongiu. A Density Functional Study of Tautomerism of Uracil and Cytosine. *J. Phys. Chem.*, 98:5653, 1994.

[87] Ż. Czyżnikowska, R. Zaleśny, M. Ziółkowski, R.W. Gora, and P. Cysewski. The nature of interactions in uracil dimer: An ab initio study . *Chem. Phys. Lett.*, 450:132, 2007.

[88] M. Pitoňak, K. E. Riley, P. Neogrády, and P. Hobza. Highly accurate CCSD(T) and DFT-SAPT stabilization energies of H-bonded and stacked structures of the uracil dimer. *Chem. Phys. Chem.*, 9:1636, 2008.

[89] V. R. Cooper, T. Thonhauser, and D. C. Langreth. An application of the van der Waals density functional: Hydrogen bonding and stacking interactions between nucleobases. *J. Chem. Phys.*, 128:204102, 2008.

[90] B. Feibush, A. Figueroa, R. Charles, K.D. Onan, P. Feibush, and B.L. Karger. Chiral separation of heterocyclic drugs by HPLC: solute-stationary phase base-pair interactions. *J. Am. Chem. Soc.*, 108(12):3310, 1986.

[91] A.J. Barnes, M.A. Stuckey, W.J. Orville-Thomas, L. Le Gall, and J. Lauransan. Vibrational spectra of barbituric acid derivatives in low-temperature matrices: Part 1. 1-Methyl barbituric acid . *J. Mol. Struct.*, 56(0):1, 1979.

[92] H.I. Abdulla and M.F. El-Bermani. Infrared studies of tautomerism in 2-hydroxypyridine 2-thiopyridine and 2-aminopyridine . *Spectrochim. Acta A*, 57(13):2659, 2001.

[93] B. Morzyk-Ociepa, M.J. Nowak, and D. Michalska. Vibrational Spectra of 1-Methylthymine: Matrix Isolation, Solid State and Theoretical Studies . *Spectrochim. Acta A*, 60(8-9):2113, 2004.

[94] K. Nakamoto, M. Margoshes, and R.E. Rundle. Stretching Frequencies as a Function of Distances in Hydrogen Bonds. *J. Am. Chem. Soc.*, 77(24):6480, 1955.

[95] A.V. Iogansen. Direct proportionality of the hydrogen bonding energy and the intensification of the stretching $\nu(XH)$ vibration in infrared spectra . *Spectrochim. Acta A*, 55(7-8):1585, 1999.

[96] M. Rozenberg, G. Shoham, I. Reva, and R. Fausto. Low temperature Fourier transform infrared spectra and hydrogen bonding in polycrystalline uracil and thymine . *Spectrochim. Acta A*, 60(10):2323, 2004.

[97] H. Morkoc, S. Strite, G.B. Gao, M.E. Lin, B. Sverdlov, and M. Burns. Large-Band-Gap SiC, III-V Nitride, and II-VI ZnSe-Based Semiconductor Device Technologies. *J. Appl. Phys.*, 76:1363, 1994.

[98] P.M. Sarro. Silicon carbide as a new {MEMS} technology . *Sens. Actuators A: Phys.*, 82(1-3):210, 2000.

[99] J.B. Casady and R.W. Johnson. Status of silicon carbide (SiC) as a wide-bandgap semiconductor for high-temperature applications: A review . *Solid-State Electron.*, 39(10):1409, 1996.

[100] V.E. Chelnokov, A.L. Syrkin, and V.A. Dmitriev. Overview of SiC power electronics . *Diamond Rel. Mater.*, 6(10):1480, 1997. Proceeding of the 1st European Conference on Silicon Carbide and Related Materials (ECSCRM 1996).

[101] D.J. Spry, P.G. Neudeck, L.-Y. Chen, G.M. Beheim, R.S. Okojie, C.W. Chang, R.D. Meredith, T.L. Ferrier, and L.J. Evans. Fabrication and Testing of 6H-SiC JFETs for Prolonged 500 °C Operation in Air Ambient . *Mater. Sci. Forum*, 600-603:1079, 2007.

[102] P.G. Neudeck, D.J. Spry, L.-Y. Chen, R.S. Okojie, G.M. Beheim, R. Meredith, and T. Ferrier. SiC Field Effect Transistor Technology Demonstrating Prolonged Stable Operation at 500 °C. *Mater. Sci. Forum*, 556-557:831, 2007.

[103] H.-J. Song and Z.-Z. Zhang. Investigation of the Tribological Properties of Polyfluo Wax/Polyurethane Composite Coating Filled with Nano-SiC or Nano-ZrO$_2$. *Mater. Sci. Eng., A*, 426(1-2):59, 2006.

[104] R Yakimova, R M Petoral Jr, G R Yazdi, C Vahlberg, A Lloyd Spetz, and K Uvdal. Surface Functionalization and Biomedical Applications Based on SiC. *J. Phys. D*, 40(20):6435, 2007.

[105] R. Maboudian, C. Carraro, D.G. Senesky, and C.S. Roper. Advances in Silicon Carbide Science and Technology at the Micro- and Nanoscales. *J. Vac. Sci. Technol. A*, 31(5):050805, 2013.

[106] J. Botsoa, V. Lysenko, A. Geloen, O. Marty, J. M. Bluet, and G. Guillot. Application of 3C-SiC Quantum Dots For Living Cell Imaging. *Appl. Phys. Lett.*, 92(17):173902, 2008.

[107] Y. Fan, H. Li, J. Jiang, L.K.Y. So, Y.W. Lam, and P.K. Chu. 3C˝SiC Nanocrystals as Fluorescent Biological Labels. *Small*, 4:1058, 2008.

[108] J. Pourchez, V. Forest, N. Boumahdi, D. Boudard, M. Tomatis, B. Fubini, N. Herlin-Boime, Y. Leconte, B. Guilhot, M. Cottier, and P. Grosseau. In vitro cellular responses to silicon carbide nanoparticles: impact of physico-chemical features on pro-inflammatory and pro-oxidative effects. *J. Nanopart. Res.*, 14(10):1, 2012.

[109] M. Mwania, Cs. Janáky, K. Rajeshwar, and P. Kroll. Fabrication of β-SiC quantum dots by photo-assisted electrochemical corrosion of bulk powders . *Electrochem. Comm.*, 37(0):1, 2013.

[110] S.E. Saddow (Ed.). *Silicon Carbide Biotechnology, First Ed.* Elsevier, Waltham, MA 02451, USA, 2012.

[111] D. Dai, X. Guo, and J.Y. Fan. Synthesis and photoluminescence of semiconductor quantum dots/cetyltrimethylammonium bromide vesicle core/shell nanostructures . *Appl. Surf. Sci.*, 276(0):359, 2013.

[112] S.A. Alekseev, V.N. Zaitsev, J. Botsoa, and D. Barbier. Fourier Transform Infrared Spectroscopy and Temperature-Programmed Desorption Mass Spectrometry Study of Surface Chemistry of Porous 6H-SiC. *Chem. Mat.*, 19(9):2189, 2007.

[113] J.Y. Fan, H.X. Li, N. Zhang, and R.F. Lu. Identification of the Reconstruction and Bonding Structure of SiC Nanocrystal Surface by Infrared Spectroscopy. *Appl. Surf. Sci.*, 258:627, 2011.

[114] M. Iijima and H. Kamiya. Surface Modification of Silicon Carbide Nanoparticles by Azo Radical Initiators. *J. Phys. Chem. C*, 112(31):11786, 2008.

[115] Y. Li, C. Chen, J.-T. Li, Y. Yang, and Z.-M. Lin. Surface charges and optical characteristic of colloidal cubic SiC nanocrystals. *Nanoscale Res. Lett.*, 6(1):454, 2011.

[116] X. L. Wu, S. J. Xiong, J. Zhu, J. Wang, J. C. Shen, and Paul K. Chu. Identification of Surface Structures on 3C-SiC Nanocrystals with Hydrogen and Hydroxyl Bonding by Photoluminescence. *Nano Lett.*, 9(12):4053, 2009.

[117] T. Frauenheim M. Vörös, P. Deák and A. Gali. The Absorption of Oxygenated Silicon Carbide Nanoparticles. *J. Chem. Phys*, 133:064705, 2010.

[118] T. Frauenheim M. Vörös, P. Deák and A. Gali. Influence of Oxygen on the Absorption of Silicon Carbide Nanoparticles. *Mater. Sci. Forum*, 520:679, 2011.

[119] Y. Zakharko, J. Botsoa, S. Alekseev, V. Lysenko, J.M. Bluet, O. Marty, V.A. Skryshevsky, and G. Guillot. Influence of the Interfacial Chemical Environment on the Luminescence of 3C-SiC Nanoparticles. *J. Appl. Phys.*, 107:013503, 2010.

[120] J.Y. Fan, X.L. Wu, H.X. Li, H.W. Liu, G.G. Siu, and P.K. Chu. Luminescence from colloidal 3C-SiC nanocrystals in different solvents. *Appl. Phys. Lett.*, 88(4):041909, 2006.

[121] M. Fox. *Optical properties of solids, First Ed.* Oxford University Press, Great Clarendon Street, Oxford OX2 6DP, USA, 2001.

[122] R.P. Devaty and W.J. Choyke. Optical Characterization of Silicon Carbide Polytypes. *Phys. Stat. Sol. (a)*, 162(1):5, 1997.

[123] J.Y. Fan, X.L. Wu, and P.K. Chu. Low-dimensional SiC nanostructures: Fabrication, luminescence, and electrical properties . *Prog. Mat. Sci.*, 51(8):983, 2006.

[124] L.T. Canham. Silicon quantum wire array fabrication by electrochemical and chemical dissolution of wafers. *Appl. Phys. Lett.*, 57(10), 1990.

[125] T.K. Sham, D.T. Jiang, I. Coulthard, J.W. Lorimer, X.H. Feng, K.H. Tan, S.P. Frigo, R.A. Rosenberg, D.C. Houghton, and B. Bryskiewicz. Origin of luminescence from porous silicon deduced by synchrotron-light-induced optical luminescence. *Nature*, 363:331, 1993.

[126] H.W. Shim, K.C. Kim, Y.H. Seo, K.S. Nahm, E.-K. Suh, H.J. Lee, and Y.G. Hwang. Anomalous photoluminescence from 3C-SiC grown on Si(111) by rapid thermal chemical vapor deposition. *Appl. Phys. Lett.*, 70(13), 1997.

[127] T. Matsumoto, J. Takahashi, T. Tamaki, T. Futagi, H. Mimura, and Y. Kanemitsu. Blue-green luminescence from porous silicon carbide. *Appl. Phys. Lett.*, 64(2), 1994.

[128] X. L. Wu, J. Y. Fan, T. Qiu, X. Yang, G. G. Siu, and Paul K. Chu. Experimental Evidence for the Quantum Confinement Effect in 3C-SiC Nanocrystallites. *Phys. Rev. Lett.*, 94:026102, Jan 2005.

[129] D.H. Feng, Z.Z. Xu, T.Q. Jia, X.X. Li, and S.Q. Gong. Quantum size effects on exciton states in indirect-gap quantum dots. *Phys. Rev. B*, 68:035334, Jul 2003.

[130] H. Mutschke, A. C. Andersen, D. Clément, T. Henning, and G. Peiter. Infrared properties of SiC particles. *A&A*, 345:187, May 1999.

[131] R. T. Holm, P. H. Klein, and P. E. R. Nordquist. Infrared reflectance evaluation of chemically vapor deposited β-SiC films grown on Si substrates. *J. Appl. Phys.*, 60(4), 1986.

[132] W.G. Spitzer, D.A. Kleinman, and C.J. Frosch. Infrared Properties of Cubic Silicon Carbide Films. *Phys. Rev.*, 113:133, Jan 1959.

[133] H. Kuzmany. *Solid State Spectroscopy, Second Ed.* Springer-Verlag Berlin Heidelberg, 2009.

[134] R. Hillenbrand, T. Taubner, and F. Keilmann. Phonon-enhanced light-matter interaction at the nanometre scale. *Nature*, 418, 2002.

[135] F. Zenhausern, Y. Martin, and H. K. Wickramasinghe. Scanning interferometric apertureless microscopy: optical imaging at 10 Angstrom resolution. *Science*, 269, 1995.

[136] F. Keilmann and R. Hillenbrand. Near-field microscopy by elastic light scattering from a tip. *Phil. Trans. Roy. Soc. A*, 362:787, 2004.

[137] R. Hillenbrand and F. Keilmann. Material-specific mapping of metal/semiconductor/dielectric nanosystems at 10 nmresolution by back-scattering near-field optical microscopy. *Appl. Phys. Lett.*, 80, 2002.

[138] M. Brehm, A. Schliesser, F. Cajko, I. Tsukerman, and F. Keilmann. Antenna-mediated back-scattering efficiency in infrared near-field microscopy. *Opt. Express*, 16:11203, 2008.

[139] A. Zayats and Ed. D.Richards. *Nano-Optics and Near-Field Optical Microscopy.* Artech House, Inc., Norwood, MA 02062, 2009.

[140] N. Ocelic. *Quantitative Near-Field Phonon-Polariton Optical Microscopy.* Unpublished Ph.D. thesis, Technische Universitat Munchen, 2007.

[141] S. Amarie and F. Keilmann. Broadband-infrared assessment of phonon resonance in scattering-type near-field microscopy. *Phys. Rev. B*, 83:045404, Jan 2011.

[142] J. Coates. *Interpretation of Infrared Spectra, A Practical Approach, in Encyclopedia of Analytical Chemistry*. John Wiley and Sons, Ltd, 2006.

[143] G.Z. Cambaz, G.N. Yushin, Y. Gogotsi, and V.G. Lutsenko. Anisotropic Etching of SiC Whiskers. *Nano Lett.*, 6(3):548, 2006.

[144] A. Eisenberg, T. Yokoyama, and E. Sambalido. Dehydration kinetics and glass transition of poly(acrylic acid). *J. Polym. Sci. A-1: Polym. Chem.*, 7(7):1717, 1969.

[145] T.A. Dolenko, S.A. Burikov, J.M. Rosenholm, O.A. Shenderova, and I.I. Vlasov. Diamond-Water Coupling Effects in Raman and Photoluminescence Spectra of Nanodiamond Colloidal Suspensions. *J. Phys. Chem. C*, 116(45):24314, 2012.

[146] A.M. Rossi, T.E. Murphy, and V. Reipa. Ultraviolet photoluminescence from 6H silicon carbide nanoparticles. *Appl. Phys. Lett.*, 92(25):253112, 2008.